Active Length Stabilisation of an Open Fabry-Pérot Microcavity for Colour Centres in Diamond

Master Thesis

Laurens Jan Feije

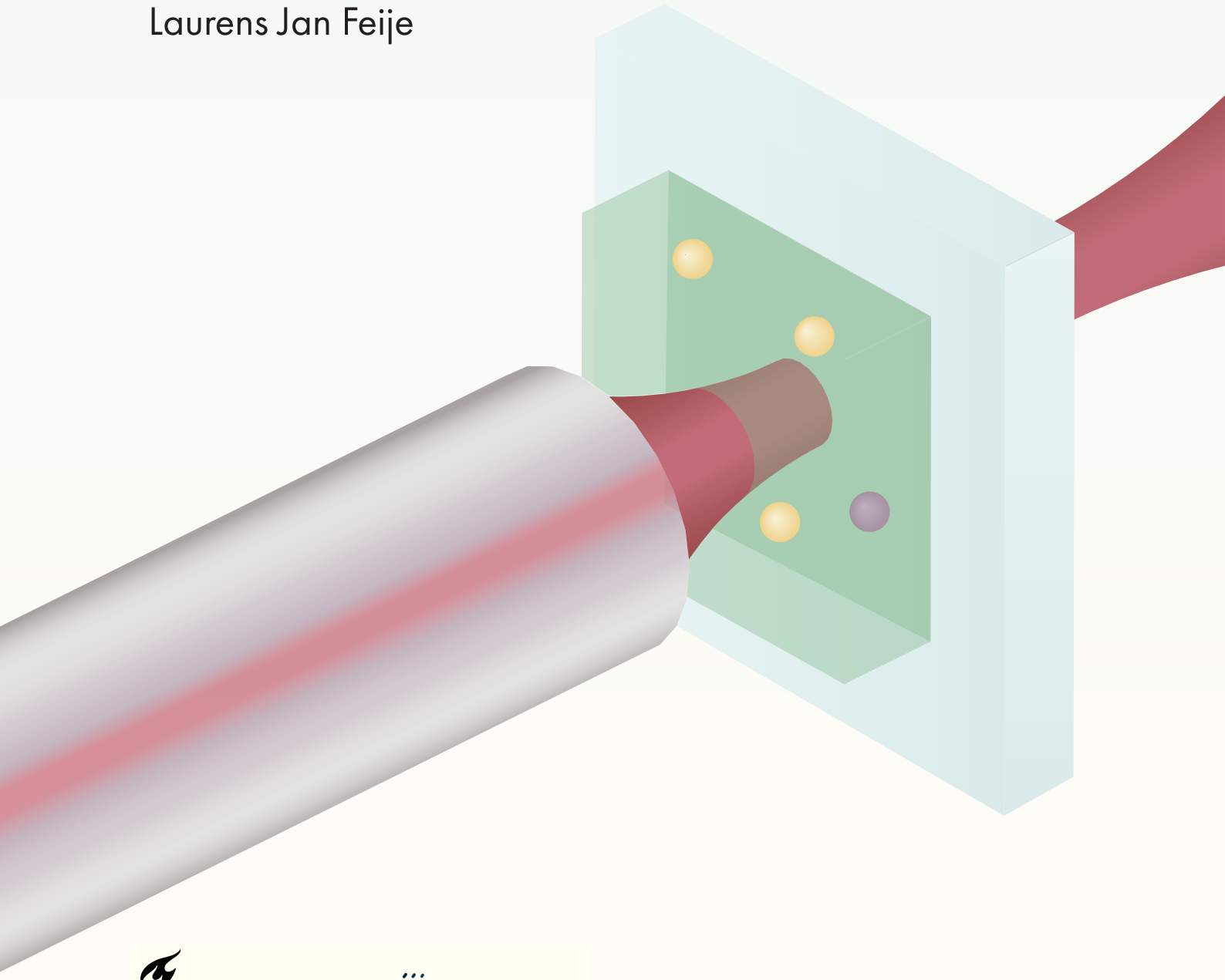

TU Delft QuTech

Active Length Stabilisation of an Open Fabry-Pérot Microcavity for Colour Centres in Diamond

Master Thesis

by

Laurens Jan Feije

To obtain the degree of Master of Science
at Delft University of Technology.
To be defended publicly on Monday October 25, 2021 at 14:00

Daily supervisor:	MSc. Y. S. Herrmann,	QuTech
	PhD. M. J. Weaver,	QuTech
Thesis committee:	Prof. dr. ir. R. Hanson,	QuTech, (Responsible supervisor)
	Dr. ir. T. van der Sar,	Quantum Nanoscience, TUDelft
	PhD. J. Borregaard	QuTech

TU Delft QuTech

Abstract

In order to create a quantum network for distributed quantum computing and secure communication, quantum nodes are required which can share an entangled state. Colour centres in diamond are a very promising set of nodes that can be used to create entanglement between remote locations. A well-studied colour centre in diamond is the Nitrogen Vacancy (NV) centre. The NV centre is a promising candidate because the electron spin can be readout optically and the spin state can be manipulated using microwaves. Furthermore, the NV-centre can be coupled to closely located nuclear spins, where the nuclear spins grant access to multiqubit protocols and the creation of a linked qubit register. A problematic downside of the NV centre is its entanglement rate which is currently limited to $\sim 39Hz$. The entanglement rate can be increased by coupling the colour centre to an optical cavity. One approach is to use open fibre-based Fabry-Pérot microcavities, with the advantage that it can be fibre coupled, achieve high quality factors and its spectral tunability. An important downside to the spectral tunability, is its sensitivity to vibrations. Therefore the goal of this thesis is to characterise a novel fibre-based microcavity setup, investigate the vibrations influencing the microcavity and actively reduce the vibrations with a feedback loop. When a stable optical microcavity is established, a diamond membrane can be placed in the microcavity to enhance its coherent emission.

The novel setup uses a new, low vibration cryostat design together with a passive vibration isolator to suppress vibrations inducing a change in microcavity length. A moveable mirror coated fibre and a flat mirror form the microcavity, where the transmitted light of the microcavity is collected with an objective.

We first show control over the microcavity by measuring the linewidth and the length of the microcavity. With this setup we obtain a typical finesse ~ 6000 (for a bare microcavity), which results in a quality factor of around 80.000 and a mode volume of $27\lambda^3$ for a microcavity length of $5\mu m$. Moreover, we show that the microcavity length dependence on temperature, is roughly $3\frac{1}{3}\mu m$ per $^{\circ}\mathrm{C}$. And we demonstrate a measurement which allows us to measure the angle of the fibre. The angle of can cause a large decrease in the quality factor and is important for mode coupling.

Next, vibrations causing a detuning in microcavity length are characterised. The vibrations can be categorised into multiple frequency ranges which are further analysed. The vibrations for certain frequency ranges can be heavily suppressed by changing the conditions of the passive vibration isolator. By characterising the vibrations, we come to the conclusion that the passive vibration isolation is not optimal, resulting in a high level of vibration. Improving the passive vibration isolation is required in order to proceed to a regime where active feedback can stabilise the microcavity length when the cryostat is on.

Finally, we demonstrate active length stabilisation under vacuum at room temperature. The transmitted light of the microcavity is used to actively feedback a voltage to a coarse piezo and a fine piezo. The coarse piezo counteracts microcavity length drifts at lower frequencies and the fine piezo counteracts faster length fluctuations due to vibrations. With this active feedback method, a fundamental mode of the microcavity can automatically be found, and the microcavity length can be locked to that mode. An estimation of the maximum root mean square (RMS) vibration level with the cryocooler off, at room temperature and with active stabilisation is $10pm$. This is at least a factor 2 lower than the RMS vibration level without active stabilisation.

Multiple suggestions are made to lower the vibration level in the novel setup. For example, how to improve the performance of the passive vibration isolator and how to implement a different active length stabilisation scheme like the Pound-Drever-Hall lock.

Acknowledgement

I cannot begin to try and explain the amount of support I received from a lot of different people. Especially when the COVID-19 pandemic has impacted our daily routines on such big scale. Nonetheless, here is my attempt at expressing my gratitude to all the people who stood beside me during the final part of my master. First and foremost, I want to thank my daily supervisor Yanik. Your dedication, enthusiasm and helpfulness are truly inspiring. Your guidance in the lab, patience in sharing knowledge and aid in my future career choices, truly made my time at QuTech an awesome experience. I am looking forward to continuing the research in the lab for the next two months and hope we manage to get rid of these annoying vibrations.

Matthew and Max I want to thank you both for the interesting (physics) conversations and all of your experience, I learned a lot from both of you. I still remember looking at some peaks appear on a screen and the enthusiasm which came with it, not realising that we just formed the first cavity in the new setup. I wish both of you the best of luck in your future careers in industry.

Ronald, I want to thank you for providing me with the opportunity to graduate in your group. I admire your way of work and how you manage to create such a great environment for everyone to work in. The great atmosphere in team diamond truly makes working more than just performing research in a lab. Furthermore, I want to thank everyone in the team for the last 8 months. Julia, Matteo jr, Matteo sr, Nina, Hans, Kian, Sophie, Arian, Marie-Christine and the new PhD students Mariagrazia and Christopher, I hope to speak all of you during the next two months at lunch and hopefully also in the TPKV.

A special thanks is deserved for Kamiel, who gave me a call and asked if I was still looking for a group to perform my thesis at. I am very grateful for that call and the time we spent together during our thesis at QuTech. Good luck with your final internship at ASML. Annick, Lisa and the new master students of team diamond: Christiaan, Sarel, Otmar and Margriet I really enjoyed my time with all of you. With the number of social activities increasing I hope to organise more dinners and time for drinks after my graduation. Good luck during the upcoming months at QuTech.

I also want to thank Kato for helping out a poor physics student trying to be creative. The cover of my thesis would have been a simple picture in paint if it wasn't for you. Moreover, I want to thank my housemates, friends and fellow graduation students: Dirk, Oyono, Mark and Tijmen for the time I did not spend in the lab. The creative way of finding new stuff to do during the covid lockdown and during the summer really kept me on my feed.

Finally, I want to express my gratitude to my family. Pap, mam, Iris en Pieter I want to thank you for the endless support, not only during my thesis, but during my whole life. I am looking forward to see what the future beholds for all of us.

Laurens Jan Feije
Delft, October 2021

1 Introduction

Networks of quantum systems are very promising as they enable distributed quantum computation [1] and secure communication [2]. For both of these applications, it is essential that the nodes in the network share an entangled state. Colour centres in diamond are a very promising set of nodes that can be used to create entanglement between remote locations. A well-studied colour centre is the negatively charged Nitrogen-Vacancy Centre (NV^-) [3, 4]. The excited state lifetime of the NV^- state is around $12ns$ [5] and the Zero Phonon Line (ZPL) emission is at 637 nm [6]. The NV centre is a promising candidate because the electron spin can be readout optically [7] and the spin state can be manipulated using microwaves [8]. Furthermore, the NV-centre can be coupled to closely located nuclear spins like C^{13} atoms (or N^{14}/N^{15} atoms [9]) which can be used as quantum memories. Moreover, the nuclear spins grant access to multiqubit protocols and the creation of a linked qubit register [10] with long coherence times [11–13]. Since the spin of the NV-centre can be entangled to a photon, the quantum state of the diamond defect can be transmitted with an optical fibre to generate entanglement between two (or multiple [14]) nodes. To create entanglement, two similar NV-centres are required, emitting indistinguishable photons. Therefore the NV-centres need to emit photons in the ZPL in order to generate entanglement. Using the NV-centre as a node has an important downside: the emission of photons into the ZPL is only around 3% of the total emission [15]. The remaining emission is through the frequency broadened Phonon Side Band (PSB) which contains longer wavelengths, up to 800 nm [6]. The low percentage of ZPL photons together with other practical limitations, like the collection efficiency, currently limit the entanglement rate of the NV^- to $39Hz$ [16]. To increase the ZPL photon emission and thus increase the entanglement rate, the NV-centre can be coupled to an open Fabry-Pérot microcavity. If the resonance frequency of the optical microcavity is tuned to be on resonance with the ZPL frequency, the spontaneous emission into the ZPL is increased [17, 18]. This effect is known as the Purcell effect. Apart from the increase of spontaneous emission into the ZPL, the collection efficiency of the photons can also be increased by using a microcavity [19]. The microcavity can be tuned on resonance with the NV^- (or any other colour centre) by changing the length of the microcavity. The spectral tunability of an open Fabry-Pérot microcavity comes with a downside. The microcavity length needs to be extremely stable to stay on resonance with the quantum emitter. Vibrations in the system can induce a detuning in microcavity length and can thus change the resonance condition of the microcavity. Therefore, these vibrations need to be suppressed in order to keep the microcavity on resonance with the ZPL of the NV^- state. An estimate of the maximum size of the detuning of the microcavity is given by: $\Delta L = \frac{\lambda}{2\mathcal{F}}$ [20]. Where ΔL is the microcavity length detuning, λ is the resonance wavelength of the microcavity and $\mathcal{F}$ is the finesse of the microcavity. If the length fluctuations caused by vibrations are covered by ΔL, active feedback can keep the microcavity length on resonance.

In this thesis, a new microcavity setup is characterised. The new setup has a design finesse of $\sim 10.000 - 14.000$ (without diamond) resulting in a maximum tolerance of the RMS vibration level of $\sim 20-30pm$. To obtain this level of vibrations a few goals need to be set which are the focus of this thesis. First, great control of the microcavity is required. Therefore, the properties of the microcavity (length as a function of external factors, linewidth, finesse etc.) need to be determined. Second, the vibrations inducing a detuning in microcavity length need to be characterised. Finally, the vibrations influencing the

microcavity length need to be actively counteracted. To counteract the vibrations inducing a detuning in microcavity length, an active feedback loop needs to be built.

This thesis is constructed in a way that each of these research goals is addressed chronologically. To do so, first, some theory regarding the NV centre and cavities is introduced in Section 2. After the theory, the new microcavity setup is discussed in Section 3. Then, the first goal is addressed in Chapter 4: Characterising the microcavity properties. Followed by the second goal in Chapter 5: Characterising the microcavity length vibrations. In Chapter 6 the final goal: Actively stabilising the microcavity length is discussed in detail. To conclude the research performed during this thesis, the final chapter, Chapter 7, will state a conclusion and an outlook.

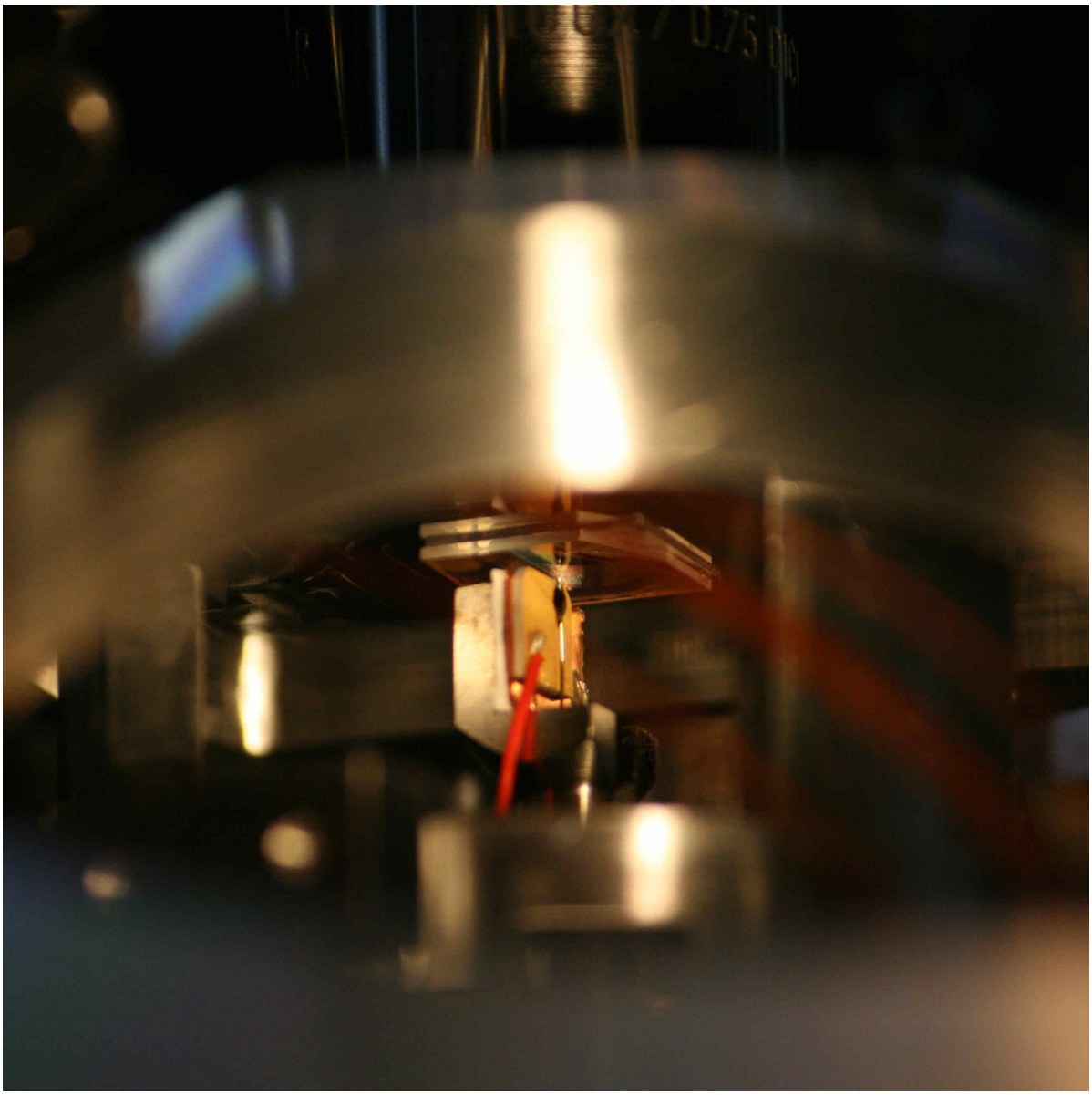

Figure 1.1: Zoom-in of the microcavity used in this thesis. The cavity is formed by a mirror coated fibre and a flat mirror which are both visible in this picture. The light which is transmitted will exit the microcavity at the flat mirror side and is collected with an objective. The fibre can be moved laterally and vertically, thus it can move to different locations on the mirror and change the microcavity length. The fibre is glued to a high bandwidth piezo (yellow square) for active feedback to the microcavity length.

2

Theory

In this chapter the theory necessary to understand the motivation behind this research and the research itself will be introduced. Starting with Section 2.1, where the properties of a Nitrogen-Vacancy centre (NV) in a diamond will be given. Followed by Section 2.2, where the physics of a bare microcavity will be discussed. Finally, in Section 2.3 an explanation will be given why an enhanced entanglement rate is obtained when an NV^- is coupled to a microcavity.

2.1. The Nitrogen-Vacancy Centre in Diamond

Inside diamonds (a crystalline lattice of carbon atoms) defects give rise to different material properties like the colour [21] and the electronic band structure [22]. A Nitrogen-Vacancy centre is one of these defects that can occur in diamonds. The NV defect is created when a carbon atom in the diamond lattice is replaced with a nitrogen atom and a lattice vacancy at its adjacent position. A schematic overview of such an NV centre in diamond is given in Figure 2.1 (left figure). The NV centre has multiple charge states. When there are 5 electrons at the defect, it is called the NV^0 state. However, an extra electron can be captured by the defect creating the NV^- state (6 electrons in total, 3 from carbon, 2 from nitrogen and 1 from a donor). For this thesis, the NV^- state is of most interest and will be discussed in more detail in this section. This section uses the theory described in [23–26].

In Figure 2.1 (right figure) a representation of the available electron orbitals is given. The ground state of the NV^- is formed by two electrons populating level a_1' and two electrons occupying level a_1. The two remaining electrons are unpaired and occupy the $e_{x,y}$ levels. The lowest energy ground state is formed when the two unpaired electrons are combined in a triplet state [23]. The hamiltonian of this ground state in the presence of a magnetic field is given by:

$$\mathcal{H} = DS_z^2 + \gamma_e \vec{B} \cdot \vec{S}. \tag{2.1}$$

With S_i being the Pauli spin operators (1D) and $D = 2.88GHz$ originates from the spin-spin interaction of the unpaired electrons. This interaction causes a split between the $m_s = \pm 1$ and $m_s = 0$ state even without a magnetic field present and is therefore called the zero-field splitting. Due to the Zeeman effect, the degeneracy of the $m_s = \pm 1$ states is lifted by the gyromagnetic ratio of $\gamma_e = 2\pi \cdot 2.802MHz/G$. Since diamond mainly consists out of spinless C^{12} atoms the electron spin state is very well protected resulting in long coherence times [27]. The coherence time of the defect is limited by other impurities and C^{13} isotopes in the diamond lattice. These impurities and isotopes generate an effective spin bath to which the NV centre is susceptible.

A detailed representation of the levels of an NV^- in diamond is given in Figure 2.2. The excited state (^3E in Figure 2.2), related to the previously described ground state ($^3A_2$ in Figure 2.2), of the NV^-, is also a triplet. The energy difference between the excited state and the ground state is $\Delta E = 1.945eV \Leftrightarrow 470.4THz \Leftrightarrow 637nm$. Transitions between these states occur by absorption or emission of photons and are mostly spin conserving. Meaning that the excited $m_s = 0$ state decays to the ground $m_s = 0$ state and the same applies to the $m_s = \pm 1$ states. Only a small fraction of the transitions are not spin conserving due to coupling to the $E_{1,2}$ states, which can decay through singlet states (see Figure 2.2). The ground state can be excited resonantly or off-resonantly. When the ground state is

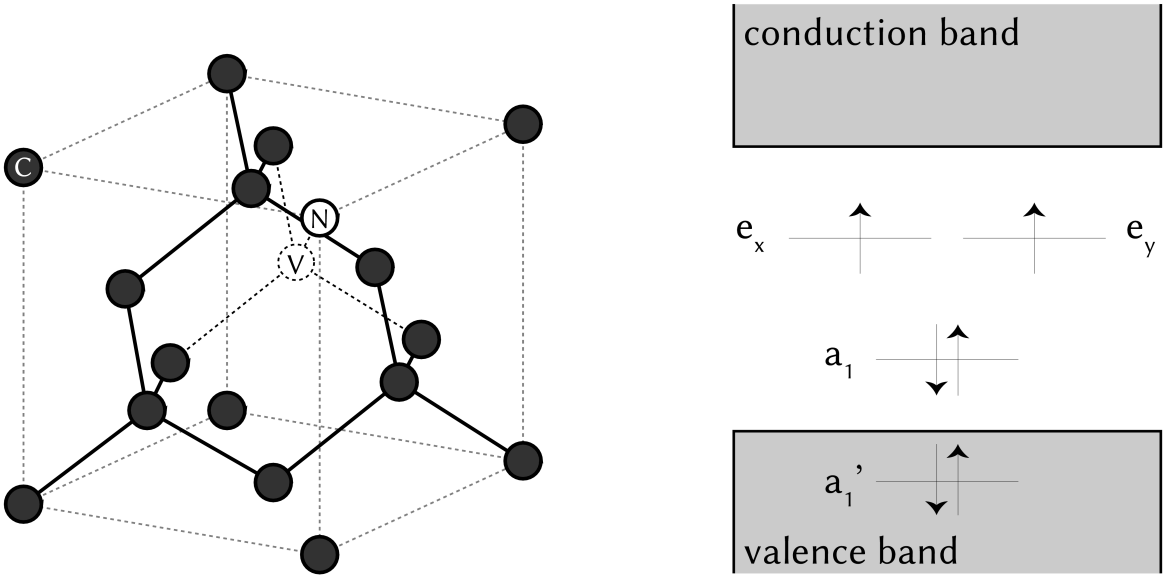

Figure 2.1: **(Left)** Schematic overview of the lattice structure of a NV^- centre in diamond. The defects hosts 6 electrons, 3 from carbon, 2 from nitrogen and 1 from a nearby donor. **(Right)** Available electron orbitals, which are combinations of the nitrogen and carbon atomic orbitals located in the bandgap of diamond. In the ground state, the lowest levels (a_1', a_1) are double occupied while the $e_{x,y}$ levels have an unpaired electron. When an electron moves from the a_1 level to the $e_{x,y}$ levels, the NV^- goes into the excited state. Figure adapted from [26].

excited off-resonantly the NV^- has higher energy than the excited state and will decay to the excited state by creating one (or multiple) phonon(s). The decay from the excited state to the ground state can happen in either two ways:

1. **Directly:** The excited state decays directly back to the ground state by emitting a single photon with $E = 1.945eV \Leftrightarrow \lambda = 637nm$. This process is called emission into the Zero Phonon Line (ZPL)

2. **Indirectly:** The excited state decays by emitting a photon with $E < 1.945eV$ and subsequently creating a phonon to decay back in to the ground state. This process is called emission into the Phonon Side Band (PSB)

Only 3% of the transition between the excited state and the ground state goes through the ZPL [15]. The remaining decay goes through emission into the PSB. The NV^- emission spectrum at cryogenic temperatures (7K) is given in Figure 2.3. The spectrum shows the presence of a sharp frequency emission into the ZPL and a frequency broadened emission into the PSB. There are several advantages for NV manipulations due to the presence of the PSB, like off-resonant excitation (useful for NV initialization and readout) and spectral separation of excitation and detection light. The big disadvantage of emission into the PSB is that the frequency of the photons in the PSB is not well-defined. To create entanglement between two different nodes, indistinguishable photons are required. Meaning that the PSB photons cannot be used for entanglement generation. As the photons in the ZPL are defined in frequency, only these photons can be used for entanglement generation [3]. Due to the small percentage of ZPL photons, the entanglement rate is limited to $39Hz$ [16]. One way to increase the number of photons emitted into the ZPL is to couple the NV^- to a microcavity.

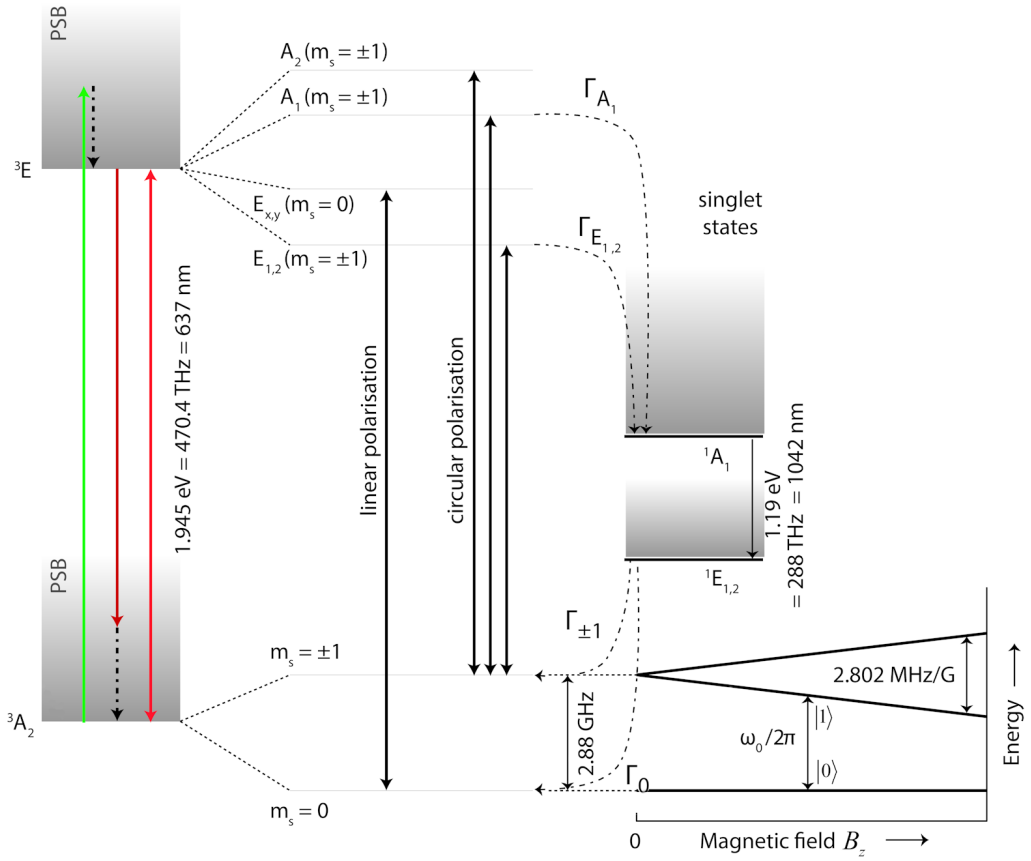

Figure 2.2: The electronic level structure of an NV⁻. The ground state can be excited by resonant excitation (orange arrow) or off-resonant excitation (green arrow). The decay of the excited state can go through, the PSB by creating an extra phonon (dark red arrow) or through the ZPL (orange arrow). Both the excited and ground states are spin-triplets. The degeneracy in the ground state is lifted by the zero field splitting, $D = 2.884GHz$. If a magnetic field is present, the $m_s = \pm1$ states are split due to the Zeeman effect. Transitions are mostly spin conserving, only if the decay goes through the singlet states the spin number can be changed. Figure adapted from [23] and [25].

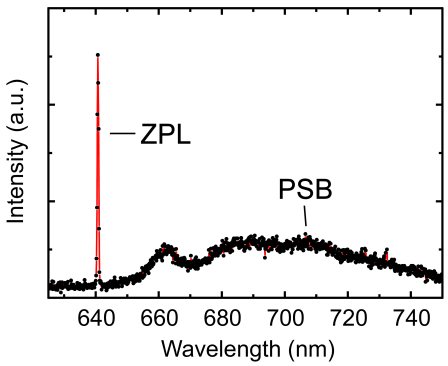

Figure 2.3: The NV⁻ emission spectrum at 7K, measured with a spectrometer. The sharp peak at $\sim 637nm$ shows the well defined (in frequency) ZPL transition of the NV^-. The broadened area at higher frequencies shows the not well defined (in frequency) PSB. Figure adapted from [24].

2.2. Open Fabry-Pérot Microcavities

In this section, a more elaborate description of open Fabry-Pérot microcavities will be discussed. The focus will be on an open Fabry-Pérot microcavity where one side of the microcavity consists out of a concave fibre mirror and the other side consists out of a plane mirror (see Figure 2.6). First, the basic principle of a 1D microcavity will be explained, concerning the transmission and reflection (Section 2.2.1). Next, some properties and working principles of highly reflective distributed Bragg reflectors (DBR) will be discussed, as these reflectors are commonly used in cavities (Section 2.2.2). Finally, the Gaussian beam propagation in the microcavity will be addressed in Section 2.2.3.

2.2.1. 1D-Microcavity Transmission and Reflection

To describe some basic principles of a microcavity, a 1D model will suffice to show the expected transmission and reflection of the optical cavity. The 1D-microcavity consists out of two reflecting surfaces placed at a distance L_{cav} away from each other. Where the material between the mirrors has a refraction index n. In Figure 2.4 a schematic overview of such a 1D-microcavity is displayed. Using the transfer matrix method [28, Chapter 5], a transfer matrix for each component in the microcavity can be composed. Multiplying each matrix in the correct order gives the final effective transfer matrix of the microcavity. Where the order of the transfer matrices is:

1. Reflection/Transmission at mirror 1.
2. Travelling over distance L_{cav} in a medium with refraction index n.
3. Reflection/Transmission at mirror 2.

The transfer matrix of reflection/transmission at a reflecting surface is generally given by:

$$M = \frac{1}{t}\begin{pmatrix} 1 & r \\ r & 1 \end{pmatrix}, \tag{2.2}$$

where t is the transmission coefficient of the mirror and r the reflection coefficient. The transfer matrix of travelling a distance L_{cav} in medium with refraction index n is given by:

$$P = \begin{pmatrix} e^{ikL_{cav}} & 0 \\ 0 & e^{-ikL_{cav}} \end{pmatrix}. \tag{2.3}$$

Here $k = \frac{2\pi n}{\lambda_0}$ is the wave vector in the medium (λ_0 is the wavelength in vacuum). The total transfer matrix for the microcavity thus becomes:

$$\begin{aligned} M_{cav} &= M_2 P_{L_{cav}} M_1 \\ &= \frac{1}{t_2}\begin{pmatrix} 1 & r_2 \\ r_2 & 1 \end{pmatrix}\begin{pmatrix} e^{ikL_{cav}} & 0 \\ 0 & e^{-ikL_{cav}} \end{pmatrix}\frac{1}{t_1}\begin{pmatrix} 1 & -r_1 \\ -r_1 & 1 \end{pmatrix} \\ &= \frac{1}{t_2 t_1}\begin{pmatrix} e^{ikL_{cav}} - r_1 r_2 e^{-ikL_{cav}} & -r_1 e^{ikL_{cav}} + r_2 e^{-ikL_{cav}} \\ r_2 e^{ikL_{cav}} - r_1 e^{-ikL_{cav}} & e^{ikL_{cav}} - r_1 r_2 e^{-ikL_{cav}} \end{pmatrix}. \end{aligned} \tag{2.4}$$

From the transfer matrix the total transmission and reflection coefficients can be determined by using :

$$\begin{pmatrix} E_{in} \\ E_{refl} \end{pmatrix} = \begin{pmatrix} M_{cav[1,1]} & M_{cav[1,2]} \\ M_{cav[2,1]} & M_{cav[2,2]} \end{pmatrix}\begin{pmatrix} E_{trans} \\ 0 \end{pmatrix}. \tag{2.5}$$

Using the definition of the total transmission : $T = \left|\frac{E_{trans}}{E_{in}}\right|^2$ the total transmission of the microcavity will be:

$$\begin{aligned} T &= \left|\frac{1}{M_{cav[1,1]}}\right|^2 = \frac{|t_2|^2|t_1|^2}{\left|e^{ikL_{cav}} - r_2 r_1 e^{-ikL_cav}\right|^2} \\ &= \frac{|t_2|^2|t_1|^2}{(1-r_1r_2)^2\left(1+\left(2\frac{\sqrt{r_1r_2}}{1-r_1r_2}\right)^2 \sin^2(kL_{cav})\right)}. \\ &= \frac{|t_2|^2|t_1|^2}{(1-r_1r_2)^2}\frac{1}{1+\left(\frac{2\mathcal{F}}{\pi}\right)^2 \sin^2(kL_{cav})} \end{aligned} \tag{2.6}$$

In the last step an assumption is made that the microcavity uses highly reflective Bragg mirrors (see Section 2.2.2). Thus the reflection fraction can be approximated with $r_i \approx \sqrt{1-\mathcal{L}_i}$, where $\mathcal{L}_i$ are the losses of mirror i. Resulting in the definition for the finesse:

$$\mathcal{F} = \frac{\pi\sqrt{r_1r_2}}{1-r_1r_2} \approx \frac{2\pi}{\mathcal{L}_1+\mathcal{L}_2}. \tag{2.7}$$

From equation 2.6 it is clear that the transmission is maximal when,

$$kL_{cav} = m\pi \rightarrow L_{cav} = m\frac{\pi}{k} = m\frac{\lambda}{2}. \tag{2.8}$$

In this thesis, the microcavity does not consist out of 2 plane mirrors, but one mirror has a dimple with a certain Radius Of Curvature (ROC). To ensure the stability of the microcavity there is a relation between the length of the microcavity and the ROC of the mirror. Note that a stable microcavity in this sentence means that the microcavity traps the light inside of it, it has nothing to do with the stability of the length of the microcavity. The microcavity traps the light inside of it when the following condition is met [29]:

$$0 < \left(1-\frac{L_{cav}}{ROC_1}\right)\left(1-\frac{L_{cav}}{ROC_2}\right) < 1. \tag{2.9}$$

Here ROC_1 and ROC_2 indicate the radius of curvature of mirror 1 and mirror 2 respectively. The microcavity used in this thesis has one plane mirror ($ROC_1 = \infty$) and a concave mirror with $ROC_2 = ROC$. To obtain a stable microcavity the length of the microcavity should thus satisfy: $0 < L_{cav} < ROC$.

To obtain a low loss microcavity special reflecting surfaces are used to reduce the losses per round trip. A commonly used reflecting surface with low losses is a Distributed Bragg Reflector (DBR) or Bragg mirror.

2.2.2. Bragg Mirrors

A Distributed Bragg Reflector (commonly known as a Bragg/dielectric mirror) does not use a single reflecting layer to act as a mirror. Instead, it uses multiple layers to let the reflected light after each layer constructively interfere. When light encounters a surface with a higher refraction index, the reflected light will obtain a phase shift of $180°$. By systematically alternating a medium with a high reflection index and a low reflection index, the reflected light will constructively interfere if the thickness of the media is chosen carefully. By taking thicknesses $t_{high} = \frac{\lambda}{4n_{high}}$ and $t_{low} = \frac{\lambda}{4n_{low}}$ the light with and without phase shift will constructively interfere upon reflection [30]. By placing multiple layers, more and more light will be reflected and thus a highly reflective surface is created for certain wavelengths, up to 99.9997 % reflectivity [31]. A schematic overview of a Bragg mirror is shown in Figure 2.5. These Bragg mirrors are commonly used for cavities where low losses are desirable. Each layer of the mirror can be deposited separately and on a large variety of different materials. In this thesis an open fibre Fabry-Pérot microcavity is used, where the fibre has a small dimple on the surface. The reason why a plane-concave microcavity has been chosen will be explained in Section 2.2.3

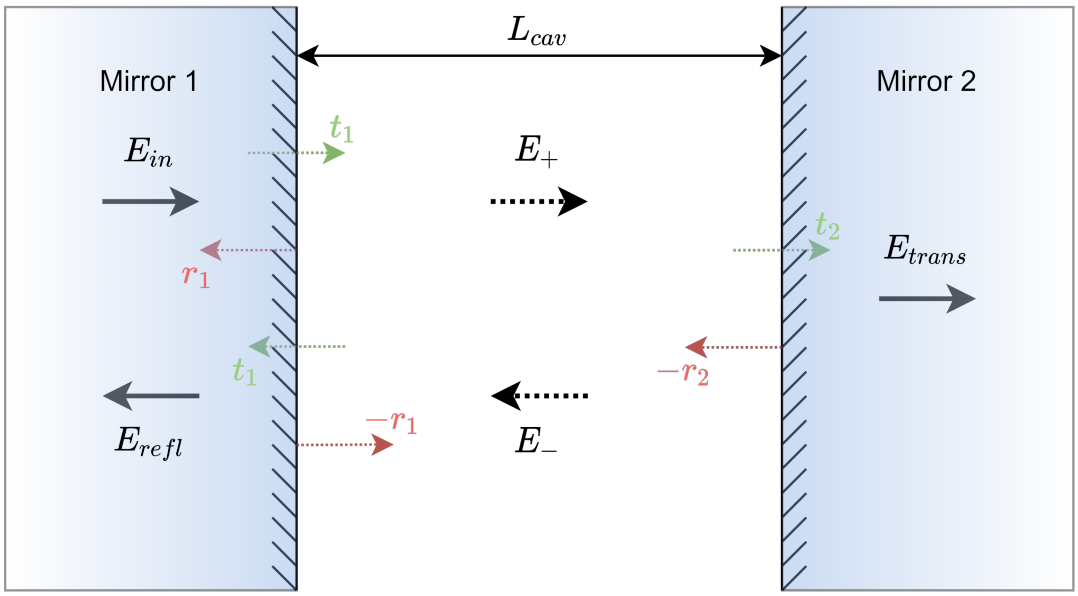

Figure 2.4: Schematic overview of a 1D-microcavity where at every interface a fraction of the incoming electric field (E_{in}) gets transmitted and reflected, causing an effective electric field in the microcavity moving to the right (E_+) and to the left (E_-). After the reflections in the microcavity there is an effective transmitted electric field moving to the right of mirror 2 (E_{trans}) and a reflected electric field moving to the left of mirror 1 (E_{refl}). The transmitted fractions are indicted in green, the reflected fractions are indicated in red and the distance between the mirrors is L_{cav}. The - sign in front of the reflection fractions arises from the propagation direction of the electric field

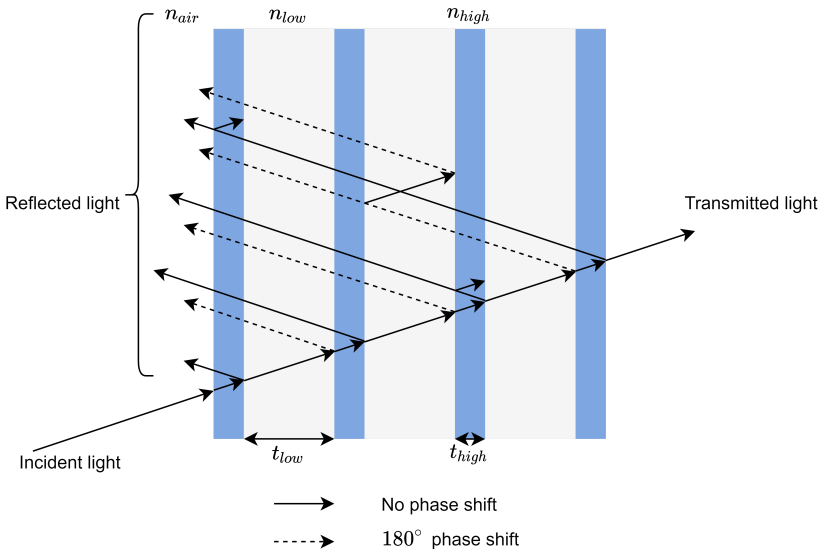

Figure 2.5: Schematic representation of a distributed Bragg reflector. n_{high} and n_{low} represent the refraction indices of the media, whereas t_{high} and t_{low} represent the thickness of the media. When light travels from a medium with a low refraction index to a medium with high reflection index the light will obtain a phase shift of 180°.

2.2.3. Gaussian Mode Propagation in an Open Cavity

The model for the microcavity described in Section 2.2.1 is a simplified model. The real microcavity is a 3D-microcavity and light will not be constricted to a beam with a constant beam waist (plane wave). Starting with the Coulomb Gauge and the Maxwell equations, the electric and magnetic fields of light in free space can be described by [32]:

$$\nabla^2 \vec{A}_c - \frac{1}{c^2}\frac{\partial^2 \vec{A}_c}{\partial t^2} = 0, \tag{2.10}$$

with $c = 2.998 \cdot 10^8 m/s$ the speed of light, $\vec{B} = \nabla \times \vec{A}_c$ and $\vec{E} = -\frac{\partial \vec{A}_c}{\partial t}$. This equation can be solved by starting with a scalar wave function:

$$\nabla^2 U - \frac{1}{c^2}\frac{\partial^2 U}{\partial t^2} = 0. \tag{2.11}$$

Using a trial wavefunction in the form of a monochromatic wave with wave number k and frequency ω travelling in the z direction, the solution

$$U(\vec{r}, t) = \psi(\vec{r}_\perp, z) e^{i(kz-\omega t)} \tag{2.12}$$

is obtained. If the assumption is made that $\psi(\vec{r}_\perp, z)$ changes little in the z direction (paraxial approximation):

$$k\frac{\partial \psi}{\partial z} \gg \frac{\partial^2 \psi}{\partial z^2}, \tag{2.13}$$

the following solution is obtained:

$$U(\vec{r}, t) = \int dq_\perp^2 \tilde{\psi}(\vec{q}_\perp) e^{i\left(\vec{q}_\perp \cdot \vec{r}_\perp + \left\{k - \frac{\vec{q}_\perp^2}{2k}\right\} z - \omega t\right)}. \tag{2.14}$$

Where $q_\perp$ is the 2D wave vector and $\tilde{\psi}(\vec{q}_\perp)$ has to be chosen such that $\psi(\vec{r}_\perp)$ falls to zero rapidly as $|\vec{r}_\perp|$ increases. A fundamental Gaussian weight function would be a suitable candidate for $\tilde{\psi}(\vec{q}_\perp)$ and is defined as:

$$\tilde{\psi}(\vec{q}_\perp) = w_0^2 e^{-\frac{1}{4} w_0^2 \vec{q}_\perp^2}. \tag{2.15}$$

This gives the final solution to equation 2.12

$$\begin{aligned} U(\rho, z, t) &= 4\pi \frac{w_0^2}{w_0^2 + i\frac{2z}{k}} e^{-\frac{\rho^2}{w_0^2 + i\frac{2z}{k}}} e^{-i(kz-\omega t)} \\ &= 4\pi \frac{w_0}{w(z)} e^{-\frac{\rho^2}{w^2(z)}} e^{i\left(\alpha(z) - \frac{k\rho^2}{2R(z)} - kz + \omega t\right)} \end{aligned} \tag{2.16}$$

$$w(z) = w_0 \sqrt{1 + \left(\frac{z}{z_R}\right)^2}, \tag{2.17}$$

$$\alpha(z) = \arctan\left(\frac{z}{z_R}\right), \tag{2.18}$$

$$R(z) = z\left(1 + \left(\frac{z_R}{z}\right)^2\right), \tag{2.19}$$

$$z_R = \frac{1}{2} k w_0^2. \tag{2.20}$$

Here $\rho^2 = x^2 + y^2$ and w_0 is commonly referred to as the beam waist. $w(z)$ is half of the width of the beam, $R(z)$ is the curvature of the wavefront, $\alpha(z)$ the Gouy phase shift (originates from the deviation between the planar wave and Gaussian beam) and z_R is the Rayleigh length (the distance from the beam waist to the position where the curvature of the expanding beam is maximal). This equation describes a Gaussian expanding beam in the propagation direction. A schematic of such a Gaussian beam in a plane-concave microcavity is depicted in Figure 2.6.

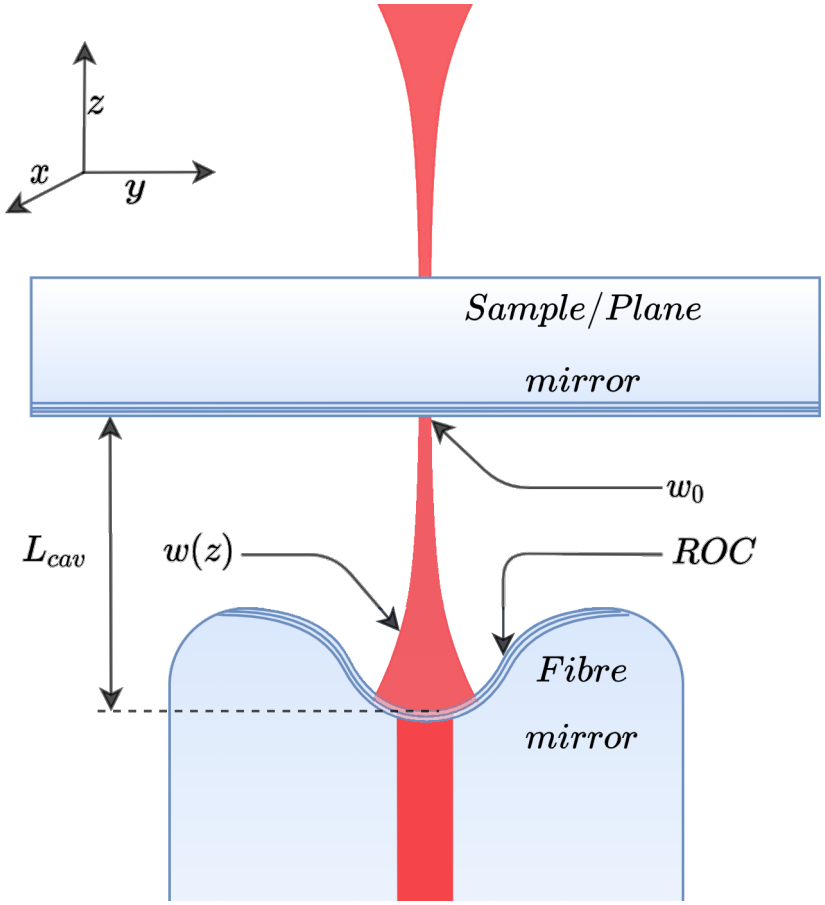

Figure 2.6: Schematic representation of a Gaussian beam in a microcavity with length L_{cav}. Where half of the width at the plane mirror is the beam waist (w_0). Half of the width of the beam anywhere in the microcavity is indicated with $w(z)$. The Radius Of Curvature (ROC) of the fibre dimple is also indicated. Sizes are not to scale.

For a Gaussian beam in a plane-concave microcavity there are 2 boundary conditions:

1. The beam waist ($R(w_0) = \infty$) is located at the plane mirror, that is $w_0 = w(0)$
2. The beam front curvature at L_{cav} is equal to the ROC of the concave mirror , that is $R(L_{cav}) = ROC$

With these two conditions the beam waist of the plane-concave microcavity is fixed and given by:

$$w_0 = \sqrt{\frac{2}{k}\sqrt[4]{L_{cav}\,(ROC - L_{cav})}} \tag{2.21}$$

$$= \sqrt{\frac{\lambda_0}{\pi}\sqrt[4]{L_{cav}\,(ROC - L_{cav})}}. \tag{2.22}$$

The fundamental Gaussian weight function (equation 2.15) is the simplest form of suitable solutions, which are known as the Hermite-Gauss modes. Using these solutions a more detailed solution to equation 2.12 is found and given by [23]:

$$U(\rho, z, t) = 4\pi \frac{w_0}{w(z)} H_m\left(\frac{\sqrt{2}x}{w(z)}\right) e^{-\frac{x^2}{w^2(z)}} H_n\left(\frac{\sqrt{2}y}{w(z)}\right) e^{-\frac{y^2}{w^2(z)}} e^{i\left(\alpha(z) - \frac{k\rho^2}{2R(z)} - kz + \omega t\right)}, \tag{2.23}$$

$$\alpha(z) = (1 + m + n)\arctan\frac{z}{z_R}. \tag{2.24}$$

Here $H_i(a)$ is the Hermite polynomial of degree i and the order of the Hermite-Gauss modes is indicated with m (x-direction) and n (y-direction). All the other functions in equation 2.23 are the same

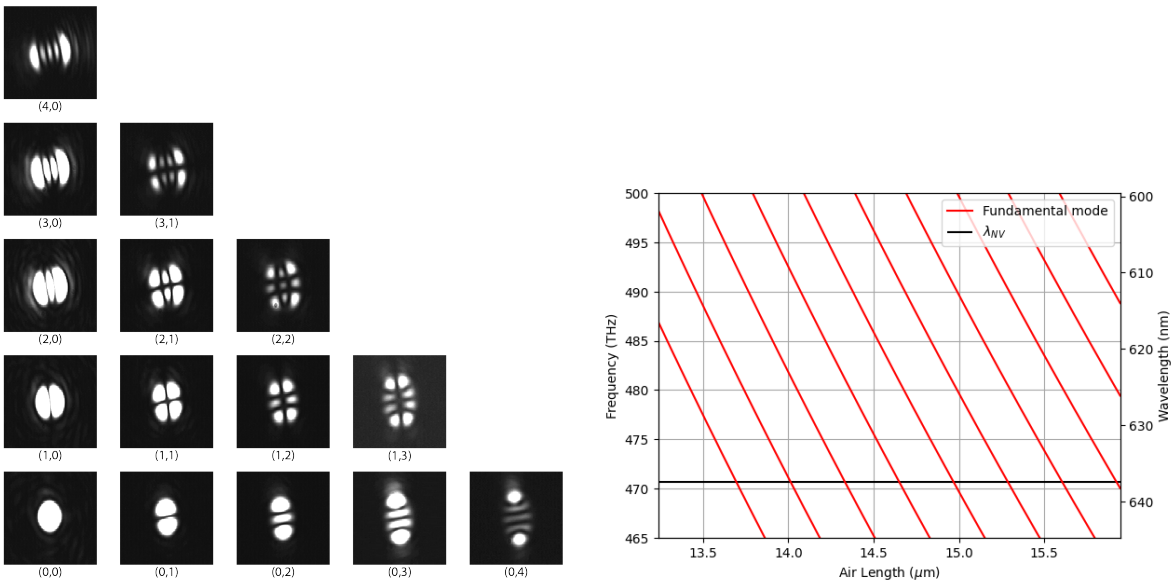

Figure 2.7: **(Left)** Hermite-Gauss modes in a plane-concave microcavity where the fundamental Gaussian mode ($m = 0, n = 0$) and the higher order Hermite-Gauss modes with order (m, n) can be seen on a CCD camera. Figure obtained from [33]. **(Right)** Theoretical transmission of the fundamental modes in a microcavity.

as in equation 2.16 except for the Gouy phase. The Guoy phase picks up an extra phase for higher order Hermite-Gauss modes. The spatial structure in x and y for these Hermite-Gauss modes is very characteristic and can be seen in Figure 2.7(left figure).

The plane-concave microcavity will be on resonance if the Hermite-Gaussian modes obtain a phase shift which is multiple of π when travelling from the plane mirror to the concave mirror (or vice versa). This gives the following resonance condition:

$$kL_{cav} - 2\alpha(z) = \pi(1 + \beta), \tag{2.25}$$

where $\beta = 0, 1, 2, 3, \ldots$. For a bare plane-concave microcavity the resonance frequency is then given by:

$$\nu = \frac{c}{4\pi L_{cav}}\left(2\pi(1+\beta) + (2m+1)\arccos\left(\sqrt{1-\frac{L_{cav}}{ROC_x}}\right) + (2n+1)\arccos\left(\sqrt{1-\frac{L_{cav}}{ROC_y}}\right)\right). \tag{2.26}$$

An ellipticity in the ROC of the concave mirror is accounted for by separately specifying ROC_x and ROC_y. The transmission of the microcavity will be maximal when the microcavity is on resonance. Meaning that the transmitted light shows the resonance frequency of the microcavity (Section 2.2.1). The resonance frequency for a bare microcavity as a function of the microcavity length is shown in Figure 2.7 (right figure). Now that a derivation for the resonance condition of the microcavity is found, it can be tuned on resonance with the ZPL of the NV^-. The reason for tuning the microcavity on resonance with the ZPL of the NV^- is given in the next section.

2.3. Purcell Enhancement of Quantum Emitters

If a quantum network is to be realised entanglement needs to be generated faster than it is lost. The entanglement generation with NV centres is currently limited by the coherent emission into the ZPL. To improve the entanglement rate, the amount of 'useful' indistinguishable photons needs to be increased. Using Purcell enhancement the emission into the ZPL can be enhanced. In this section the emission rate of an emitter without a microcavity present will be discussed first, followed by what happens when the emitter is embedded in a microcavity. This section of the theory has been retrieved from [23, 32, 34]

2.3.1. Spontaneous Transition Rates of Emitters

Emitters such as the NV⁻ can spontaneously emit a single photon by transitioning from an excited state to a lower energetic state. Using time-dependent perturbation theory, the rate of this "spontaneous" emission can be derived. The spontaneous emission rate for any emitter is given by Fermi's golden rule:

$$\Gamma_{i\to f} = \frac{2\pi}{\hbar} \left|\langle f_k| \hat{\mathcal{H}}_{int} |i\rangle\right|^2 D(\omega_k). \tag{2.27}$$

Here $\hat{\mathcal{H}}_{int}$ is the interaction hamiltonian between matter and radiation, in this case, the emitter and the photon vacuum. $D(\omega_k)$ is the photon density of electromagnetic modes with frequency ω_k. The initial state of the emitter is $|i\rangle = |e\rangle \otimes |0\rangle$ (the emitter is in it's excited state and there are no photons) and the final state after the emission is given by $|f_k\rangle = |g\rangle \otimes |1_k\rangle$ (the emitter is now in it's lower energetic state (for simplicity, the ground state is used) and there is a photon with wave vector k). If the wavelength of the transmitted photon is assumed to be considerably larger than the atomic length scale, the dipole approximation can be used. Using the dipole approximation the transition rate of an emitter in free space is given by:

$$\Gamma_{i\to f} = \frac{2\pi}{3} g^2 D(\omega_k), \tag{2.28}$$

where g is defined as the emitter-field coupling:

$$g \equiv \sqrt{\frac{\omega_k \mu_{ge}^2}{2\hbar\epsilon_0 V_0}}, \tag{2.29}$$

with μ_{ge} the transition matrix element, ϵ_0 the vacuum permittivity, V_0 the quantization volume (mode volume) and the photon density in equation 2.28 is:

$$D(\omega_k) = \frac{\omega_k^2 V_0 n^3}{\pi c^3}. \tag{2.30}$$

Here n is the refraction index of the material in which the emitter is embedded and c is the speed of light. Using equations 2.28-2.30, a free space spontaneous transition rate

$$\Gamma_{i\to f} = \frac{n^3 \omega_k^3}{c^3} \frac{\mu_{ge}^2}{3\pi\hbar\epsilon_0} \tag{2.31}$$

is obtained. This free space emission can be enhanced by coupling the emitter to a microcavity. Why the free space emission is enhanced will be explained in the next subsection.

2.3.2. Transition Rates of NV⁻ Centre in an Optical Cavity

The NV⁻ cannot only decay directly from the excited state to the ground state (in the zero phonon line (ZPL)) but can also decay by creating extra phonons (vibrational states) in the phonon sideband (PSB). Details of these transitions are given in Section 2.1. Both of these transitions have their own transition rate with a total rate of $\Gamma_{tot} = \Gamma_{ZPL} + \Gamma_{PSB}$. The only useful photons for entanglement generation are the photons in the ZPL, as they are well defined in frequency. Hence the branching factor into the ZPL,

$$\beta = \frac{\Gamma_{ZPL}}{\Gamma_{PSB} + \Gamma_{ZPL}} \tag{2.32}$$

should be increased to increase the entanglement generation rate. The transmission rate into the ZPL can be increased by modifying the density of states to a transition frequency ω_{ZPL} (equation 2.28). The density of states can be altered by placing the NV⁻ centre inside a microcavity. Some generic properties of the microcavity are discussed/repeated in this section. For a more detailed description, see Section: 2.2.

In a microcavity the electromagnetic field interferes constructively if the length of the microcavity is a multiple of half the wavelength of the light, hence:

$$L_{cav} = m\frac{\lambda}{2} = m\frac{c}{2n\nu}. \tag{2.33}$$

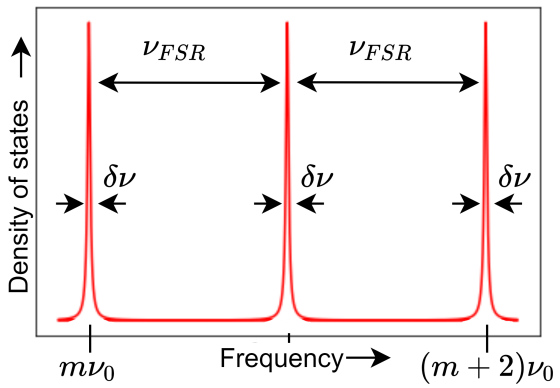

Figure 2.8: Density of states of the microcavity for different modes in the microcavity. The density of states looks like a Lorentzian around the resonance frequency $\nu_0 = m\frac{c}{2nL_{cav}}$ where m is a positive integer as mentioned in equation 2.33. The width of the Lorentzian is a measure of the amount of losses in the microcavity (see equation 2.34). All the resonant modes are spaced $\nu_{FSR} = \frac{c}{2nL_{cav}}$ apart.

Where $\lambda = \frac{c}{n\nu}$ is used, m is a positive integer and ν is the frequency of the mode inside the microcavity. This outcome can be recognized and is similar to the derivation of equation 2.8. Given equation 2.33, the frequency difference between two following modes is given by the free spectral range (FSR): $\nu_{FSR} = \frac{c}{2nL_{cav}}$. The optical microcavity is not perfect and experiences losses. Thus, the resonance mode will not be a delta peak function placed at $\nu_0 = m\frac{c}{2nL_{cav}}$, but will be a Lorentzian where the full width at half maximum (FWHM) is a measure for the losses. The FWHM can be generalised by:

$$\delta\nu = \frac{\kappa}{2\pi}, \tag{2.34}$$

where $\delta\nu$ is the FWHM (linewidth) and κ is the decay rate of the microcavity itself.

The density of states of a bare microcavity is therefore simply a repeating set of Lorentzian peaks, as shown in Figure 2.8 and given by:

$$D_{cav}(\omega) = \frac{1}{2}\frac{\frac{\delta\omega_0}{2}}{(\omega-\omega_0)^2 + \left(\frac{\delta\omega_0}{2}\right)^2}. \tag{2.35}$$

Where $\nu = \frac{\omega}{2\pi}$ is used. The maximum spontaneous transition rate of an emitter embedded in an optical microcavity is obtained when the microcavity and the emitter are on resonance, hence $\omega = \omega_0$. A gain in transition rate is given by using both the density of states of the microcavity (equation 2.35) and of free space (equation 2.30) when the emitter and microcavity are on resonance. The gain in transition rate is then given by the so called Purcell factor:

$$\begin{aligned} F_p &= \frac{\Gamma_{cav}}{\Gamma_{i\to f}} = \frac{\zeta^2}{1/3}\frac{D_{cav}(\omega_0)}{D(\omega_0)} \\ &= \frac{\zeta^2}{1/3}\frac{\frac{2}{\pi\delta\omega_0}}{\frac{\omega_0^2 V_0 n^3}{\pi c^3}} = 3\zeta^2\frac{2c^3}{\delta\omega_0\omega_0^2 V_0 n^3} \\ &= 3\zeta^2\frac{1}{\pi^2\delta\nu}\frac{4V_0c^3}{n^3\nu^2} \\ &= 3\zeta^2\frac{3c^3}{4\pi^2 n^3\nu^3}\frac{Q}{V_0}, \end{aligned} \tag{2.36}$$

where in the last step the definition of the quality factor (number of optical cycles before the energy of the mode drops a factor of 1/e of its initial value) $Q = \frac{\nu}{\delta\nu}$ is used. Furthermore, the mode volume

(for a bare optical cavity) is defined as [23]:

$$V_0 = \frac{\pi w_0^2}{4} L_{eff}, \tag{2.37}$$

where L_{eff} is the energy distribution length [35]. For a bare microcavity (no diamond membrane) $L_{eff} = L_{cav}$. In equation 2.36 ζ indicates the overlap between the electric dipole moment of the electronic transition ($\hat{d}$) and the polarization of the mode in the microcavity ($\hat{e}$). In free space ζ averages out to 1/3, see equation 2.28.

By embedding an emitter in a microcavity one can thus enhance the emission rate of the emitter if $F_p > 1$. This effect is called the Purcell effect and is at its highest for low mode volumes and high quality factors. The new branching ratio into the ZPL is now given by :

$$\beta_{cav} = \frac{F_p \Gamma_{ZPL}}{F_p \Gamma_{ZPL} + \Gamma_{tot}}. \tag{2.38}$$

3

Experimental Setup

As has been mentioned in the introduction of this report, reducing vibrations is very important to maintain an enhancement of emission into the ZPL of the NV^-. In a novel setup, vibrations created by the cryostat (or other sources) are to be suppressed using two separate systems. First, the vibrations are reduced by the design of the High Inertia Low Acceleration (HILA) cryostat. Further vibration reduction is achieved with a passive vibration isolator stage from Janssen Precision Engineering (JPE). This chapter entails a description of the experimental setup used in this thesis. First, the experimental setup of the microcavity and the method of creating a microcavity is discussed in Section 3.1. After which the passive vibration stage from JPE and the HILA system are discussed in Section 3.2. This chapter will end with a description of the optical excitation and detection paths (Section 3.3).

3.1. Experimental Setup of the Microcavity

A microcavity is formed with two opposing mirrors. In the setup used in this thesis, the microcavity is formed by a fibre end with a mirror coating and a flat mirror (see Section 2.2.3). To make sure that the light in the microcavity does not escape, a dimple is manufactured in the fibre tip using a CO_2 ablation setup. The analysis of an exemplary fibre dimple, used in this thesis, can be found in Appendix A. After the dimple (with a certain ROC) has been created the fibre is coated with either: a high reflectivity coating (Design: 50 ppm, $\lambda = 600$-680 nm) or a low reflectivity coating (Design: 700 ppm, $\lambda = 600$-680 nm). A high (Design: 50 ppm, $\lambda = 600$-680 nm) or low (Design: 290 ppm, $\lambda = 600$-680 nm) reflectivity coated flat mirror can be chosen as the second mirror of the microcavity. On the flat mirror, diamond membranes can be placed which are bonded to the mirror by Van der Waals forces. The mirror is glued to a mirror holder which is mounted on a cone in which a stack of positioners is located. The JPE CS02 – CRYO STAGE 02 nanopositioner system has two identical positioners for lateral movement. The positioners are rotated 90° with respect to each other to move in the x and the y direction. The lateral positioners are stacked on top of a third positioner which allows movement in the z-direction. The JPE nanopositioner stack also includes a scanning piezo which can change the z-position continuously. This scanning piezo will be referred to as the ”coarse piezo”. A fibre holder can be placed on top of the positioner stack to obtain great control over the location of the fibre (in lateral and z-direction). To ensure that the microcavity length can be scanned at high frequency and that active locking (using a feedback loop) is a possibility, the fibre is glued to a high bandwidth piezo (noliac, shear plate CSAP02). The high bandwidth piezo will be referred to as the ”fine piezo”. A schematic representation of the micro-cavity and the JPE passive vibration isolator can be found in Figure 3.1.

The fibre is glued to both the fibre holder and the high bandwidth piezo with a high resonance frequency (idea originates from [36, 37]). The process of mounting the fibre to the fibre holder is best described with the following steps (see Figure 3.2 for a visual representation of the steps):

1. Glue a piece of alumina (Al_2O_3) to the fibre holder using stycast 2850 (and catalyst LV24). This is to electrically isolate the locking piezo from the fibre holder (made of titanium) as alumina is an electrical insulator but has relatively high thermal conductivity [38].

2. Glue a piece of copper foil to the alumina using stycast 2850.

3. Glue the high bandwidth piezo to the copper foil using silver glue (Lake Shore silver epoxy ESF-2-5) to ensure electrical conductivity between the copper foil and the high bandwidth piezo.

4. Glue a Teflon wire to the top side of the high bandwidth piezo and another Teflon wire to the copper foil. This way voltage can be applied to the high bandwidth piezo. The same glue is used as in step 3.

5. Glue the fibre to the high bandwidth piezo using stycast 2850. In this process, the fibre must remain perpendicular with respect to the fibre holder to reduce the angle between the static mirror and the fibre. This will result in a less clipping losses for larger L_{cav} (Section 4.4). The angle is monitored using a blue cross, see Figure 3.2f

6. Glue the fibre to the fibre holder using stycast 2850. This ensures a stable fibre that is fixed on two positions on the fibre holder.

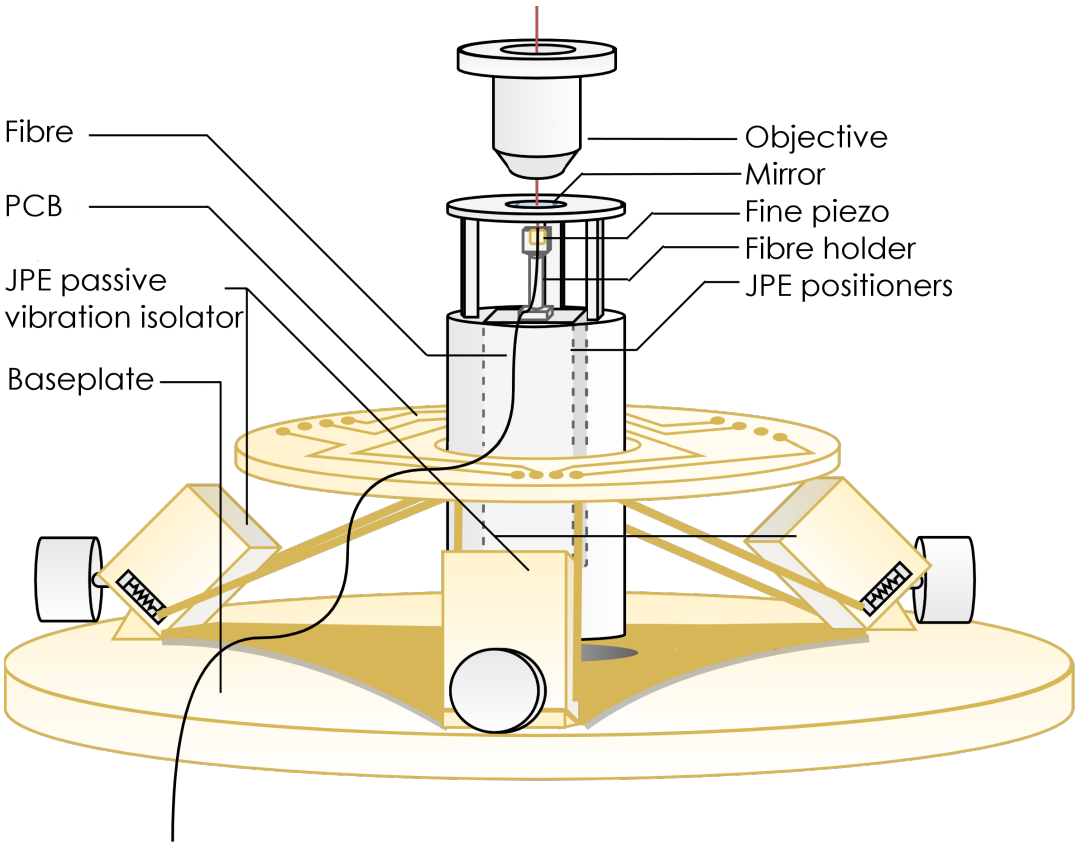

Figure 3.1: Schematic overview of the microcavity setup. The JPE passive vibration isolator is mounted on the HILA baseplate. The passive vibration isolator has been simplified in the schematics and ensures that the cylinder on which the microcavity is mounted floats (Section 3.2). The Printed Circuit Board (PCB) is connected to the floating cylinder and can be used to make an electrical connection to the JPE positioners, the temperature sensor at the sample and the high bandwidth piezo. The fibre is glued to the fibre holder and to the high bandwidth piezo to ensure a stable fibre that can scan at high frequency in the microcavity length direction. The plane mirror is glued (using heat-conducting glue) to the mirror holder which is placed on the floating cylinder. The entire setup described above is thermally connected to the first stage of the HILA cryostat system and will go down to ~ 6 K. Extra thermal straps connecting the mirror holder and the baseplate are present but are not depicted in the schematic overview. The objective is placed above the static mirror and can be moved in x,y and z using 3 PI positioners. The objective stage is not placed on the first stage of the system and will stay at room temperature. Between the microcavity and the objective, a radiation shield is placed and is thermally connected to the second stage of the HILA cryostat which has a temperature of ~ 30 K. The entire setup is placed in the vacuum chamber of the HILA cryostat and can be put to vacuum.

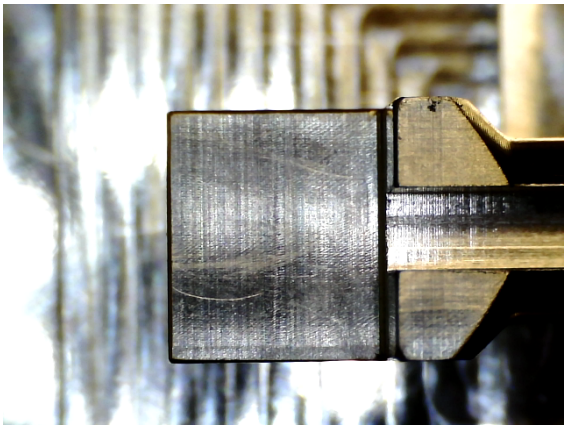

(a) Bare titanium fibre holder

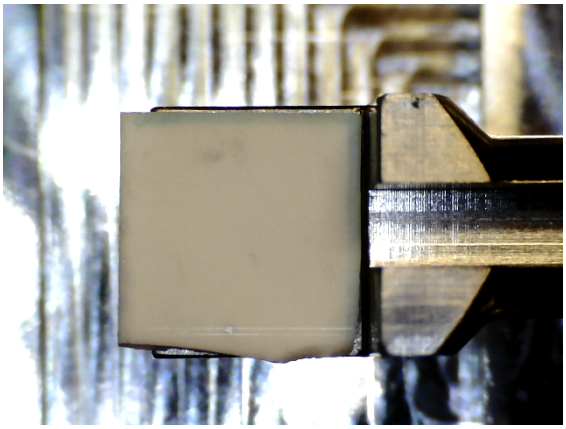

(b) Step 1: glue alumina

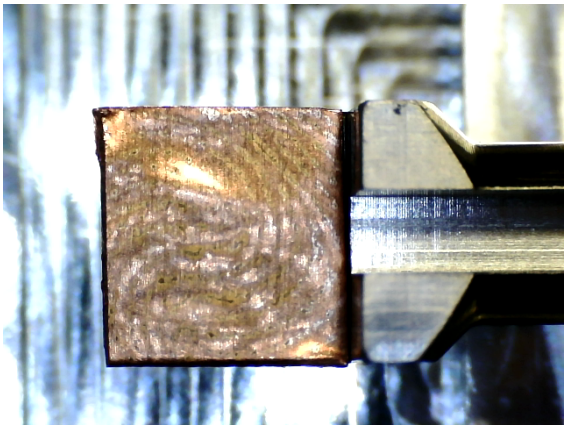

(c) Step 2: glue copper foil

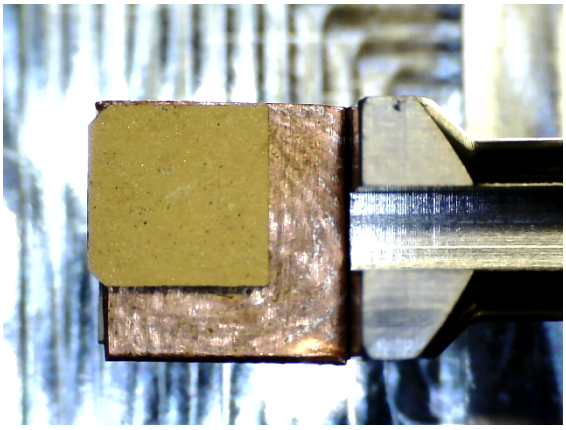

(d) Step 3: Glue high bandwidth piezo

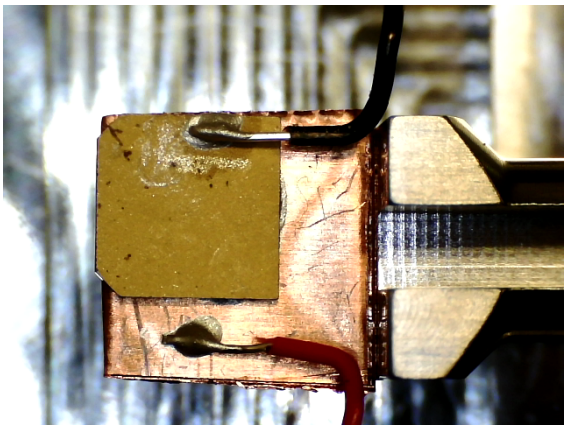

(e) Step 4: Glue Teflon wires

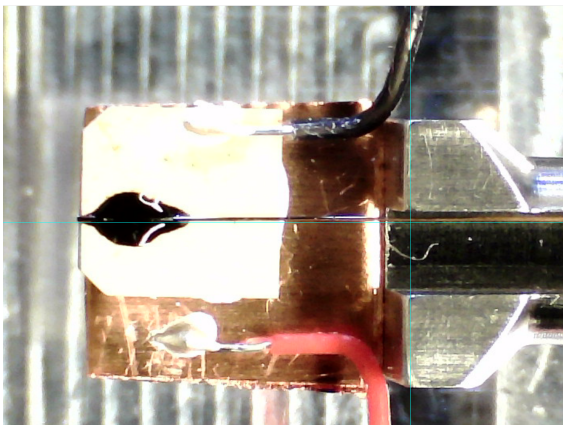

(f) Step 5: Glue fibre to high bandwidth piezo

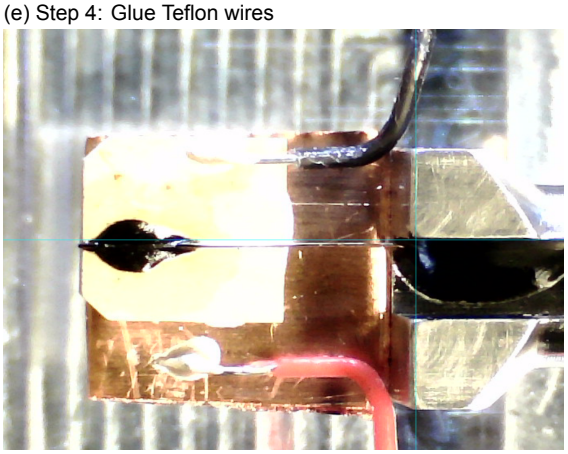

(g) Step 6: Glue fibre to fibre holder

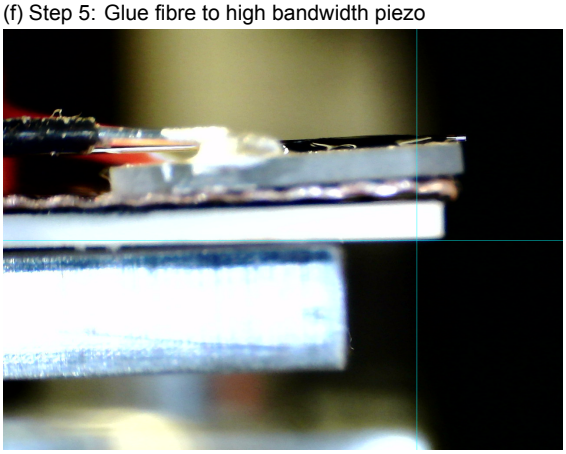

(h) Side view of fibre holder after all the steps

Figure 3.2: Production of the fibre holder with high bandwidth piezo and fibre.

After these steps, the fibre holder can be mounted on the JPE positioner stack and the mirror holder can be placed on top of the surrounding cylinder. Now the microcavity can be formed by slowly moving the fibre towards the flat mirror. To check the approximate microcavity length, a red laser coming from the objective side (detection path) is focused on the static mirror. The reflected light of the mirror is collected using the camera in the detection setup (see Figure 3.5). The position of the objective is noted and the objective will now be focused on the fibre mirror. Subtracting the distances gives an approximate microcavity length. When the approximate distance is smaller than $\sim 25\mu$m the supercontinuum laser can be used to determine the exact length of the microcavity (see Section 4.1).

3.2. Passive Vibration Isolation

In order to realise high microcavity length stability, the cavity is mounted on two passive vibration isolator stages. Both vibration isolator stages will be discussed in the next subsections. As the main focus of this thesis is not the design of these stages, limited details will be given.

3.2.1. JPE Passive Vibration Isolator

As mentioned previously in this chapter, the microcavity is mounted on a passive vibration isolator from Janssen Precision Engineering (see Figure 3.1). The vibration isolator acts as a low pass filter for vibrations. The vibration isolator uses 3 identical spring modules connected to the floating cylinder containing the JPE nano-positioner stack. A detailed drawing of such a module is shown in Figure 3.3. The custom design from JPE uses several (leave) springs to suppress vibrations not only in the z-direction but also in both lateral spacial directions. All 3 JPE spring modules include a small motor that can rotate to ”push” the entire JPE positioner stack up or down. Using these motors, the positioner stack (and thus the microcavity) can be put to a position in which it floats. In this floating condition, the vibration isolator should suppress vibrations above its cut-off frequency (designed to be below $1Hz$). Using this motor the microcavity can be tuned to different levels of passive vibration isolation. These motors can be addressed at cryogenic temperature, as the floating condition will vary when going from room temperature to cryogenic temperatures.

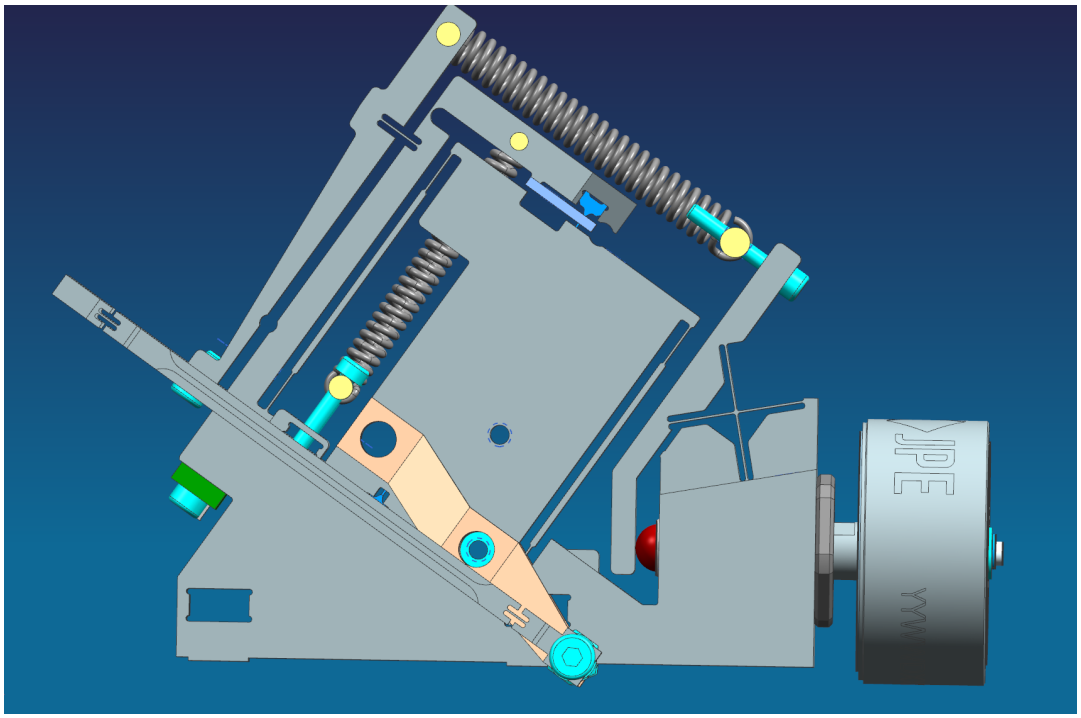

Figure 3.3: The JPE spring module. 3 off these modules are connected to cone supporting the microcavity in order to isolate vibrations from the environment. By turning the JPE motor (right bottom of the figure) the upper most spring is stretched and this will lead to an upwards movement of the cone supporting the microcavity.

3.2.2. HILA Cryostat

The entire microcavity setup is mounted on the baseplate of the HILA cryostat from Montana Instruments. The cryostat is a closed-cycle optical cryostat with a base temperature of ~ 6 K. The HILA system has two main advantages over other cryostats. First, the cold head (which is the major source of vibrations) is outsourced to a support rack standing next to the optical table. By separating the cold head from the optical table, the energy transfer between the cold head and the optical table (and thus the microcavity) is reduced. Second, the baseplate inside the HILA is separated from the optical table using a spring system and electromagnets. Using these electromagnets the baseplate can be automatically levelled. With the HILA system, the baseplate should be minimally coupled to the optical table and act as a low pass filter for vibrations.

3.3. Optical Excitation and Detection Setup

The optical setups are displayed in Figure 3.4 and Figure 3.5, which show the excitation path and the detection path respectively. First, the excitation path will be described. For this thesis 4 different lasers are used:

1. Toptica DL Pro ($637nm$): referred to as the DL laser.
2. New Focus laser ($637nm$); referred to as the NF laser.
3. Pulsed Cobolt laser ($532nm$): referred to as the green laser
4. NKT Femptopower supercontinuum laser ($450nm-2\mu m$): this is a high power pulsed laser that is limited to a range of $600nm-700nm$ using spectral filters (see bottom left of Figure 3.4). Referred to as the white light source/supercontinuum laser.

Both red lasers are directed to a wavemeter using a 99:1 fibre beam splitter to monitor the exact wavelength of the lasers. After which one fibre Acoustic-optic modulator (AOM) is used to control the power into the microcavity (and for further NV sequences). Eventually, two AOMs will be placed after each other for better control. After the AOM a Phase Electro-Optic Modulator (PEOM) can be placed in the excitation path to generate sidebands using an RF source at the sideband frequency. Using a fibre collimator (Schäfter+Kirchhoff) the laser light in the fibre is converted to a collimated free space laser beam. In the free space optics path of the red laser, a 50:50 beam splitter is placed such that the reflected light from the microcavity can also be monitored with a photodiode. As no measurements are performed where the reflected signal needs to be measured, the 50:50 beam splitter is always flipped out during the measurements described in this thesis. The red lasers and the green laser are combined using a dichroic mirror and directed towards a single-mode fibre coupler and connected to the microcavity fibre. The supercontinuum laser can also be directed (after filtering the wavelengths) to the microcavity fibre. Changing between the supercontinuum laser and the green/red lasers has to be done manually. In the future, a switch box will make sure that switching between all the lasers can be done remotely and the excitation path can be fully automated and closed off.

The transmitted light from the microcavity is collected with the detection path (schematically shown in Figure 3.5). The first step in the detection path is an objective that can be moved in 3 dimensions using 3 linear stages from Physik Instruments (PI) (Q-545 Q-Motion® Precision Linear Stage). After the objective stage, the light is directed to the optical table using a rack with 3 mirrors. These mirrors are used to align the transmitted signal to 2 different pinholes (see Figure 3.5). Using this technique most of the optics does not have to be touched once the transmitted beam is aligned to the pinholes. The detection setup consists out of multiple switchable paths, beginning with a camera path that allows for imaging of diamond samples in the microcavity. After the second pinhole, a switchable mirror is used to switch between a path used for measurements on the NV (bottom left side of Figure 3.5) and a path used for measurements on the microcavity properties (middle right part in Figure 3.5). The microcavity properties are analysed using a spectrometer (determining the microcavity length) and a photodiode (determining the linewidth and actively stabilising the microcavity length). As no experiments are performed which include measurements on an NV centre, the NV side of the detection path is not utilised during this thesis.

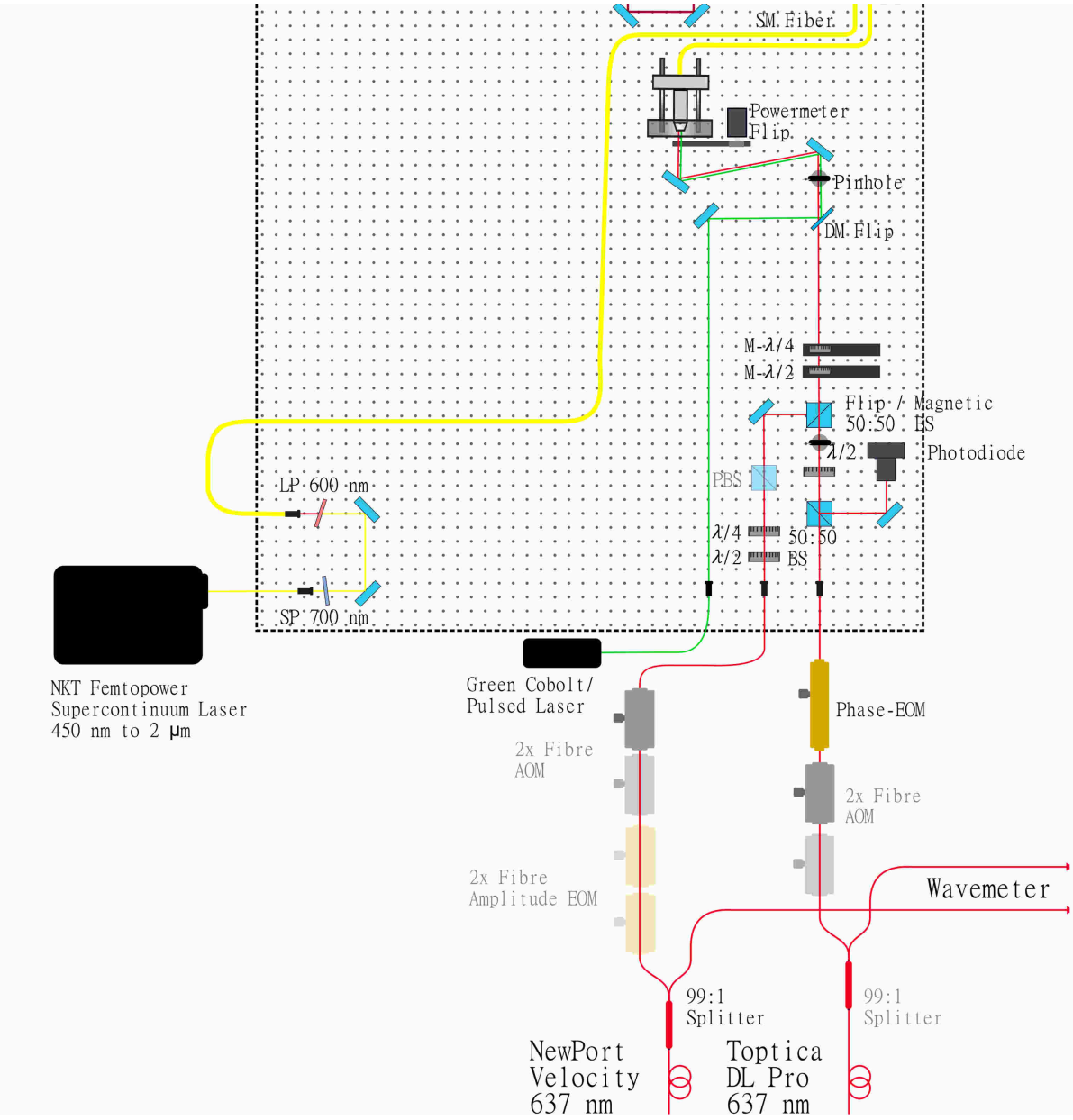

Figure 3.4: The excitation path, including 4 different lasers. (1.) NKT Femtopower, which is directed to spectral filters to only keep light between $600 - 700nm$. (2.) Green Cobolt laser, which is combined with the two red lasers. (3.) NewPort Velocity, which is polarized using 2 static waveplates. The NewPort Velocity is used in this thesis to measure the linewidth of the microcavity but its final use is NV control (spin-pumping etc.). (4.) Toptica DL Pro, which is polarized using 3 different waveplates (one static, two dynamic). The lasers are aligned using two pinholes and by analysing the laser power going into the microcavity. A power meter can be flipped in front of the single-mode fibre coupler to calibrate the green laser and both red lasers. Furthermore, using this power meter (and by placing a power meter before the cavity fibre) the efficiency of the excitation path can be determined. A 50:50 beamsplitter can be flipped in on the Toptica path for detection of the reflected light. The somewhat transparent equipment is still to be built.

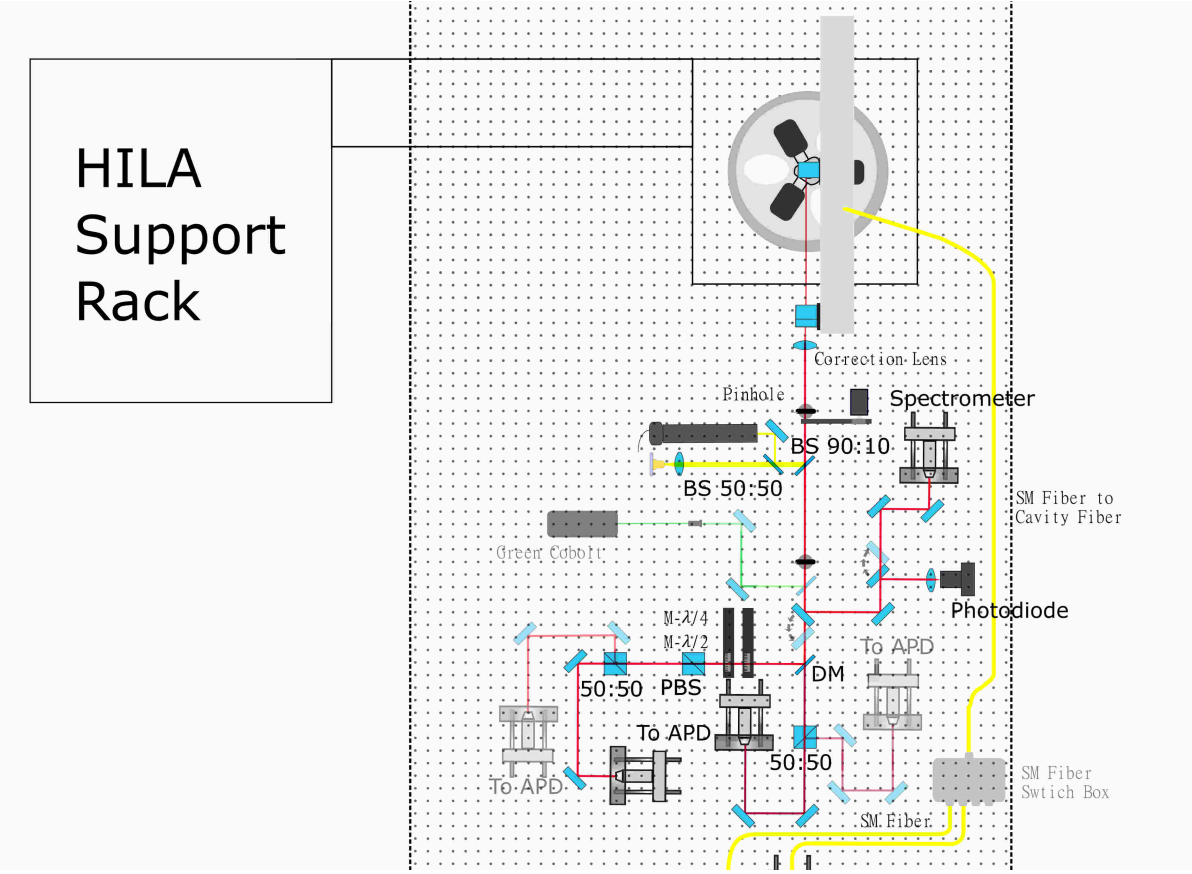

Figure 3.5: The detection setup. The transmitted light of the microcavity is directed back to the optical table using an objective and 3 different mirrors which can be used to align the transmitted light to the pinholes. The detection setup consists out of 3 major paths. (1) Camera path: A 90:10 beam splitter can be flipped in to observe the diamond samples using a led light and a camera. Furthermore, the camera can be used to focus on the fibre tip or the flat mirror. (2) NV path: A mirror can be flipped out to perform measurements on the NV centre (left bottom part of the figure). (3) Microcavity characterisation path: When the mirror (to the NV path) is flipped in, the light is directed to the microcavity path. Using this path the properties of the microcavity can be analysed. A spectrometer is used to measure the microcavity length. A path to the photodiode can be flipped in to measure the linewidth and allow us to lock the microcavity to a certain microcavity mode. The somewhat transparent equipment is still to be built.

4

Characterisation of Fundamental Microcavity Properties

To generate Purcell enhancement, the microcavity must be tuned exactly on resonance with the ZPL of the NV^-. In order to tune the microcavity on resonance, the properties of the microcavity must be well understood. To obtain a great understanding of the new setup, several experiments are performed to characterise the properties of the open air Fabry-Pérot microcavity. Most of the characterisation of the microcavity is performed before the installation of the HILA cryostat. Hence a mock-up base-plate (mounted on the optical table, see Figure E.2) is manufactured on which the microcavity setup is mounted. Thus, the measurements and results shown in this chapter are performed at atmospheric pressure and at room temperature unless mentioned otherwise.

First the method of measuring the microcavity length (L_{cav}) is discussed in Section 4.1, followed by Section 4.2 describing different measurements of the linewidth ($\delta\nu$) of a microcavity mode. In Section 4.3 the results of a changing cavity length as a function of temperature is shown. Section 4.4 will show the finesse as a function of the microcavity length. Section 4.5 will state a brief summary of the found results in this chapter.

4.1. Microcavity Length Measurement

To measure the length of the microcavity, L_{cav}, the supercontinuum (white light source) is connected to the microcavity fibre. As explained in Section 2.4 the microcavity will only transmit light when $L_{cav} = m\frac{\lambda}{2}$ (equation 2.8) with m being an integer. A fairly simple method of determining L_{cav}, is to obtain the difference in wavelength between the transmitted peaks of the fundamental modes. The difference in wavelength/frequency between the two consecutive fundamental modes (FSR) is inversely proportional to the length of the microcavity ($L_{cav} = \frac{c}{2n\nu_{FSR}}$). For this method the detection path will direct the transmitted light of the microcavity to a fibre coupler, guiding the light to a spectrometer (see Figure 3.5). Using the spectrometer, the intensity for each wavelength is recorded. By aligning the detection path in such a way that the fundamental mode has the highest intensity on the spectrometer, a single spectrum can be recorded and used to determine L_{cav}. An example of such a spectrum is shown in Figure 4.1. Here the red crosses are the fitted peaks of the fundamental mode which are used to determine the length of the microcavity.

A more sophisticated way to determine the length of the cavity (and other properties) is by applying a DC voltage to the coarse piezo of the JPE positioner stack. By applying a voltage to the piezo L_{cav} will change (increase in voltage results in a decrease of L_{cav}).

An intensity spectrum for different voltages can be seen in Figure 4.2 (middle figure). From the intensity plot, all the different modes (fundamental and higher-order modes, see Theory Section 2.2.3) can be extracted by analysing the intensity spectrum and track the movement of the bands by analysing the spectrum at higher and lower voltages [39]. The extracted fundamental and higher-order modes can also be seen in Figure 4.2 (lower figure). To calculate the length of the microcavity only the fundamental modes are of importance, and thus the higher-order modes can be removed for the analysis. Next, the

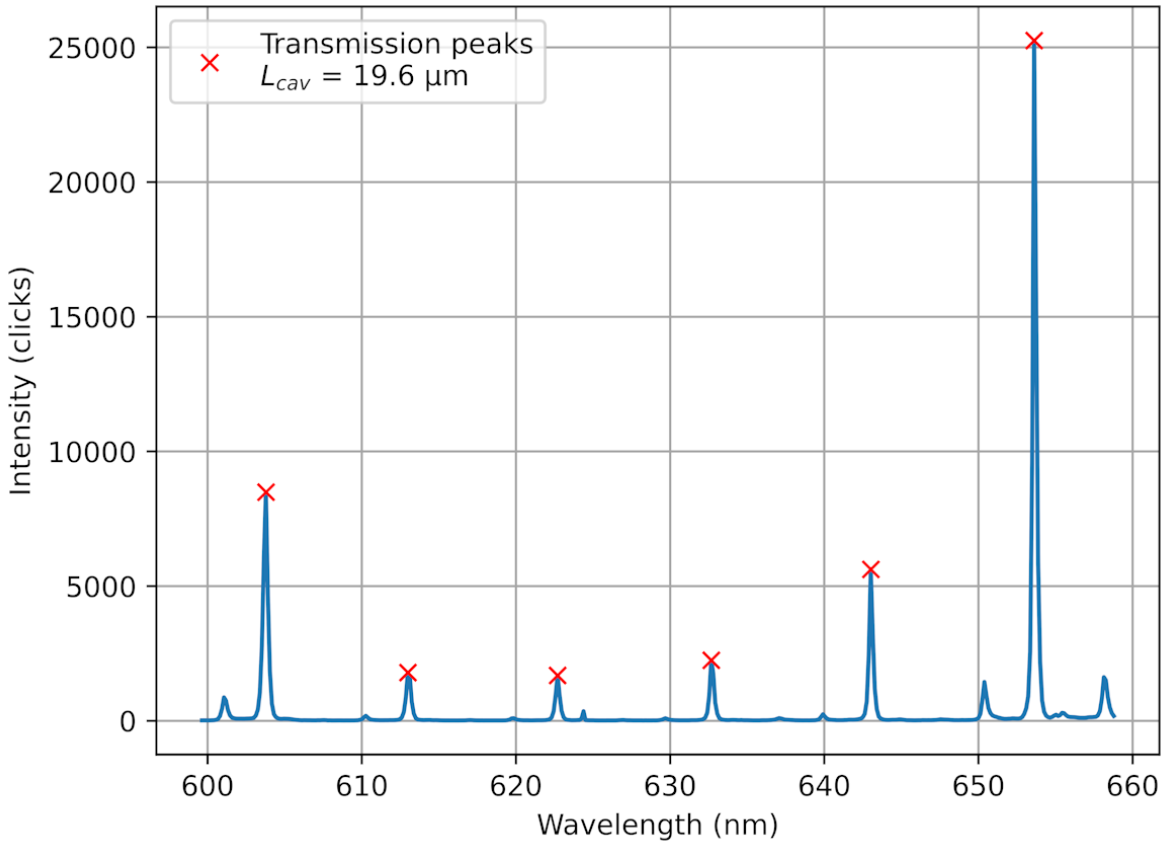

Figure 4.1: A single transmission spectrum of the cavity when the white light source is connected. The blue line indicates the amount of clicks the spectrometer detects for an exposure time of $5s$. The red crosses indicate the peak of the fitted fundamental mode. The peaks are used to determine the length of the cavity, which is $19.6\mu m$ for this particular spectrum.

non-linearity between the applied voltage on the piezo and the length increase of the piezo needs to be taken into account. Since the distance between subsequent bands will be $\frac{\lambda}{2}$ by definition, a relation between the applied voltage and a relative length increase is computed. After performing the voltage to relative length conversion, the resulting fundamental modes can be fitted using equation 2.26 with the fitting parameter $L_{cav} = L_{abs} + L_{rel}$. Using this method a length dependence of the different modes in the microcavity is obtained.

With the fitted fundamental modes, one knows which voltage to apply to get to a certain L_{cav} and to get a certain fundamental/higher-order mode. Using the DL laser with $\lambda_{laser} = \lambda_{NV} = 637nm$ the microcavity can be checked when it will be on resonance with the ZPL of the NV^-. The transmitted light of the microcavity can be analysed by directing the detection path to the photodiode (see Figure 3.5). When an AC voltage with a certain frequency, amplitude and offset is applied to the coarse piezo, the length of the microcavity will continuously scan over the different modes at λ_{NV}. This results in a transmission peak at the time that the microcavity is on resonance with a certain mode. The transmitted signal can in its turn be analysed and fitted with a Lorentzian to determine the linewidth of that particular mode. More on this in Section 4.2. At every resonance, a picture can be taken by flipping in the camera path (same modes as Figure 2.7). The PD signal, a zoom-in of the PD signal and the camera images at different microcavity lengths can also be seen in Figure 4.2 (top figure).

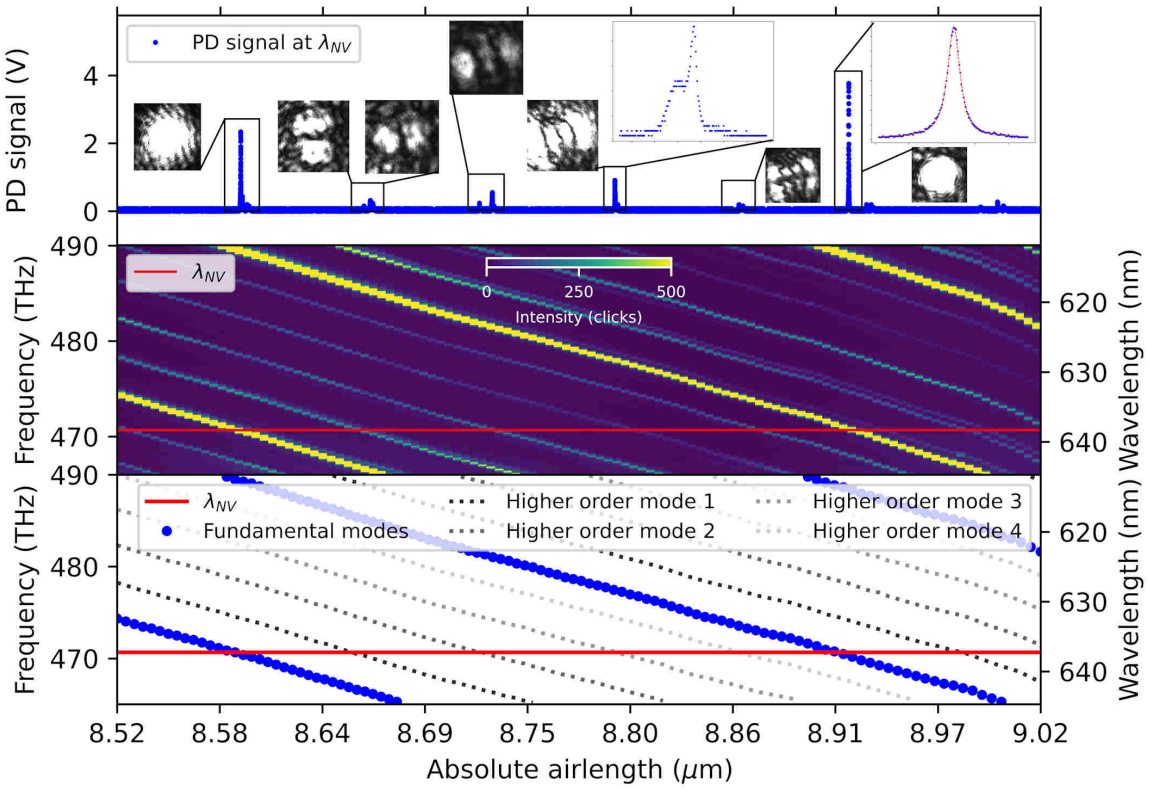

Figure 4.2: Figure inspired from [40, Figure 4a]. **(Top)** The PD signal when a red laser with $\lambda_{laser} = \lambda_{NV} = 637nm$ is connected to the microcavity fibre. An AC voltage is applied on the coarse piezo with $f = 200Hz$, $V_{pp} = 0.36V$ and $V_{offset} = 0.82 \rightarrow L_{cav} \approx 8.85\mu m$. In the inset, the different modes detected by the camera are shown. A zoom-in of the fundamental mode is shown together with a Lorentzian fit (red), another inset shows a zoom-in of the PD signal of a higher-order mode without a fit. **(Middle)** The intensity plot is measured by the spectrometer, for every applied voltage on the piezo a spectrum is taken. The incremental voltage step is $0.002V$, the exposure time of the spectrometer is set to $1500ms$ and a waiting time between setting the piezo voltage and taking the spectrum is $500ms$. The red line indicates the wavelength of the ZPL of the NV^- and thus the wavelength of the used red laser. **(Bottom)** The extracted fundamental and higher-order modes can be fitted to obtain the conversion between applied piezo voltage and microcavity length. Here "Higher order mode i" indicates a group of higher-order modes with the same degeneracy. Again the red line indicates the wavelength of the ZPL of the NV^- state.

To determine the length of the microcavity, only the fundamental modes are important and the higher-order modes can be disregarded. However, the higher-order modes can be used to determine the radius of curvature of the fibre dimple. Inverting the relation between the resonance frequency and the ROC from equation 2.26 and assuming that the dimple in the fibre is spherical ($ROC = ROC_x = ROC_y$) the relation:

$$ROC = \frac{L_{cav}}{1 - \cos\left(\frac{2\pi L_{cav}\Delta\nu_{mn}}{(m+n)}\right)^2} \tag{4.1}$$

is obtained. Here m and n indicate the order of the Hermite-Gauss modes (see Section 2.2.3) and $\Delta\nu_{mn}$ indicates the frequency difference between the higher-order modes m and n which belong to a certain fundamental mode q. By analysing the frequency difference of the higher-order modes for every microcavity length, the ROC of the fibre dimple can be computed. Figure 4.3 shows a histogram of all the found ROCs, together with a Lorentzian fit from which a ROC$= 20.140 \pm 0.283\mu m$ is obtained. From a previous fibre analysis (after manufacturing) a ROC $= 23.83\mu m$ is measured (see appendix Figure A.1). The difference between these 2 found ROCs can be due to an angle between the fibre

and the plane mirror. This can result into a smaller effective ROC, more on this in Section 4.4. Another possible explanation for the difference in ROC can be due to the deposited DBR layers on the fibre. The analysis from appendix A.1 is performed before the DBR is deposited. The DBR also has a finite thickness of a few μm which can thus be an explanation for the difference in ROC (the exact layer thickness is not known, a similar coating of which the thickness is known had a total layer thickness of $3.66\mu m$).

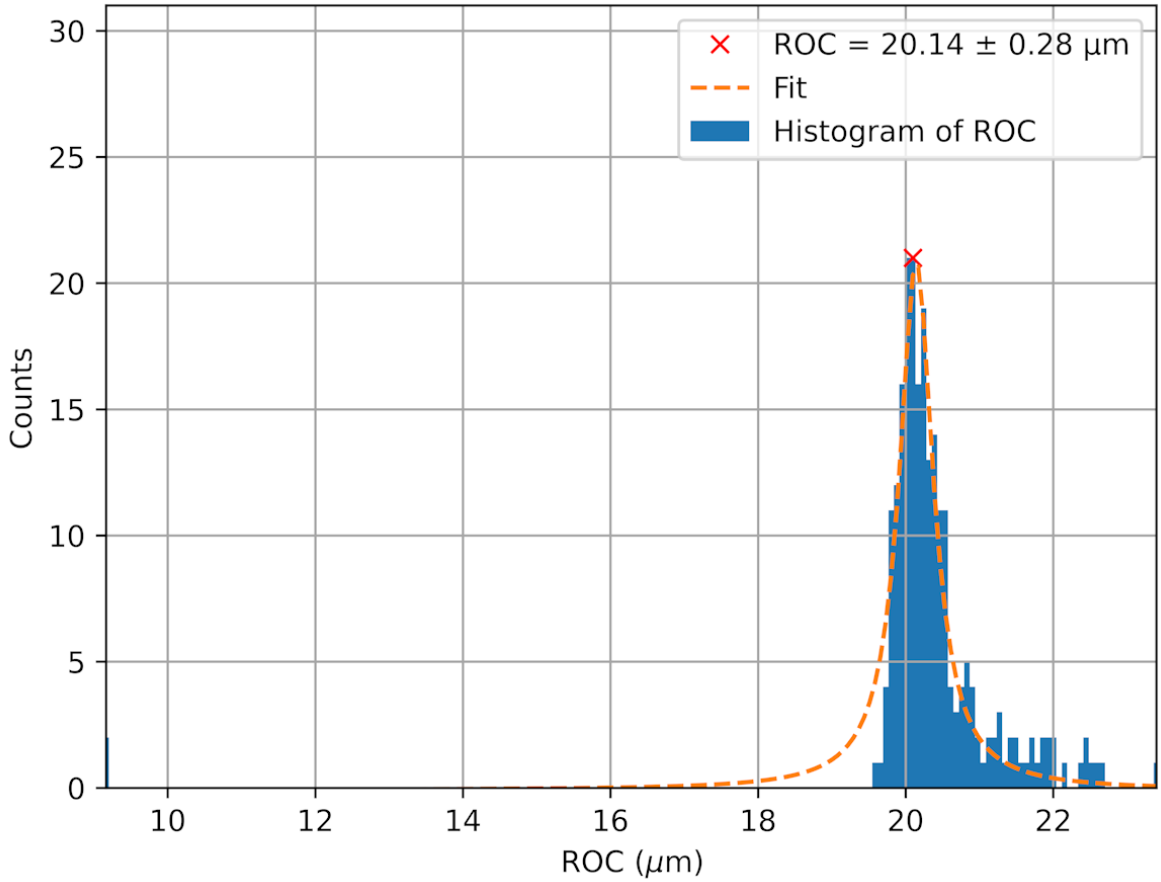

Figure 4.3: Histogram of the computed ROC from the data displayed in Figure 4.2. A Lorentzian curve has been fitted to the data and results in ROC= $20.14 \pm 0.28\mu m$

Another important microcavity parameter is the linewidth. The linewidth is defined as the Full Width at Half Maximum (FWHM) of the cavity mode. How to measure the linewidth of a certain cavity mode will be described in detail in the next section.

4.2. Microcavity Linewidth Measurement

Since a microcavity is never completely perfect, there will be some losses for a certain mode in the cavity. That is why the transmission of a microcavity will never be a delta peak at a certain L_{cav}. To determine the linewidth of a microcavity mode, the length of the microcavity must be scanned over its resonance length. In order to do that an AC voltage can be either applied to the coarse piezo (JPE) or the fine piezo. By continuously scanning the microcavity length, a Lorentzian transmission peak can be measured on the photodiode. The transmission peak will be located at a certain time in the AC signal and can be fitted with a Lorentzian. With this fit, a linewidth in time can be computed. However, to convert this linewidth in time to the actual physical linewidth of the microcavity mode in frequency, a known reference signal is needed. During this thesis, two reference signals are used and will be discussed separately (Section 4.2.1 and 4.2.2). The first method is to use a Phase Electro-Optic Modulator (PEOM) to generate sidebands to the transmission peak.

4.2.1. Determining Linewidth with Modulated Sidebands

Including a PEOM in the optical excitation path of the DL laser (see Figure 3.4) will generate sidebands to the transmission peak. These sideband transmission peaks are separated in frequency from the main transmission peak. The frequency spacing between these peaks is exactly the modulation frequency applied to the PEOM [41]. These modulated sidebands can be used as a reference in measuring the linewidth. First, the linewidth is determined in time using a non modulated transmission peak. After which the PEOM is used to determine the conversion between time and actual frequency. In Figure 4.4 the (non) modulated transmission signals of the PD with fits are shown.

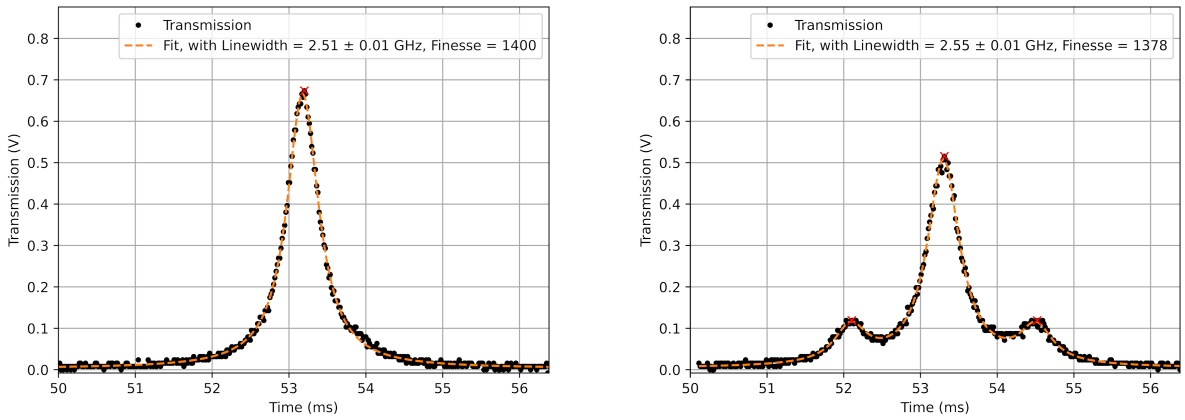

Figure 4.4: **(Left)** Photodiode signal of the fundamental mode with a Lorentzian fit. The red cross indicates the peak of the transmission signal. The AC signal applied to the coarse piezo has $f = 600Hz$, $V_{offset} = 1.835V \rightarrow L_{cav} = 13.6\mu m$ and $V_{pp} = 0.2V$ **(Right)** The same settings for the AC signal only now the laser has modulated sidebands with a sideband frequency of $6GHz$ and where the sideband power is $17dBm$. The red crosses indicates the peaks of the main transmission peak and sideband peaks.

There is a downside to measuring the linewidth by using modulated sideband: there is a maximum linewidth that can be measured. In the setup used in this thesis, the maximum applied modulation frequency is 6 GHz. If the linewidth of the cavity exceeds this modulation frequency the sidebands will be inside the main transmission peak. Therefore, the reference signal is lost and the linewidth cannot be determined with high accuracy. Hence, another method needs to be used to determine the linewidth of microcavity modes in which the linewidth exceeds 6 GHz.

4.2.2. Determining Linewidth with a Second Laser

The second method of determining the linewidth uses the NF laser as the reference signal. Both the DL and NF laser are coupled to the cavity fibre. Both lasers are red but differ a few hundred GHz in frequency. By scanning the cavity length over the resonance length of both lasers, two transmission peaks are visible. The difference between these transmission peaks in time can be converted to frequency by measuring the exact wavelength of both lasers. The wavelengths of both lasers are recorded using a wavemeter (see Figure 3.4) and the transmission signal of the cavity is again measured with a PD. Both the transmission peaks can be fitted with a Lorentzian which will give the linewidth in time. Then using the known frequency difference between both lasers, the linewidth in time is converted to a linewidth in frequency for both transmission peaks. The PD signal (together with the fits) of the DL and NF transmission peaks are shown in Figure 4.5.

Using the methods described in Section 4.1 and 4.2. More cavity properties can be analysed. For example, the temperature dependence of the microcavity length.

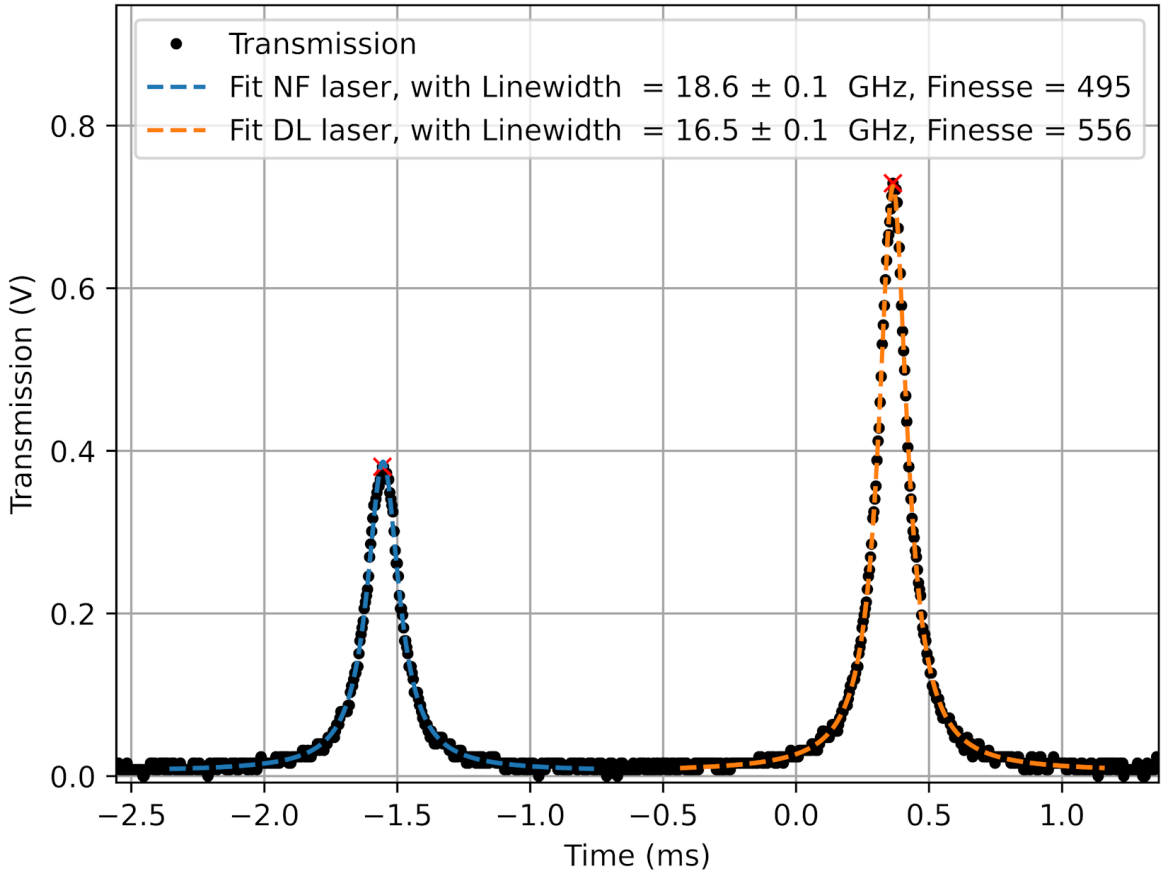

Figure 4.5: Photodiode signal of a fundamental mode when both the NF laser and DL laser are coupled to the cavity fibre. For this plot the length of the cavity is scanned by applying an AC signal to the fine piezo. Where $f = 2.9$ kHz, $V_{offset} = 0.16$ V $\rightarrow L_{cav} = 16.3\mu m$ and $V_{pp} = 2.2$ V. The linewidth is computed by using $\nu_{NF} = 470.49$ THz and $\nu_{DL} = 470.74$ THz. This measurement is taken at vacuum and at room temperature.

4.3. Microcavity Length Drifts at Room Temperature

A problematic feature at the beginning of this thesis are drifts in microcavity length. As has been stated at the beginning of this chapter, most measurements in this chapter are performed at atmospheric pressure and room temperature. To analyse the correlation between the temperature in the lab and the microcavity length, both parameters are monitored over a longer period of time. A temperature sensor is placed directly next to the microcavity and the supercontinuum laser is connected to the microcavity fibre. The length of the microcavity is monitored by taking a spectrum of the transmitted light by the cavity with the spectrometer (see Section 4.1). By taking a spectrum every minute, L_{cav} is measured over time. In Figure 4.6 (left top plot) the intensity plot of the spectrometer is shown over time. At the end of the measurement the fibre broke (around 00:00 the last day), which can be seen since no transmitted signal is measured after that. The measurement is performed over the weekend and lasts ~ 50 hours where every minute a spectrum is taken. An example of such a spectrum is also shown in Figure 4.6 (right top plot). From the spectrum, L_{cav} is computed for any given time during the measurement. The resulting microcavity length and the temperature at that time are shown in Figure 4.6 (left bottom plot), where a zoom-in on the first 12 hours is shown in Figure 4.7.

The first thing which can be noticed is that the peaks of the fundamental mode shift quite a lot over time. If the microcavity and the laser are perfect and stable, the fundamental modes will not move over time and would stay fixed at certain wavelengths. However, small variations in microcavity parameters (thermal expansion of the fibre material/mirror, expansion of the fibre holder or other components in the setup) can cause the peaks to shift. These changes result in a changing intensity plot.

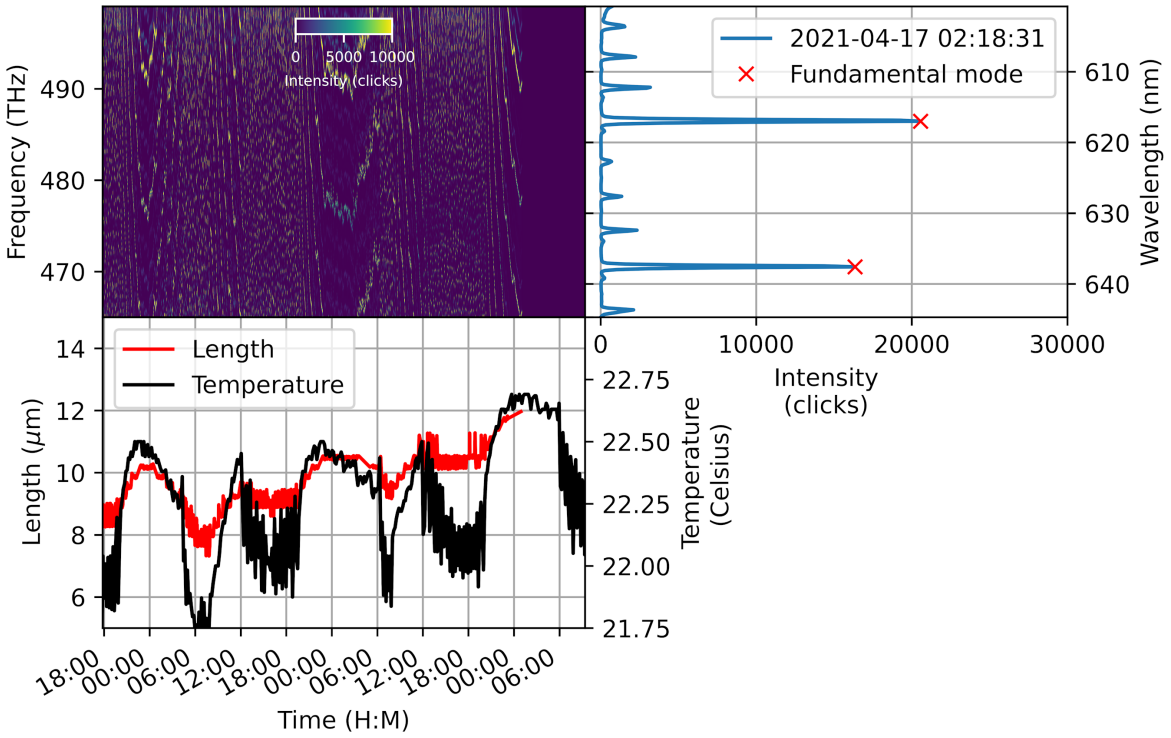

Figure 4.6: **(Top left)** Intensity plot of the transmitted signal taken every minute for 3 days in a row. The exposure time is $4000ms$ and the time between the spectra is $56s$ (1 minute in total). **(Top right)** A single spectrum taken at the second day at 02:18:31, where the fundamental modes are indicated with a red cross, the frequency difference between these peaks is used to compute the length of the microcavity. **(Bottom left)** Microcavity length and temperature during the measurement. The temperature is averaged every 10 minutes.

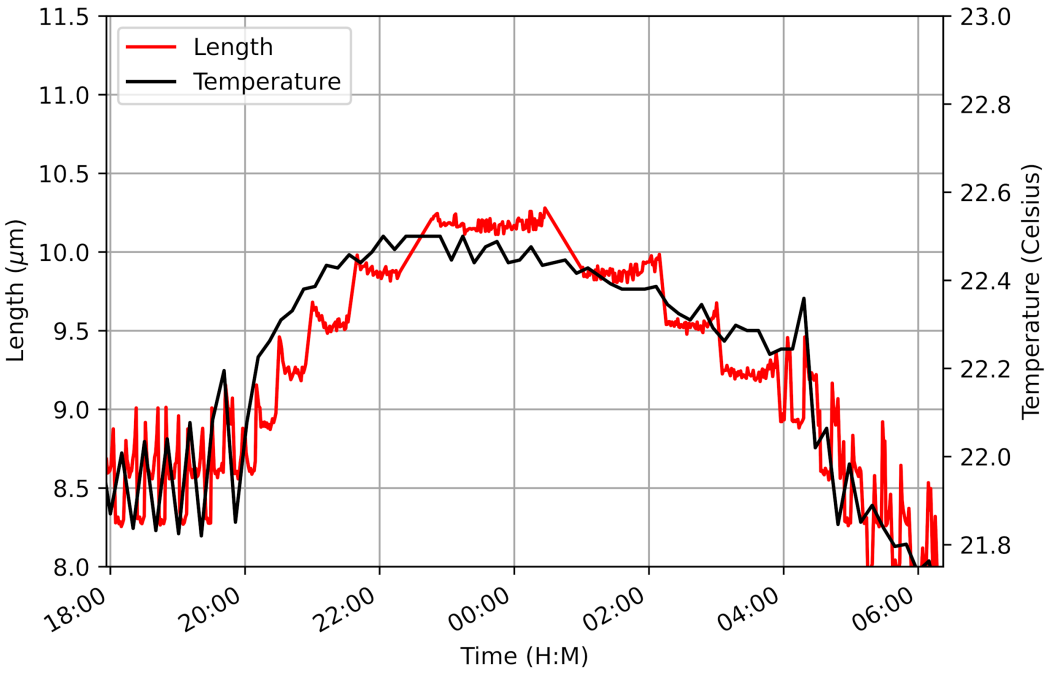

Figure 4.7: A zoom in of the first 12 hours of Figure 4.6. A jump in L_{cav} is caused by switching between different fundamental modes for the computation of L_{cav}.

However, the most important conclusion which can be drawn from Figures 4.6 and 4.7 is the relation between the temperature and the microcavity length. For a change in temperature of $\Delta T = 0.8℃$ the microcavity length changes with $\Delta L_{cav} = 4\mu m$. The length of the microcavity seems to follow the temperature almost $3\frac{1}{3} : 1$ ($3\frac{1}{3}$ μm per ℃). A very small drift in temperature can result in a relatively large change in microcavity length. This is important to notice, especially for longer time scales. If the setup is not used for some time, L_{cav} is not necessarily at the same length as the last measurement. This can be taken into account and monitored when going to cryogenic temperatures.

Another feature which is important to know is the change in finesse for different L_{cav}.

4.4. Length Dependent Microcavity Finesse

The Gaussian beam width in the microcavity increases for an increase in microcavity length (see Section 2.2.3). Thus the finesse will drop drastically when the beam width exceeds the ROC of the fibre dimple. This is because a lot of light will escape the microcavity and thus, the losses will increase (related to losses described at equation 2.9). These so-called clipping losses are the main source of losses for longer lengths and thus need to be investigated. A general expression for the finesse is given by:

$$\mathcal{F} = \frac{\nu_{FSR}}{\delta\nu}. \tag{4.2}$$

Where $\delta\nu$ is the linewidth of the fundamental mode and ν_{FSR} the Free Spectral Range frequency (difference in frequency between two subsequent fundamental modes). For this measurement, the length of the microcavity is determined, followed by measuring the linewidth at that length. With this method, the finesse is computed for different L_{cav}. After which the finesse as a function of L_{cav} can be fitted considering the following losses in the microcavity:

1. Designed mirror losses: $\mathcal{L}_{\mathcal{M}1}$ for the fibre mirror and $\mathcal{L}_{\mathcal{M}2}$ for the plane mirror
2. Clipping losses: $\mathcal{L}_{clip}$
3. Extra losses: $\mathcal{L}_{ex}$, these losses can originate from the presence of dirt, extra scattering losses etc.

By taking these losses into account, the finesse can be computed using:

$$\mathcal{F}_{cavity} = \frac{2\pi}{\mathcal{L}_{\mathcal{M}1} + \mathcal{L}_{\mathcal{M}2} + \mathcal{L}_{clip} + \mathcal{L}_{ex}}. \tag{4.3}$$

Where $\mathcal{L}_{\mathcal{M}1}$ and $\mathcal{L}_{\mathcal{M}2}$ are known,$\mathcal{L}_{ex}$ can be used as an extra fitting parameter and $\mathcal{L}_{clip}$ is defined as [23]:

$$\mathcal{L}_{clip} = e^{-2\left(\frac{D'_d/2}{w_m}\right)^2}. \tag{4.4}$$

Here D'_d is the effective dimple diameter, w_m the width of the Gaussian beam at the fibre (see Figure 2.6) and defined as (see equation 2.14):

$$w_m = w_0\sqrt{1 + \left(\frac{L_{cav}}{z_R}\right)}. \tag{4.5}$$

Where w_0 and z_R are defined in Section 2.2.3. From these equations can be deduced that the finesse has a dependence on the microcavity length through the clipping losses. The obtained finesse values as a function of L_{cav} are fitted using D'_d and $\mathcal{L}_{ex}$ as fitting parameters. The finesse as function of microcavity length together with a fit can be seen in Figure 4.8. For this measurement the linewidth is determined using the PEOM (see Section 4.2.1). As the NF laser was not yet included in the setup, measuring the linewidth for $\delta\nu > 6GHz$ increases the uncertainty in the linewidth. The uncertainty increases because the sidebands are not well separated from the main transmission peak and thus fitting 3 Lorentzian peaks is less accurate.

D'_d is chosen as a fitting parameter because, from the effective dimple diameter, an angle between the fibre and the plane mirror can be determined. Using the dimple diameter and ROC which are both

independently determined by an interferometric microscope after machining the fibre dimple (Appendix A). And using the effective dimple diameter, the angle between the fibre and the plane mirror can be found using simple geometry arguments [23]:

$$D'_d = D_d - \theta ROC. \tag{4.6}$$

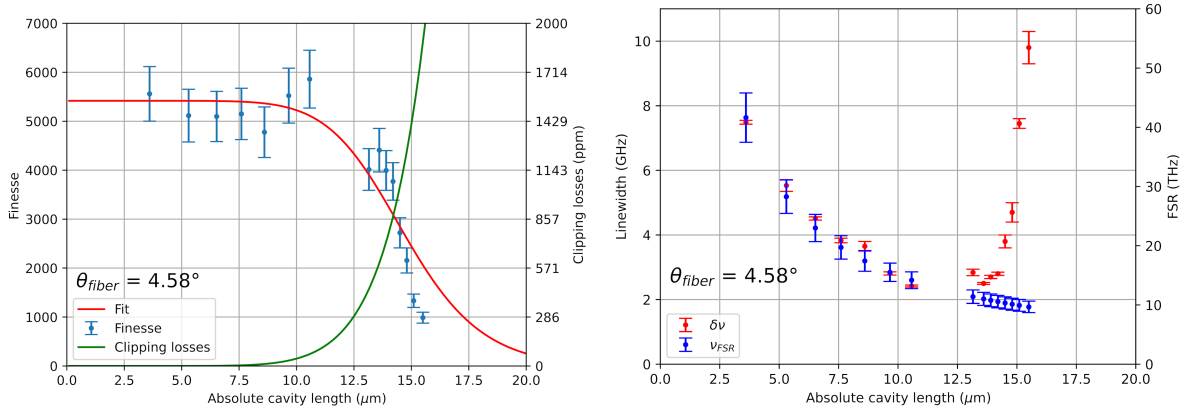

Figure 4.8: **(Left)** Finesse as function of L_{cav} with fit (in red) defined in equation 4.3 and clipping losses (in green). Here the losses for the mirrors are: $\mathcal{L}_{\mathcal{M}1} = 50ppm$, $\mathcal{L}_{\mathcal{M}2} = 400ppm$ which should, in perfect microcavity, result in a finesse of 14000. The highest obtained finesse is around 6000 which results in a quality factor of around 80.000 for $L_{cav} = 5\mu m$. The extra losses obtained from the fit are: $\mathcal{L}_{ex} = 710 \pm 54ppm$ and the found angle between the fibre and the plane mirror is $4.58°$. **(Right)** Microcavity Free Spectral Range ν_{FSR} and linewidth $\delta\nu$, in blue and red respectively for different microcavity lengths.

The clipping losses start to be the most dominant source of losses when the microcavity length is longer than $\sim 10\mu m$ since the finesse decreases rapidly after that length. The error in the finesse is due to an error in the microcavity length (which is taken at 10% of the microcavity length) and an error in the linewidth (which results from a fitting error). The fit in Figure 4.8 gives $\mathcal{L}_{ex} = 710 \pm 54ppm$ and an angle between the plane mirror and the fibre mirror of $4.58°$. This is an expected angle as other measurements indicated that the fibre touches the mirror at a length of $\sim 3\mu m$ (which converts to an angle close to the fitted angle). The extra losses are quite high compared to the losses of the mirror and restrict this microcavity to a finesse of ~ 6000. The obtained finesse results in a quality factor of around 80.000 and a mode volume (of the bare cavity) of $27\lambda^3$ for $L_{cav} = 5\mu m$ (see Section 2.3 equation 2.37). Looking at the fibre tip with a USB microscope gave the impression that there could be some small dirt particles on the fibre tip which could result in these extra losses. In Figure 4.8 it is quite clear that the finesse drops when the linewidth increases. At the finesse plateau (~ 6000), ν_{FSR} and $\delta\nu$ scale the same, when the clipping losses start to increase the linewidth of the microcavity start to increase as expected.

4.5. Summary

In this chapter, the method for characterising the microcavity properties is explained. Where two measurement methods for determining the microcavity length and two methods for determining the linewidth of a microcavity mode are discussed. With these characterisations, a ROC of the fibre dimple is found with ROC = $20.14 \pm 0.28\mu m$. The found ROC is in good agreement with an earlier analysis performed by TNO. Furthermore, a microcavity length dependence on the temperature in the lab is found. With a change in microcavity length of $3\frac{1}{3}\mu m$ per $°C$. By measuring the finesse of the microcavity modes at different microcavity lengths an angle of the fibre with respect to the plane mirror is found. The found angle is $\theta = 4.58°$. From the finesse measurements a maximum obtained finesse is around 6000 for an empty microcavity, which results in a quality factor of around 80.000 and a mode volume of $27\lambda_0^3$ for $L_{cav} = 5\mu m$.

5

Characterisation of Microcavity Length Vibrations

One of the main challenges of generating Purcell enhancement of the ZPL of NV centres using an open Fabry-Pérot microcavity is the stability of L_{cav}. The microcavity must be tuned on resonance with the NV^- and must stay on resonance. The Purcell factor (see Section 2.3), will increase for smaller mode volumes and will thus increase for shorter microcavity lengths. At shorter microcavity lengths, the finesse of the cavity mode will be high, thus very sensitive to length fluctuations of the microcavity ($\Delta L_{cav} = \frac{\lambda}{2\mathcal{F}}$, see Chapter 1). Therefore, it is important to know the size of the vibrations, and the frequency of the vibrations in order to work towards Purcell enhancement. This section will characterise the vibrations present in the new microcavity setup. First, the method of measuring the vibrations will be introduced in Section 5.1. Second, the results of the vibration measurements for different configurations of the microcavity will be discussed in Section 5.2. Then, in Section 5.3, the vibrations measurements are shown, where the cryocooler is on at room temperature. Finally, in Section 5.4 a summary of the results is given. All measurements in this chapter are performed with the HILA cryostat being installed. Meaning that: the microcavity setup is installed on the HILA cryostat baseplate inside the vacuum chamber and pumped to vacuum ($10^{-6} mbar$). Furthermore, the cryocooler can be turned on at room temperature.

5.1. Method for Measuring Vibrations

The vibrations affecting the microcavity can be measured by observing fluctuations in L_{cav}. Measuring microcavity length fluctuations with the methods described in Section 4.1 will hardly give representative and accurate results. The vibrations present in the system (after two passive vibration isolators) will be in the order of 10's of picometres and can have varying frequencies between $1Hz$ and a few kHz. The vibrations influencing the microcavity can be measured using the intensity of the transmission signal. As has been shown in Chapter 4, the light transmitted by the microcavity has a Lorentzian shape when it is on resonance with the input laser. This gives a direct correlation between the transmitted light and the microcavity length, as a small change in microcavity length will correspond to a different location on the Lorentzian. If all the parameters of the Lorentzian microcavity mode are known ($\delta\nu, L_{cav}$, peak height and voltage offset), a change in voltage of the photodiode can be converted to a change in L_{cav}.

Hence, to measure the vibrations, the microcavity mode first needs to be characterised. L_{cav} is measured with the white light source and $\delta\nu$ is measured using both the NF laser and the DL laser (see Subsection 4.2.2). From the linewidth measurement, the maximum transmission voltage on the PD is also obtained. After the microcavity mode is fully characterised, either the NF or DL laser is used and L_{cav} is tuned on resonance with the characterised fundamental mode (by applying a voltage to the coarse piezo). When the characterised fundamental mode is found, the PD signal is connected to the Yokogawa DLM5000 Series Mixed Signal Oscilloscope. The Yokogawa scope is used because long measurement traces (up to an hour) with high time resolution (125 Mpoints) can be recorded. The PD used for this measurement has a maximum bandwidth of 50 MHz (Thorlabs APD130A/M) and the time resolution of the oscilloscope is set to $1.6\mu s \rightarrow 625kHz$. Using this oscilloscope and PD, the vibrations

which can be measured are limited to $625kHz$. This bandwidth is high enough to capture all expected mechanical vibrations.

The PD signal is recorded for 20 s. During the 20 seconds, the PD signal must stay on one side of the Lorentzian and should thus not jump over the maximum transmission peak. If the vibrations cause the PD signal to move from the left side of the Lorentzian to the right side of the Lorentzian (or vice versa), the measurement is not reliable. Because, the effective length change is twice the length change compared to the situation where the PD signal moves from one side of the Lorentzian to the peak voltage and back to the same side of the Lorentzian. Therefore, the vibration measurements can best be performed at longer lengths, where the clipping losses dominate. For these lengths, the linewidth is very broad and larger fluctuations in L_{cav} can be tolerated to keep the transmission signal on one side of the Lorentzian. The results shown in this section are performed with the cryocooler off, the JPE stage floating on two out of the three axes and the HILA platform is floating and actively levelled.

In Figure 5.1 (left figure) a small portion of the 20-second trace can be seen. In the middle of Figure 5.1, the characterised fundamental Lorentzian mode is plotted, where the average, minimum and maximum voltage of the entire 20-second trace are indicated with a red dot and red lines respectively. Using this Lorentzian the changes in voltages on the PD can be converted to a change in frequency on the Lorentzian, and thus to a change in L_{cav}. The computed length detuning trace (in GHz and pm) can be found on the right in Figure 5.1.

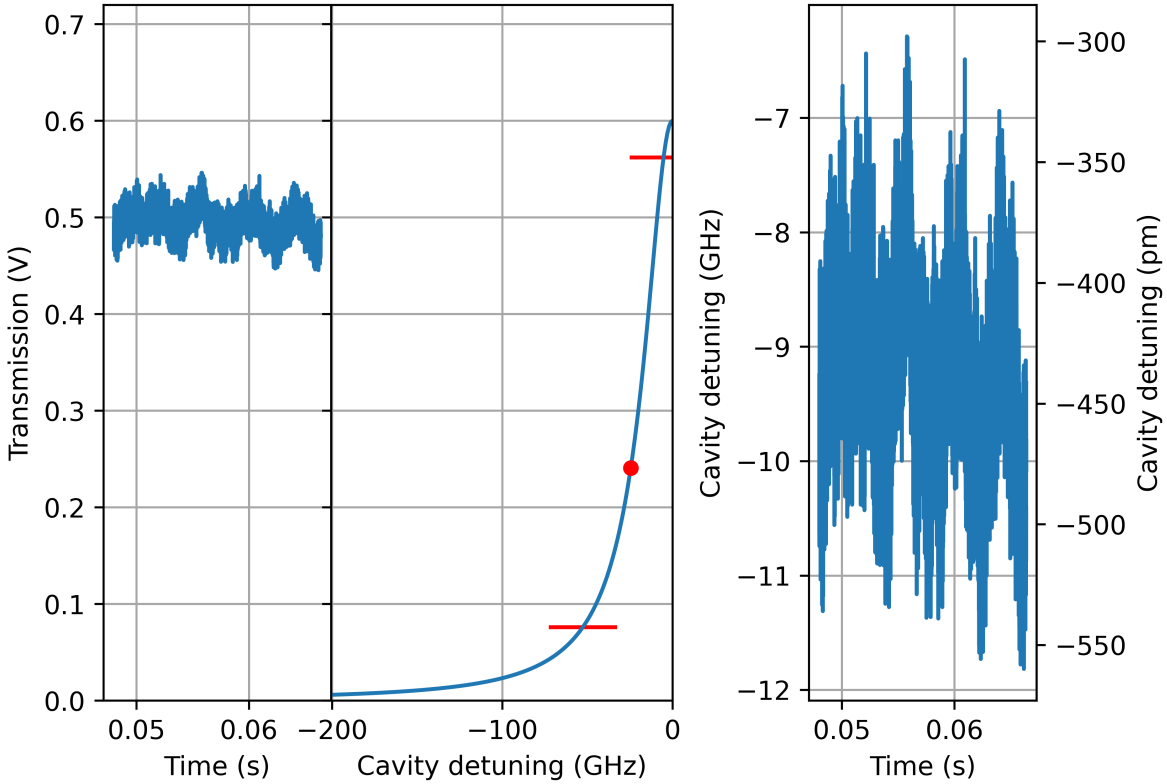

Figure 5.1: **(Left)** Example of 0.02 seconds of the 20 second PD transmission signal from a vibration measurement. **(Middle)** The Lorentzian which is generated after characterising the fundamental mode. Here the red dot indicates the average of the entire 20 second trace and the red lines indicate the maximum and minimum of the complete trace. For this measurement the microcavity properties are: $\delta\nu = 40.1GHz$, $L_{cav} = 22.3\mu m$ and $V_{peak} = 0.6V$. **(Right)** The voltage trace from the left figure which is converted to a detuning in microcavity length (in frequency and length). The measurement is performed by using the DL laser.

A general problem, which can be seen in the left and middle figures, is microcavity length drifts. The change in voltage in the left figure is smaller than the complete voltage range of the entire trace. Figure 5.2 (top figure) shows the microcavity length detuning during the complete measurement. What

can be seen, is that there is a drift in length detuning. The microcavity length detuning is detrended by applying a smoothing function on the length detuning signal and subsequentially removing the smooth time-trace from the dataset. The data can be detrended because the drift is not necessarily related to vibrations.

The resulting length detuning over time can also be seen in Figure 5.2 (middle figure). Where the cavity detuning is now centred around 0 and the resulting changes in length are a result of vibrations. An important node that has to be made here is that a change in voltage on the photodiode does not directly correspond to a detuning in L_{cav}. High fluctuations in laser power and detector noise can also change the measured PD signal. The changes in voltage related to these ”noise sources” will also contribute to the RMS vibration level in the analysis. More on the noise contribution to the RMS vibration level can be found in Section 6.3.

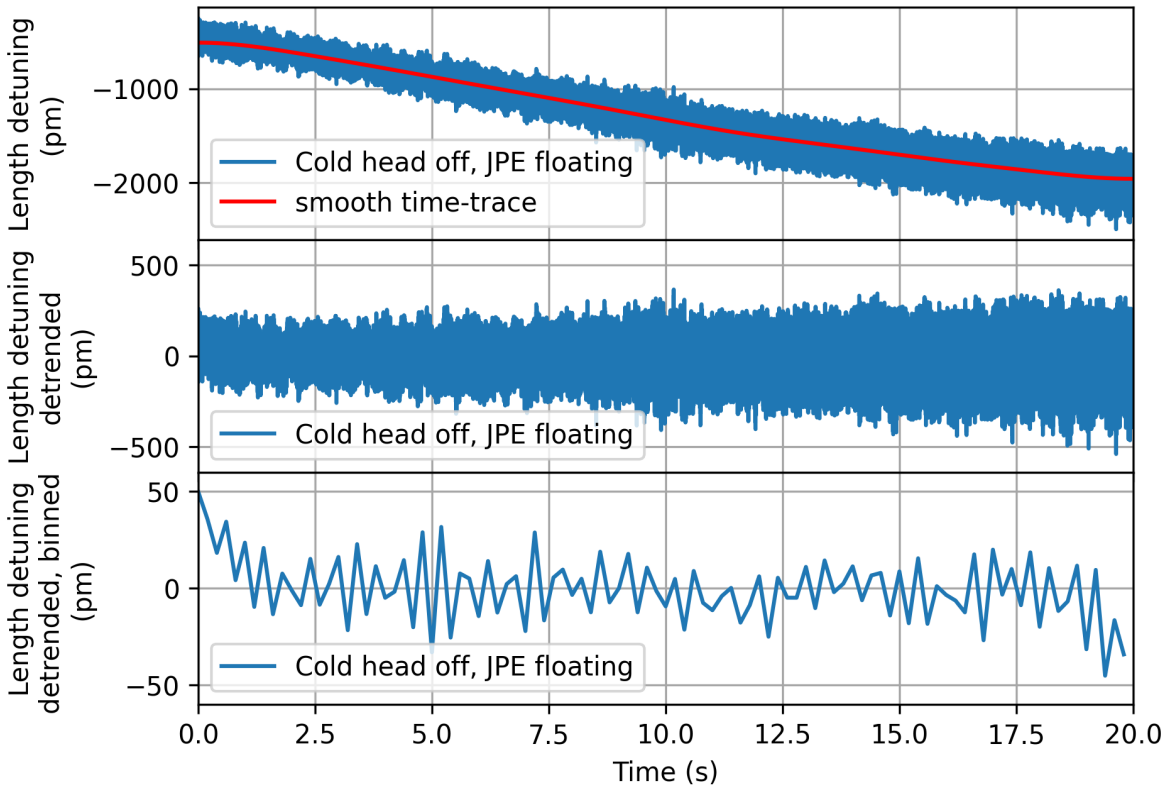

Figure 5.2: **(Top)** Computed length detuning of the microcavity over 20 seconds. The length detuning is detrended by applying a smoothening function on the detuning signal and removing this smoothening function from the data. The red line indicates the smoothening function over time. **(Middle)** The resulting detrended length detuning over time. **(Bottom)** The same detrended length detuning over time, only the data is binned in bins of 100 data points. The data displayed in these figures originates from the same measurement as Figures 5.1. This measurement is taken at vacuum and at room temperature, where the cold head is off. The JPE stage is floating on at least two axes. Meaning that the vibration isolator is not fully floating and thus does not function according to the design.

The next step in measuring the vibrations is to take the Fast Fourier Transform (FFT) of the length detuning signal. The FFT will give a spectrum from which the main vibration frequencies can be extracted. An example of the FFT and the cumulative sum of the FFT is shown in Figure 5.3. Using these graphs, the vibrations influencing the microcavity length can be identified. The focus of this section is to describe the vibration measurement method, not to analyse the results of the vibrations. The analysis of multiple vibration measurements will be discussed in Section 5.2.

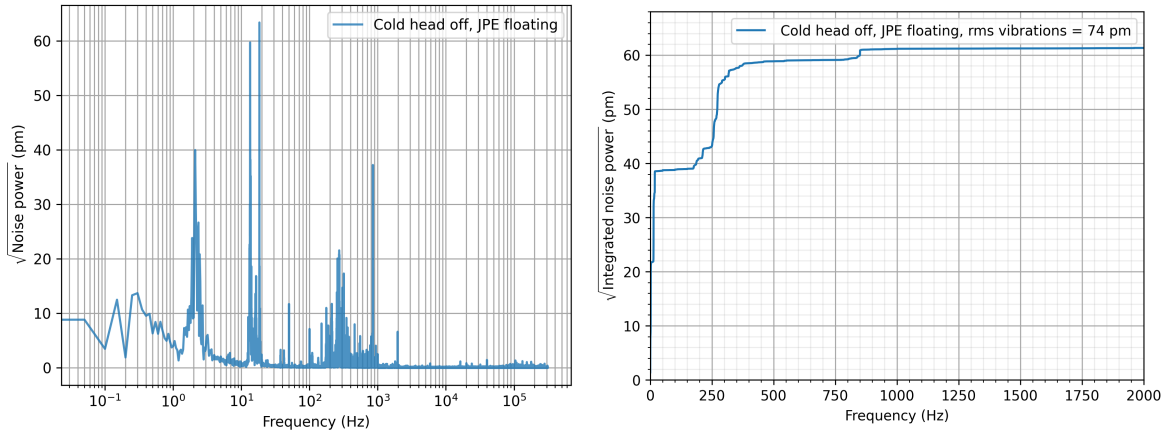

Figure 5.3: **(Left)** Typical FFT of the detrended detuning signal shown in Figure 5.2. Multiple frequency bands contribute to a detuning in L_{cav}. The most important frequencies of the vibrations are discussed in Section 5.2. **(Right)** The cumulative sum of the FFT shown in the left figure. The rms vibrations are computed using the entire microcavity detuning signal displayed in Figure 5.2. The rms values indicates a maximum of vibration sizes, as noise sources (see text) also contribute to the rms vibration level.

5.2. Different Configurations of the Microcavity

With the new microcavity setup, multiple parameters can be changed which influence the vibration level. Using these parameters, the setup can be tuned such that the vibration level is as low as possible. The best configuration (so far) is discussed in more detail. The results shown in this section are all performed at vacuum and at room temperature with the cryocooler off. A separate section is dedicated to the difference in vibration level when the cryocooler is switched on (see Section 5.3).

5.2.1. Influence of the Nanopositioner Control System

The first vibration measurements result in a very high vibration level, independent of the performance of the JPE passive vibration isolator. This resulted in further analysis of the frequency of the vibrations which contribute to the high vibration level. The FFT and the cumulative sum of the FFT of the vibration measurement with an unexpected high level of vibrations can be seen in Figure 5.4. The frequencies of the vibrations which are measured are almost all at multiples of $50Hz$. Indicating that there is some electrical component inducing these vibrations [42]. Multiple different configurations are tested to find the main source of these "$50Hz$" contributions. By grounding the input of the JPE x,y and z positioner control the vibrations at multiples of $50Hz$ are significantly reduced (see Figure 5.4). Even with all these positioners grounded, there still seem to be contributions of $50Hz$ vibrations. The still remaining $50Hz$ contributions arise most likely due to the connection to the coarse piezo or the fine piezo. Especially using an amplifier to enlarge the movement of the coarse piezo, also enlarges the contributions of the $50Hz$ vibrations. Therefore, the amplifier for the coarse piezo is removed and the JPE positioners are grounded (during the measurements). The final solution to shield the microcavity from these electric AC induced vibrations, is to filter the input signal to all the positioners/piezo's in the setup.

Another important aspect of the vibration characterisation shown in Figure 5.4, is located at other specific frequency ranges. The following frequency ranges which are related to a (relatively) high level of vibrations are investigated further:

- $1 - 3Hz$ (DC)
- $10 - 20Hz$
- $250 - 400Hz$
- $750 - 900Hz$.

To counteract the vibrations at these frequencies, it is important to know how they are transmitted to the microcavity. Starting with analysing the frequency range: $750 - 900Hz$. These vibrations are related to the resonance frequency of the JPE positioner system. The main argument for attributing

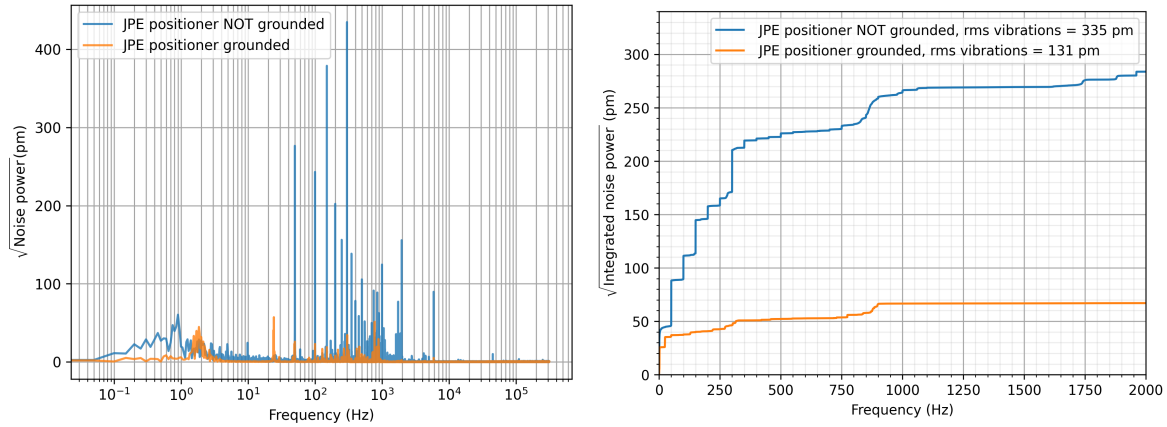

Figure 5.4: **(Left)** FFT of the computed microcavity length detuning for a measurement where all the JPE positioners are grounded or not grounded. Showing clear peaks in vibration size for vibrations with a frequency of $m \cdot 50Hz$, with m being an integer when the positioners are not grounded. The two measurements are taken on two different days where the JPE passive vibration isolator is in a non floating position (see text).This can result in different vibration sizes and different vibration frequencies. **(Right)** Cumulative sum of the FFT in the left figure. A clear difference in vibration level is visible due to the $m \cdot 50Hz$ vibrations.

these vibrations to the resonance frequency of the positioner system is twofold. First of all, a high pitch arises when applying an AC signal to the coarse piezo at this frequency. Secondly, it has been measured with a transfer function measurement and an acceleration measurement. More on the transfer function measurement can be found in Appendix B and more on the acceleration measurement can be found in Appendix C. These measurements also confirm mechanical simulations performed by the manufacturer. Since the vibrations are on resonance with the JPE positioner system, the detuning in L_{cav} is large. From the same transfer function measurements, an explanation for the vibrations with $f \approx 250 - 400Hz$ arises. This would also indicate that the vibrations at this frequency are excited due to a resonance of the JPE positioner system. This particular resonance is very close to a multiple of $50Hz$ which is also a problem in the transfer function measurement. Furthermore, at these frequencies, lots of possible excitation sources can be found. A few explanations are ruled out by measuring the influence of that particular parameter. For example, by measuring the vibration level with the green laser, laser fluctuations are ruled out. And by measuring the transfer function of the fine piezo, the feedback of the fine piezo is also ruled out. A definite explanation for this vibration frequency is still to be determined. For example, by measuring the vibrations when the JPE passive vibration isolator is removed and the positioner and microcavity are directly placed on the HILA baseplate. This will give more insight into the origin and transmission of these vibrations.

An explanation for the $10 - 20Hz$ vibrations is not so straightforward and is most likely related to the passive vibration isolator. These vibrations will be discussed more in Section 5.2.2. The last large vibration contributions are near DC. These vibrations can originate from large (solid) pieces in the setup like the active levelling of the HILA baseplate. However, the high level of vibrations can also be due to the cut-off frequency of the JPE passive vibration isolator. The vibration isolator should function as a low pass filter for vibrations where the cut-off frequency is originally designed to be below $1Hz$. At this cut-off frequency, the vibration isolators stopband starts rising, and thus vibrations at this frequency are less suppressed. Due to wrong material simulations in the design of the vibration isolator, the cut-off frequency is higher than initially intended. Therefore, the vibrations at DC are most likely to arise from the cut-off frequency of the JPE passive vibration isolator. Since these vibrations are almost at DC, actively counteracting these vibrations should be relatively simple. Furthermore, vibrations at these frequency levels have less influence on the final goal, Purcell enhancement. As the measurements and pulses are generated at frequencies orders of magnitude higher.

The vibrations which are measured at higher frequencies (above the cut-off frequency), should be suppressed by the JPE passive vibration isolator and the floating HILA baseplate, since both of them function as a low pass filter for vibrations. The presence of these higher frequency vibrations thus indicates that either of the two systems is not functioning properly. As the JPE passive vibration

isolator shows clear signs of malfunction (the entire stage cannot float with the current mass), the stage is investigated in more detail by measuring the vibrations for different conditions.

5.2.2. Different Floating Conditions for the JPE Passive Vibration Isolator

The performance of the JPE passive vibration isolator stage shows some problems. The stage is designed to float, and when it does the vibrations should be suppressed. However, multiples problems occur when getting the entire JPE stage (and thus the microcavity) to float.

- The total mass mounted on top of the JPE positioner system is too high. Almost all extra masses have been minimized (replacing copper with aluminium and reducing the size of thermal straps connections). However, with the bare minimum of mass currently in the system, the passive vibration isolator does not seem to put the JPE positioner stack to its floating condition. Multiple efforts could not fix this problem. So during this thesis, the JPE passive vibration isolator is never fully functioning according to design. This causes the general level of vibrations to be higher than expected and operation generally harder. The JPE motors (see Section 3.2.1) can still vary the floating condition of the positioner stack, by rotating the motors of the JPE modules (Figure 3.3).

- The wire connecting the PCB to the nanopositioner in the Z-direction touches the JPE baseplate. Due to this wire, the passive vibration isolator is bypassed and thus a higher level of vibrations is to be expected. Where different frequencies of vibrations can be transmitted to the microcavity.

In Figure 5.5 the measured vibrations for multiple positions of the JPE motors are displayed. Where the increase in positions corresponds to a more elevated cylinder on which the microcavity is mounted (see Figure 3.1). By analysing the positions of the JPE motors at vacuum, a rough estimation can be made from which positions the cylinder is going towards its floating condition. In this case, position 3 should already push two JPE modules in its floating condition. And from positions 6 and 7, the end stops of all the motors from the JPE modules are reached.

Looking at Figure 5.5, a few important characteristics can be found:

1. The $800Hz$ resonance can be significantly reduced. This frequency of vibrations is on resonance with the resonance frequency of the JPE positioner stack. By moving the passive vibration isolator towards its floating condition the vibrations at this frequency are significantly reduced. This would indicate that the passive vibration isolator is suppressing vibrations at this frequency.

2. By moving the JPE stage to its floating condition, vibrations with frequency $\sim 230-300Hz$ appear to be transmitted more. From position 4 and higher, an increase of the vibration level is very well visible at frequencies $\sim 250-300Hz$ compared to the non-floating conditions of positions 1 and 2. This frequency of vibrations is not expected to arise from a resonance frequency of the JPE positioner stack (from simulations performed by JPE). An explanation of these vibrations could be related to the passive vibration isolator. Since the JPE passive vibration isolator is not functioning according to the original design, a very complex transmission of vibrations can arise. This can dramatically influence the size of the vibrations but also the frequency of the vibrations being transmitted.

3. The $14Hz$ frequency vibrations seem to be suppressed more when the JPE stage is moving towards its floating condition. For some configurations, the $14Hz$ peak is not even present. This gives a strong indication that the transmission of these vibrations to the microcavity is highly dependent on the floating condition of the JPE stage. However, it can also be related to the wire (from the coarse piezo) touching the HILA baseplate. As the JPE stage is put into different floating conditions, the wire can also change its position (and connection to the baseplate).

4. The level of vibrations increases once the JPE module motors reach their end stop. Especially the $1-2Hz$ vibrations seem to increase. From these measurements, it is still hard to attribute these low-frequency vibrations to the JPE module. There is not a clear correlation between the floating condition and the low DC frequencies. However, intuitively it is very likely that when the end stops of the JPE modules are reached, the level of vibrations increase as this is not an ideal condition for the JPE modules. This can also be seen in the sharp increase of frequencies at $270Hz$ when the end stops are reached.

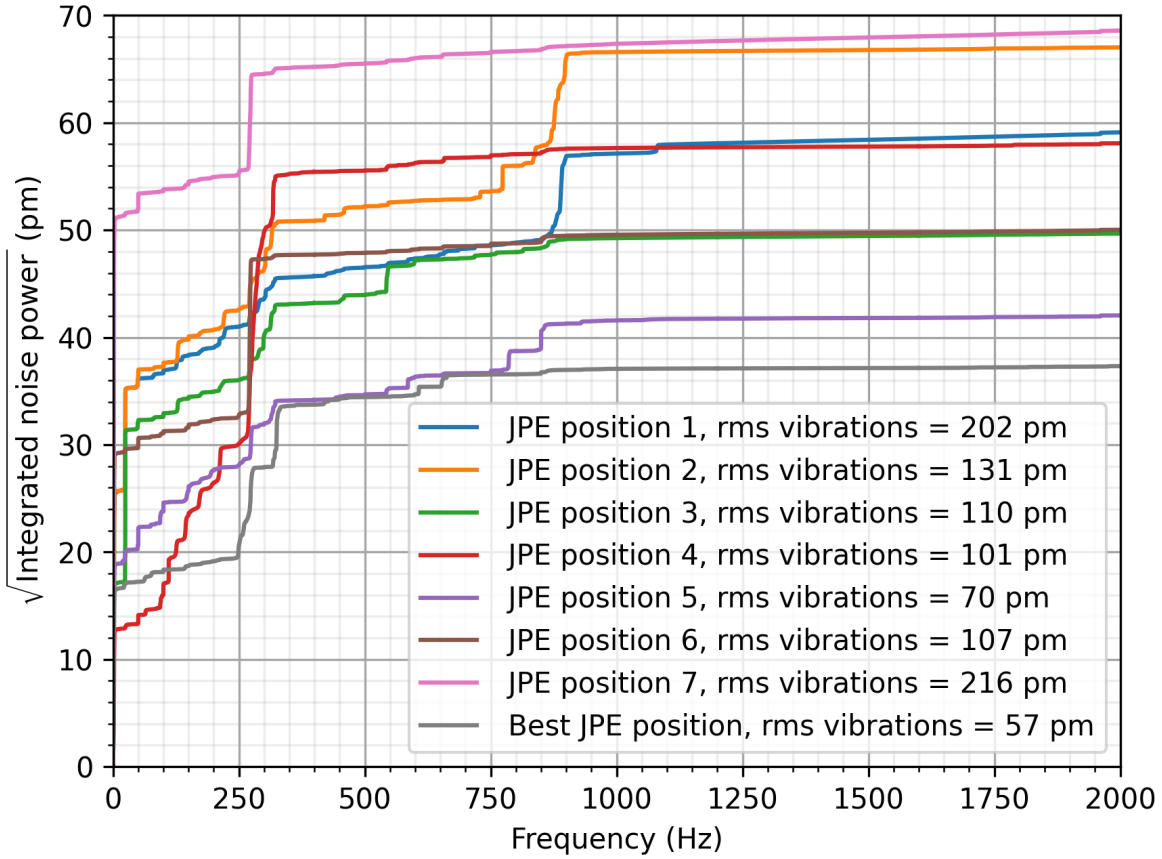

Figure 5.5: Cumulative sum of the FFT of the length detuning signal (shown in the Appendix D Figure D.1). Position 1 indicates the reference point for the other positions. For positions 1 and 2 it is known that the JPE passive vibration isolator is in the NON-floating condition. From position 3 to position 5 the vibration isolator is moving towards the floating condition. For positions 6 and 7, the JPE module motors are reaching their end stop. The measurements of positions 1-7 are all performed with the same vacuum conditions (10^{-6}). Furthermore, the wire connecting the PCB to the coarse piezo is touching the baseplate in all of these measurements. For the best JPE position, the wire is not touching and the best floating condition is found by looking at each JPE passive vibration isolator module (when the vacuum chamber is open). For the best floating condition one axis of the passive vibration isolator is still not fully floating.

These measurements are all performed without being able to assess the actual floating condition of the passive vibration isolator. The actual floating condition can only be assessed when the setup is not at vacuum and the vacuum chamber is open. When opening the vacuum chamber after the measurements, a few remarks could be made.

- The JPE stage is not in its most ideal floating condition for either of the measurement positions.
- The bars connecting the JPE passive vibration isolator modules to the JPE positioner stack are bend. More specifically, several leaf springs in these bars are bend. More on this can be found in Appendix E Figure E.1.
- The wire connecting the nanopositioner in the Z-direction to the JPE is touching the baseplate and could thus transport vibrations to the JPE positioner stack (and the microcavity).

Two of these problems could be solved directly. The wire is detached from the baseplate and an optimal floating condition for the passive vibration isolator stage is found. In this optimal condition, one of the JPE modules is still not able to float and thus, still not completely able to move freely. A vibration measurement (at vacuum and room temperature) of this best configuration is also shown in Figure 5.5. The best configuration also has the lowest vibration level so far but still shows some

characteristic vibration frequencies which have been encountered before. Especially the $250 - 300Hz$ vibrations are the main source of vibrations, together with the DC vibrations. Taking all measurements into consideration, the main conclusion which can be drawn is that the actual performance of the JPE passive vibration isolator is highly dependent on the floating condition. Furthermore, the vibration level is still high, also at frequencies that are supposed to be suppressed by the two low pass filters for vibrations. This high level of vibrations, and the not ideal performance of passive vibration isolators, also shows to be a problem when the vibrations are measured when the cryocooler is switched on.

5.3. With and Without Cryocooler

The final condition in which Purcell enhancement is to be realised is at cryogenic temperature. At cryogenic temperature, the cryocooler continuously runs to ensure cooling at the sample site. The pumping of the cryostat will induce large vibrations which can be problematic for detuning of L_{cav}. Measuring the vibrations when the cryocooler is on, will give a more realistic final level of vibrations. The cryocooler can be manually turned on for several minutes to measure the vibrations, but to stay at room temperature. A general problem which is expected when performing the measurement, is that the vibrations might be so high, that the induced length detuning causes the transmission signal to move from one side of the Lorentzian to the other side of the Lorentzian. If this happens (the PD signal reaches the maximum transmission voltage), the RMS vibration level should be considered as the minimum vibration level.

The resulting vibration levels with the cryocooler on and off are shown in Figure 5.6. What can immediately be noticed is the high level of vibrations in general. The noise floor of vibrations for the measurement where the cryocooler is on, is already higher than some vibrations with specific frequencies when the cold head is off. The RMS vibration level shown in Figure 5.6 with the cryocooler on, is also the minimum vibration level (due to the PD signal overshooting the maximum transmission). In Figure 5.7, the voltage trace on the PD signal is shown for the measurement with the cryocooler on. As is clearly visible, the vibrations induced by the cryocooler are so large that the PD signal moves over the peak of the Lorentzian. This makes the measurement and its results not reliable.

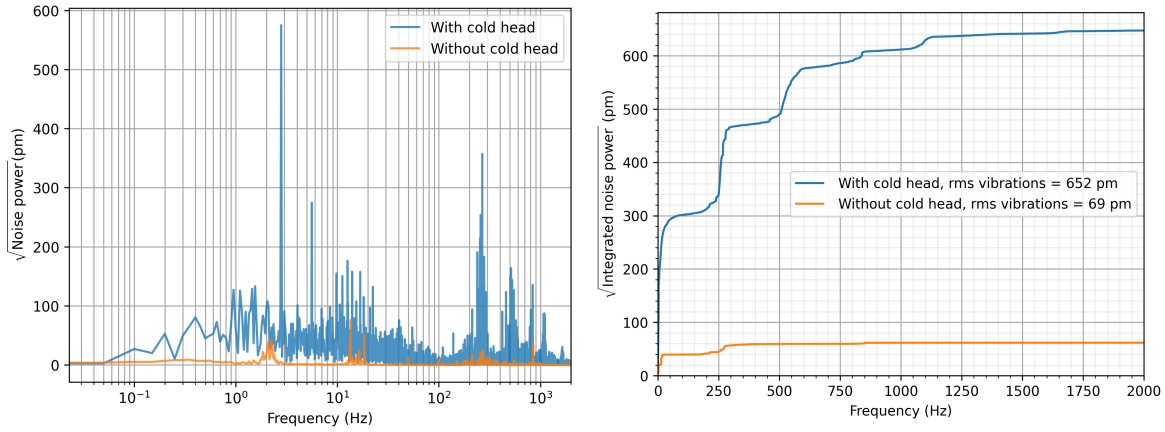

Figure 5.6: **(Left)** FFT of the detuning in L_{cav} for a measurement where the cryocooler is on and off. A clear increase in general vibration level is visible for the measurement with the cryocooler on. **(Right)** The cumulative sum of the FFT signal. Especially the not suppressed vibrations when the cryocooler is not on are significantly increased when the cryocooler is on.

From these vibration measurements can be deduced that still most of the vibrations have a familiar frequency. Especially the vibrations with frequencies at DC, around $10-20Hz$ and (maybe) at (multiples of) $\sim 250Hz$. These frequencies are already not well suppressed when the cryocooler is off and become even more problematic when the cryocooler is on. A promising sign which can be seen in Figure 5.6 is that when a resonance frequency is already somewhat suppressed ($\sim 800Hz$) the cryocooler makes it not significantly worse. If the vibrations at the known frequencies are suppressed more by improving the passive vibration systems, the vibration level with the cryocooler on might be significantly reduced. However, this is still speculation and also needs to be measured.

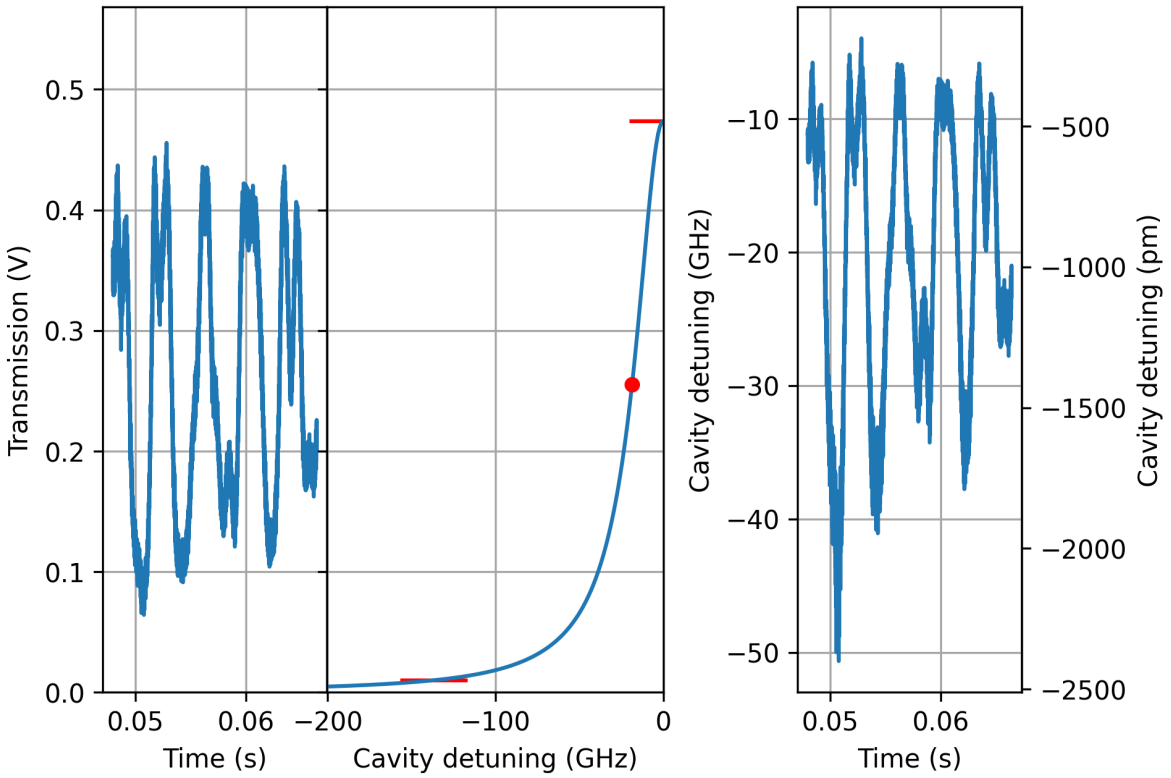

Figure 5.7: **(Left)** 0.02 seconds of the 20-second PD transmission signal when the cryocooler is on. **(Middle)** The Lorentzian which is generated after characterising the fundamental mode. The transmission signal of the left figure is the same microcavity mode. Here the red dot indicates the average of the entire 20-second trace and the red lines indicate the maximum and minimum of the complete trace. The maximum reached voltage is equal to the maximum of the Lorentzian peak, indicating that the vibrations are so high that they cause a detuning in L_{cav} to move over the entire peak. Here, $L_{cav} = 22.3\mu m$ and $\delta\nu = 40.1GHz$ **(Right)** The voltage trace from the left figure which is converted to a detuning in cavity length (in frequency and length). The measurement is performed by using the DL laser.

For now, it seems that the level of vibrations is too high. This needs to be solved in order to move towards Purcell enhancement for colour centres in diamond. The most obvious next step is to improve the passive vibration isolation of the JPE passive vibration isolator and some other minor improvements (see Chapter 7). However, the vibrations which cause a detuning in L_{cav} can also be actively counteracted. How to actively stabilise L_{cav} is discussed in detail in Chapter 6.

5.4. Summary

In this chapter, the vibrations influencing the microcavity length are measured. The size and frequencies of these vibrations are measured by tracking the intensity of the transmitted light with a photodiode. The change in PD signal can be converted to a detuning in microcavity length. The first vibration measurements show a large influence of vibrations at multiples of $50Hz$. Indicating that an electronic signal is actively driving these vibrations. By switching of an amplifier and disconnecting the JPE positioners control unit, most of the $50Hz$ vibrations are suppressed. To completely remove these induced vibrations, the electrical input signal needs to be filtered before applying it to the piezo's. Another large influence on the size and frequency of the vibrations is the performance of the JPE passive vibration isolator. Changing the floating condition of the JPE stage dramatically influences the transmission of vibrations with frequencies in the range of $1-3Hz$, $10-20Hz$, $250-300Hz$ and $750-900Hz$. Improving the passive vibration performance is required to also measure the vibrations when the cryocooler is on. Currently, the vibrations inducing a detuning in microcavity length are too high to measure when the cryocooler is on.

6

Active Microcavity Length Stabilisation

To obtain a stable microcavity length, large vibrations need to be suppressed. With the design of the High Inertia Low Acceleration (HILA) cryostat and the passive vibration isolator from Janssen Precision Engineering (JPE) vibrations at frequencies $>\sim 10Hz$ should be suppressed. Since both systems act as a low pass filter for vibrations in all three spatial dimensions. If the microcavity length detuning induced by vibrations, is small enough that the microcavity is always on resonance with the input laser, the transmission signal is always somewhere on the transmitted Lorentzian ($\Delta L < \frac{\lambda}{2\mathcal{F}}$) (see Section 5.1). Then, the light transmitted/reflected by the microcavity can be used to actively stabilise the microcavity length. Since the passive vibration is still not optimal, active feedback on the microcavity length can ensure a more stable microcavity length. In this chapter, the method for actively stabilising the microcavity length will be discussed in Section 6.1. Followed by Section 6.2 where the drifts in microcavity length (also discussed in Section 4.3 and Section 5.1) are actively compensated. Then, in Section 6.3 the final stability of the microcavity is shown when the microcavity length is "locked" to a fundamental mode. Finally, Section 6.4 gives a summary of the results obtained in this chapter.

As Chapter 5 has shown, the performance of the passive vibration isolation is not optimal and the size of the vibrations is still too high when the cryocooler is on. Therefore, this chapter only actively stabilises the microcavity length when the cryocooler is off. If the passive vibration isolation performance is improved, the same method described in this chapter can be used to actively stabilise the microcavity length when the cryocooler is on. All measurements shown in this chapter are performed at vacuum ($10^{-6}mbar$) and at room temperature.

6.1. Method for Actively Locking the Microcavity Length

As the introduction of this chapter states, a signal from the microcavity is required to stabilise L_{cav}. A simple feedback loop is constructed which uses the transmission signal of the microcavity. The feedback loop for active stabilisation is shown in Figure 6.1. The feedback loop is very similar to the loop used to measure the transfer function (See Figure B.1). The microcavity is put to a resonance length of the DLC/NF laser (with the coarse piezo) and is scanned over the resonance length by applying an AC signal to the fine piezo. This will give a Lorentzian transmission signal as explained in 4.2. The applied AC signal is then mixed with the Photodiode (PD) signal and the resulting "mixed" signal is low pass filtered. After the low-pass filter, a DC error signal is obtained. This DC error signal is used to feedback a voltage to either the coarse piezo or to the fine piezo. The feedback voltage is generated by applying a Proportional-Integral-Derivative (PID) controller on the error signal [43]. Due to a Bias T, an AC signal from a Lock-In amplifier (HF2LI 50 MHz Lock-in Amplifier Zurich Instruments) can be combined with a DC signal from the PID loop. How the error signal is generated and how it can be used to actively stabilise the microcavity length will be discussed in Section 6.1.1. More details about the PID loop can be found in Section 6.1.2. Why the feedback signal from the PID loop is used for both the coarse piezo and the fine piezo will be explained in Section 6.2.

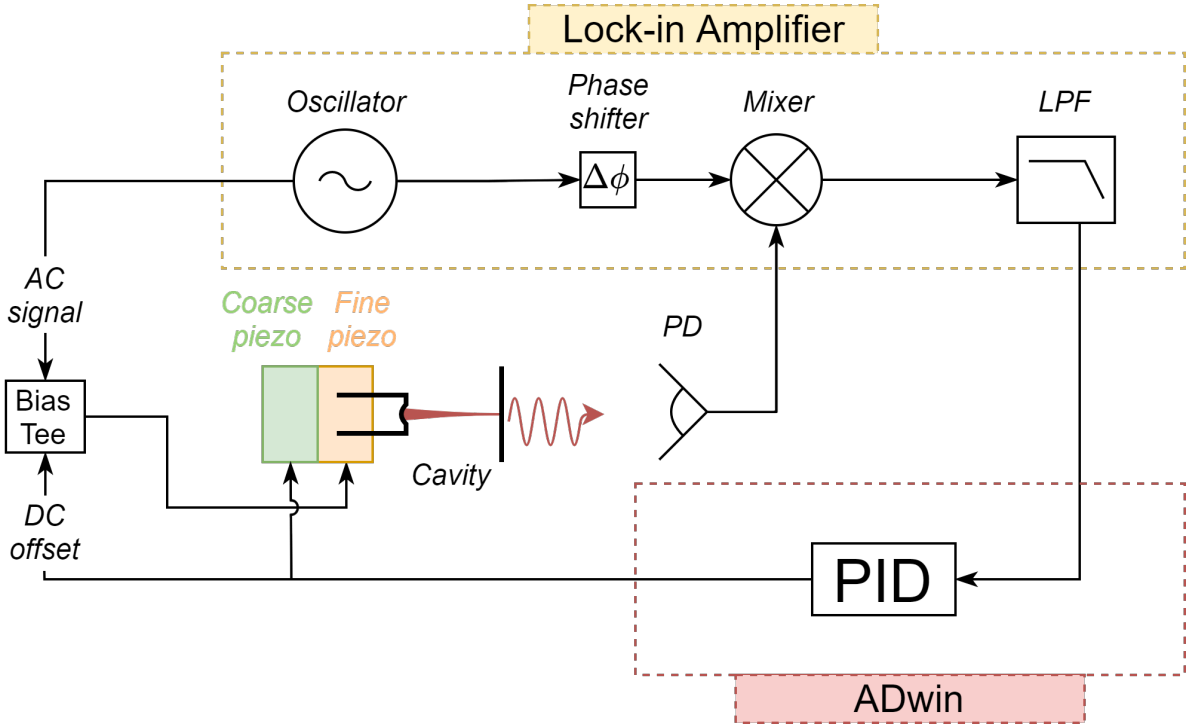

Figure 6.1: Schematic overview of the electronics for active stabilisation. The oscillator, phase shifter, signal mixer and low-pass filter (LPF) are all internally connected in the Lock-In amplifier. The AC output from the Lock-In amplifier is combined with the DC feedback from the PID loop (see Section 6.1.2). The output of the Bias Tee is connected to the fine piezo to stabilise L_{cav}. The feedback signal of the PID loop can also be applied to the coarse piezo to counteract slower length drifts (see Section 6.2). The transmission signal from the microcavity is used in the Lock-In amplifier to generate an error signal (see Section 6.1.1). The PID loop is programmed in an integrated micro-controller (ADwin-Pro II).

6.1.1. Error Signal

To enable active feedback on L_{cav} information is needed about the change in L_{cav}. By applying an AC signal to the fine piezo a Lorentzian transmission peak will be generated somewhere in time in a period of the AC signal. Ideally, the Lorentzian peak is situated at half the period of the applied AC signal (at the steepest slope of the sine/cosine wave). Because the transmission is then exactly symmetric with respect to the AC signal, thus the microcavity is exactly on resonance with the laser. To automatically determine if the transmission peak is located at the middle of the AC signal, the PD signal and the AC signal need to be mixed. By mixing the AC signal and the PD signal and low pass filtering this mixed signal only the difference in signal between the AC signal and PD signal remains. This so-called ”error signal” has a phase and an amplitude [44]. The phase gives information with respect to the relative location of the transmission peak compared to the centre of the AC signal (left or right of the centre). Whereas the amplitude of the error signal includes information of how ”far” the transmission peak is located from the centre. By combining the phase and the amplitude of the error signal an exact location of the transmission peak compared to the AC signal is found. Using this error signal a feedback voltage can be applied to either the coarse piezo or the fine piezo in order to locate the transmission peak to the centre of the AC signal. In Figure 6.2 an example of automatically locating the Lorentzian peak to the centre of the AC signal can be seen. Here the increase in opacity indicates the evolvement of the Lorentzian in time and the feedback voltage after the PID loop is applied to the coarse piezo. It is clearly visible that the error signal (red) moves towards 0 when time increases. The Lorentzian should be exactly centred when the error signal is 0, as the amplitude of the error signal is then 0. Using this method the entire Lorentzian is locked to the centre of the AC signal. However, in this method, the microcavity length is scanned continuously which does not have any practical applications, except measuring the linewidth more conveniently. The upside of obtaining the error signal in this fashion is that it also works when the AC signal has an extremely small amplitude. If the amplitude of the AC signal is very small a very small detuning in microcavity length is introduced. This results in a change

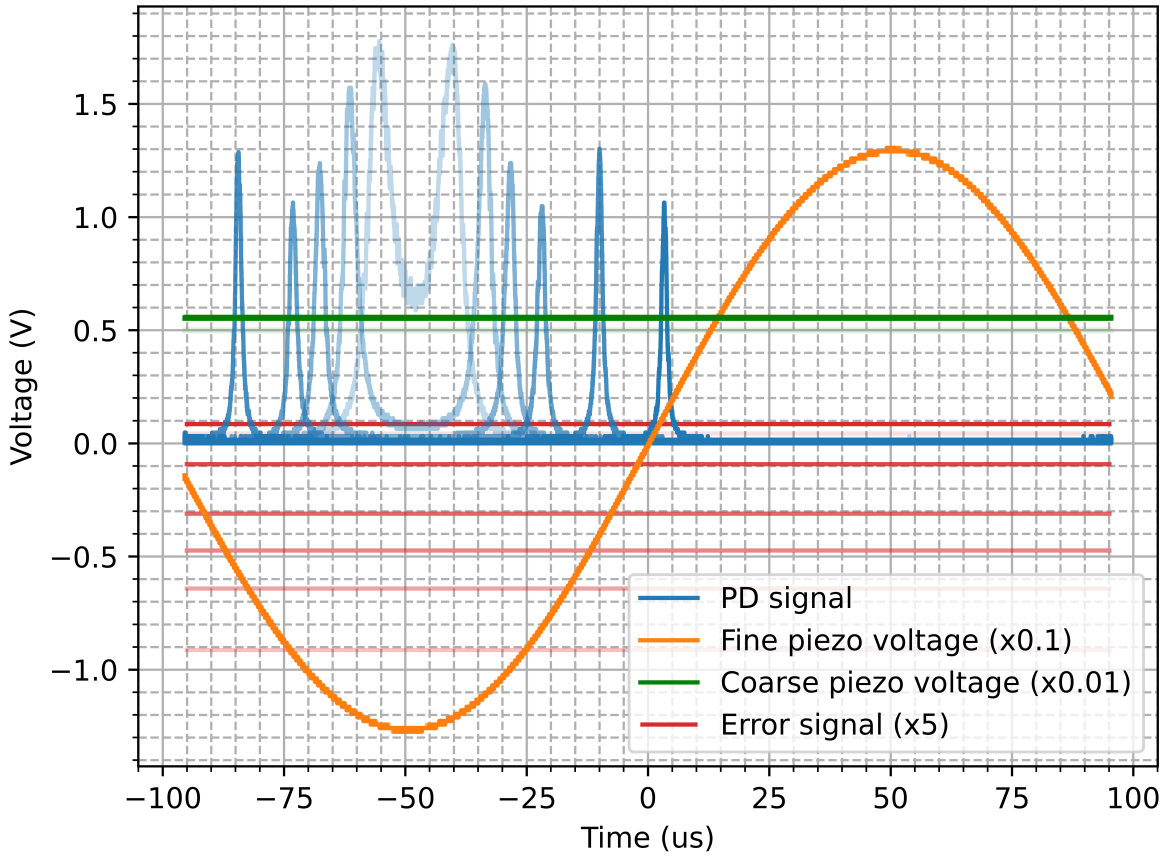

Figure 6.2: Principle of the active stabilisation of the microcavity length. The microcavity length is scanned over the resonance condition using the fine piezo (orange), where the Lorentzian transmission peak is centred at the AC signal of the fine piezo. An increase in opacity indicates an increase in time at which the PD voltage, error signal voltage and coarse piezo voltage are recorded. Thus showing the convergence of the error signal towards 0. The AC signal applied to the fine piezo is constant for all time frames and has: $f = 5kHz$, $V_{pp} = 25V$. The voltage applied to the coarse piezo varies (from $50V$ to $56V$) to lock the Lorentzian to the centre of the AC signal. For the lock the following PI parameters are used $P_{gain} = 0.001$ and the Integration term is left out ($I_{time} = \infty$), see Section 6.1.2

of transmission intensity since the detuning would move the transmission intensity over the Lorentzian. This change in the PD signal can again be used to find an error signal. The error signal will go to 0 when the transmission of the microcavity is at its maximum. With this method, a tiny detuning in microcavity length is induced (order of a few pm) to stabilise the microcavity. Ideally, the microcavity length is stabilised when the microcavity length is not detuned. A different scheme that produces an error signal by detuning the input laser (and not the microcavity length) can also be used to stabilise L_{cav}. This active stabilisation scheme is called the Pound-Drever-Hall lock and is discussed in more detail in Appendix F [45, 46]. For now, this technique for active stabilisation is a trade-off between the induced vibrations from the AC signal and the length stabilisation which is achieved.

6.1.2. PID Loop

Using the generated error signal, an automatic feedback circuit needs to ensure that the error signal is converted to an appropriate change in voltage. This voltage can then be applied to either the coarse or fine piezo. A PID loop is one of the simplest feedback loops which can solve the conversion between the error signal and feedback voltage. In this thesis, only the Proportional part and the Integral part of the controller are used (essentially a PI controller). The PI controller converts the error signal to a

feedback signal using the following formula:

$$V_{applied} = P_{gain} \cdot V_{error} + \frac{1}{I_{time}} \cdot V_{error}. \tag{6.1}$$

Where P_{gain} and I_{time} are variables that need to be tuned to an ideal combination and V_{error} is the error signal from Section 6.1.1. Tuning the PI parameters is a time-consuming process and is done according to the method described in [43]. If either P_{gain} or I_{time} is too high, the PI controller is constantly overshooting the desired error signal (underdamped). If P_{gain} and I_{time} are too small, the PI controller is not sensitive enough (overdamped). To obtain the best possible feedback of the PI controller P_{gain} and I_{time} need to be chosen such that the system is critically damped. The PI controller has a certain feedback frequency which can also be adjusted and also influences P_{gain} and I_{time}. The PI controller is programmed in an integrated micro-controller (ADwin-Pro II). More complex feedback loops can also be implemented to obtain better stability. H_∞ methods can synthesize controllers to achieve stabilization with a guaranteed performance [47]. These kinds of controllers require more knowledge about control theory and are not in the scope of this thesis. Furthermore, the implementation of a more sophisticated feedback process does not ensure better performance. Using this active stabilisation with the PI controller, the microcavity can be locked to a certain transmission peak of a (fundamental) mode. More about the actual stability of the microcavity length when the lock is actively stabilising L_{cav} can be found in Section 6.3. Apart from a more stable microcavity length, the lock can also counteract microcavity length drifts (mentioned at room temperature in Section 4.3 and Section 5.1). The microcavity length drift compensation is discussed in more detail in Section 6.2.

6.2. Compensation of Length Drifts

As both Section 4.3 and Section 5.1 show, is that tiny changes in the setup (temperature, pressure etc.) can cause the microcavity length to drift. This happens at a relatively low frequency and can thus be counteracted with a slow feedback loop. It is wise to divide the active length stabilisation into a slow part (drifts) which will be compensated with the coarse piezo due to its larger travel range and a fast part (vibrations) which will be counteracted with the fine piezo due to the high feedback bandwidth.

To further automate locking to a fundamental mode, the resonance condition of the microcavity has to be found first. Next, the microcavity length must be locked to the fundamental mode. This process is automated and separated into 2 sections. First, the so-called ”fundamental mode sweeping” procedure is initiated, which entails:

1. Apply a starting voltage to the coarse piezo.
2. Denote the error signal for the applied voltage.
3. If the error signal exceeds a set threshold (reaches a fundamental mode) the coarse piezo voltage is maintained and the ”Fundamental mode locking” procedure is initiated.
4. If the error signal does not exceed the set threshold, the applied voltage is increased with an incremental voltage. And the process starts over.

Using this structure L_{cav} is swept until a fundamental mode is found. When the fundamental mode is found the so-called ”Fundamental mode locking” procedure is initiated:

1. Denote the error signal and convert the error signal to a feedback voltage for the fine piezo (see Section 6.1.2).
2. Repeat the PI loop to ensure a high level of stability of the microcavity length.
3. After $25s$, use the PI loop (at a different frequency than the PI loop for the fine piezo) to also apply a feedback voltage to the coarse piezo (more on this in the text below).
4. Use the coarse piezo to counteract the drifts and use the fine piezo to counteract vibrations.

How a feedback voltage is applied to the fine piezo is discussed in Section 6.1.2. A different loop is used to apply a voltage to the coarse piezo. In this loop, the most important input parameter is the fine piezo voltage over time. Ideally, the average voltage applied to the fine piezo would be 0 and it would

only change to counteract the vibrations. Therefore, the voltage applied to the fine piezo is recorded and summed up over time. If the sum of the fine piezo voltages is larger than 0, the voltage applied to the coarse piezo should increase. If the sum is negative, the voltage applied to the coarse piezo should decrease. Applying this sequence every so few seconds (dependent on the size of the drifts) the fine piezo voltage should go towards 0 and solely counteracts vibrations whereas the voltage applied to the coarse piezo changes slowly to compensate for the drift. To make sure that the coarse piezo is not constantly overshooting and influencing the fine piezo, the sum of the fine piezo voltage is set to 0 when the voltage applied to the fine piezo has a different sign than the sum of the voltage applied to the fine piezo.

The whole process of locking to a certain fundamental mode described above is summarized in Figure 6.3.

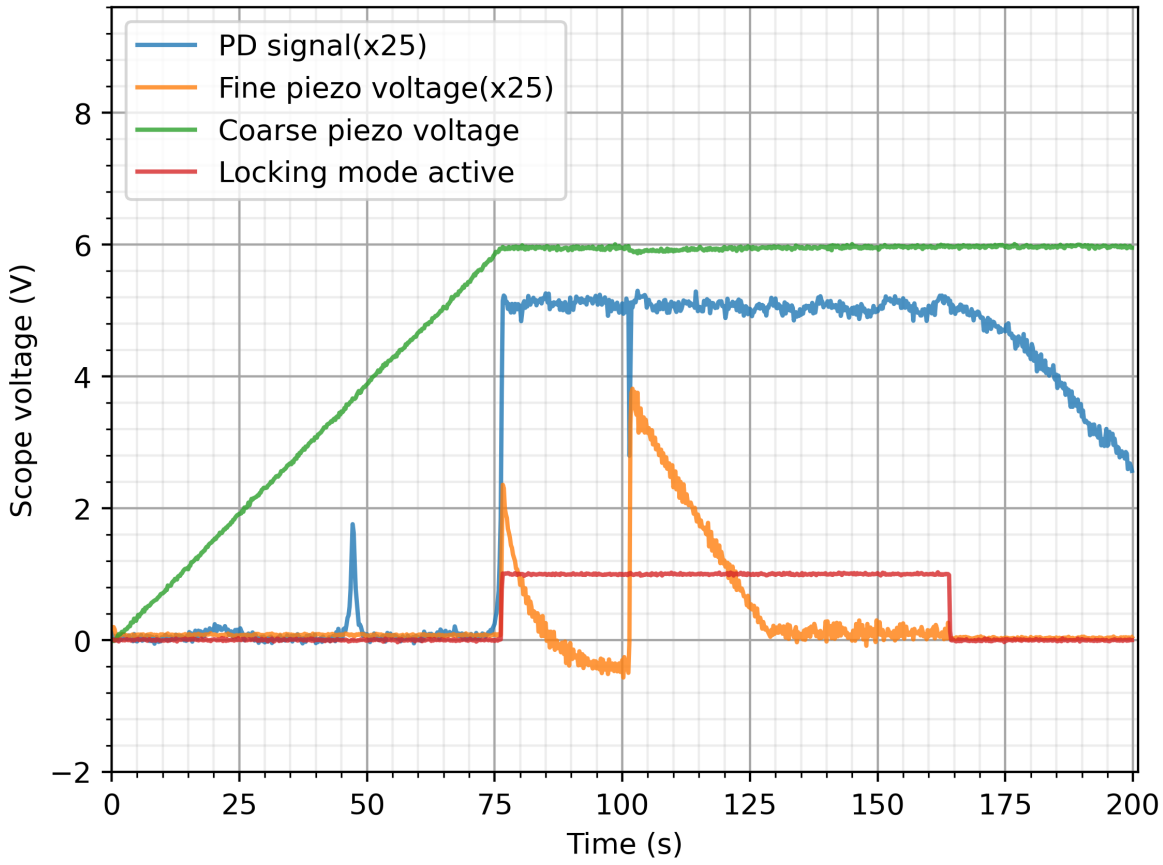

Figure 6.3: Process of actively stabilising the microcavity length. First the coarse piezo is sweeping its voltage until a fundamental mode is found. Then the fine piezo locks to the fundamental mode. After $25s$ the coarse piezo takes over drifts in length. The red line (Locking mode active) indicates if the "Fundamental mode locking" procedure is activated. The data shown in this plot is obtained with the Yokogawa scope and is binned for 1000 data points. This can explain some of the fluctuations in the PD signal. For this measurement the following parameters for the active stabilisation are used: $P_{gain} = 0.0006, I_{time} = 100.000$ and $f_{feedback} = 5kHz$. Here $f_{feedback}$ is the feedback frequency of the PI loop of the fine piezo. The PI loop for the coarse piezo has a $f = 1Hz$. The AC signal continuously applied to the fine piezo has $f = 30kHz$ and $V_{pp} = 2.5mV \sim 4pm$. Furthermore the properties of the microcavity are: $L_{cav} = 24.5\mu m$ and $\delta\nu = 52GHz$.

In this figure, certain aspects of the process described are clearly visible. In the first 75 seconds the voltage on the coarse piezo (and thus the microcavity length) is swept until it reaches the fundamental mode. During the sweep, multiple higher-order modes can also be seen in the PD signal. Once the fundamental mode is found, the locking mode is activated (red line moves to $1V$). This is directly visible by the constant coarse piezo voltage, the increase of voltage for the fine piezo and the constant PD signal. After 25 seconds the coarse piezo is taking account for the drifts. The settings of the PI loop

are deliberately chosen not to be perfect to illustrate the behaviour. The fine piezo has a voltage < 0, thus the coarse piezo voltage decreases (with a relatively large step). This can be seen in a spike of the fine piezo voltage and a dip in the PD signal. After the coarse piezo takes over the drifts, the fine piezo moves linearly down to $0V$ and only counteracts changes in L_{cav} at high frequency (vibrations). Whereas the coarse piezo slightly increase its voltage to counteract the drift. After 165 seconds, the lock is manually turned off to observe the drifts in the system. As is to be expected the PD signal gradually decreases due to microcavity length drifts.

Apart from the obvious benefit of compensating the cavity length drift, the slow drift compensation can also be used to perform linescans of the NV^- by resonant excitation measurements shown. By scanning the laser frequency different energy transitions can be addressed and detected (see [48, Figure 1c]). Since the NV^- states will only be excited (and thus emit photons) when the laser is precisely on resonance. Using the slow drift compensation, an input laser can be varied, while the microcavity stays on resonance with the laser. This is shown in Figure 6.4. The frequency of the NF laser is changed by applying a voltage to the laser while the "Fundamental mode locking" process is keeping track of the changing laser frequency. The frequency range of the NF laser is $\Delta f = 56GHz$ during the measurement ($> \delta\nu$). The coarse piezo voltage and the PD signal are recorded for each frequency of the laser. The coarse piezo changes accordingly for an increase in frequency and the PD signal fluctuates on a relatively small scale. These fluctuations are most likely related to the constantly changing laser frequency since the frequency change is larger than the linewidth of the microcavity.

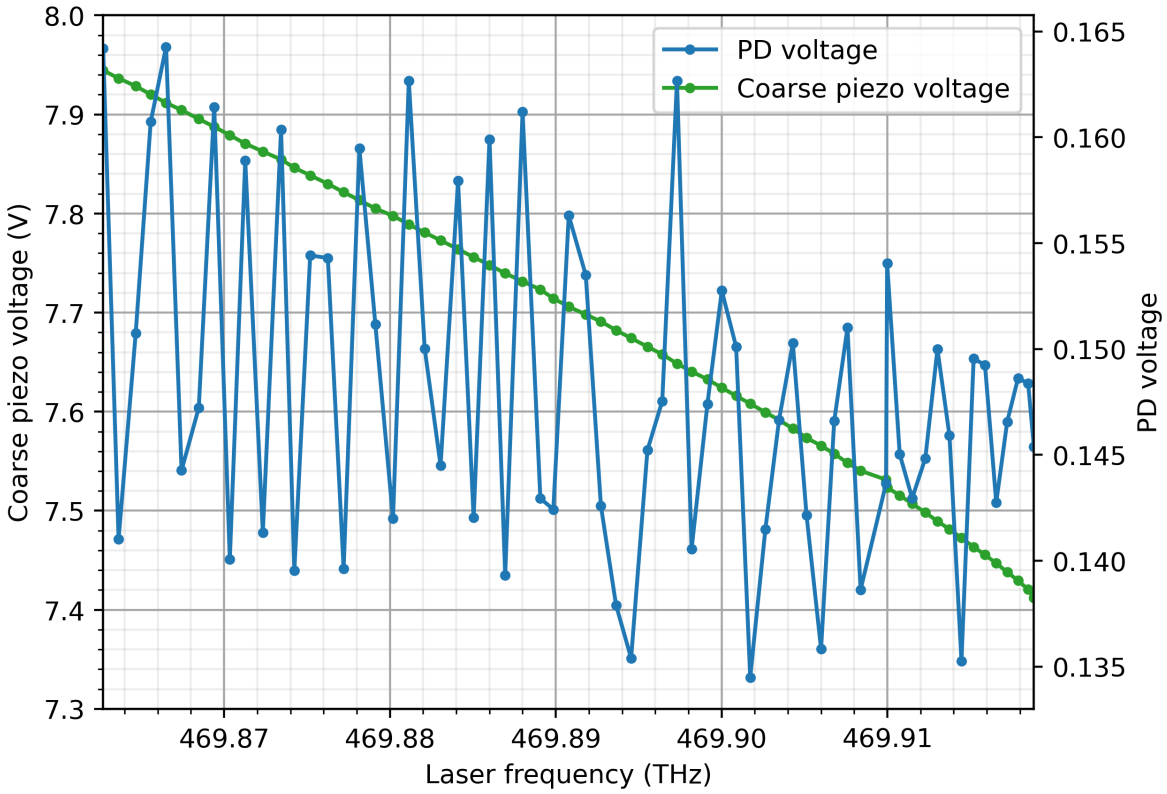

Figure 6.4: Performance of the drift compensation. By changing the frequency of the NF laser the coarse piezo voltage changes to stay on resonance with the current laser frequency. The PD signal is also recorded during the measurement to make sure that the lock is functioning properly. Changes in PD signal can arise from a not perfect lock, but are most likely to originate from a change in quality/power of the NF laser.

The drift compensation serves as a very practical tool, namely: keep the microcavity on resonance with the input laser. But it does not counteract the vibrations in the system. How much the vibrations can be counteracted with the fine piezo is described in the next section.

6.3. Lock Performance

The actual performance of the active feedback loop is highly dependent on the parameters of the PI loop and the size of the vibrations. By tuning P_{gain} and I_{time} to a combination where the feedback is critically damped, the microcavity length detuning will be compensated. In this section, an example of the active stabilisation of the microcavity is given, by first measuring vibrations when the microcavity is locked and then measuring the vibrations (on the same fundamental mode) when the lock is switched off. The exact same measurement method is used as described in Section 5.1. Only now it is important to notice that when the microcavity is locked to the maximum transmission, the transmission signal will continuously move from the left side of the Lorentzian to the right side of the Lorentzian. Therefore, the cavity detuning is multiplied by two when the microcavity is locked. This means that the RMS vibration level shown for the active feedback vibration measurement is the maximum vibration level. In Figure 6.5 the detuning signal from the vibration measurement for 20 seconds is displayed. Where the detuning signal needs to be detrended to only account for the actual vibrations in the system.

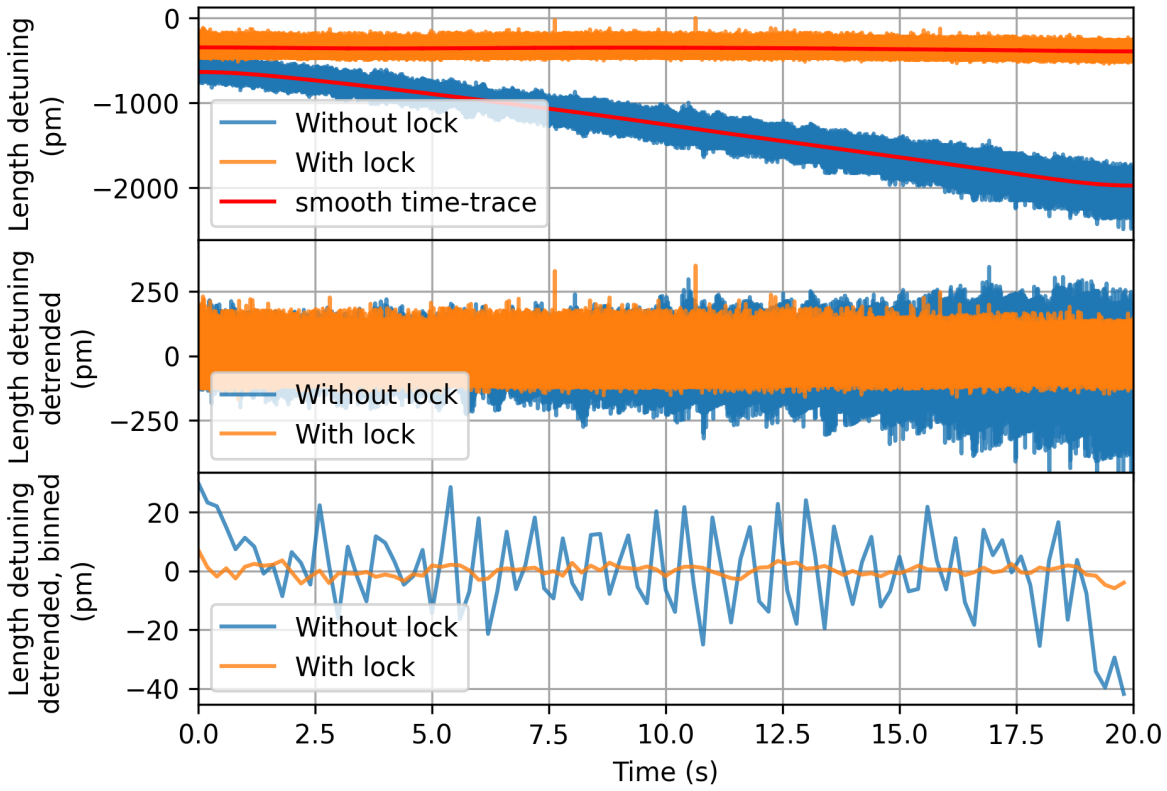

Figure 6.5: **(Top)** Cavity detuning with and without active length stabilisation. The red lines indicate a smooth time trace which is used to obtain a detrended microcavity length detuning signal displayed in the middle figure. **(Middle)** Detrended microcavity length detuning signal with and without active length stabilisation. **(Bottom)** Binned microcavity length detuning signal from the middle figure. The data is binned for every 100 data points. The measurement is taken at vacuum and at room temperature where the cryocooler is off. The JPE stage is in the best possible floating condition but still not floating on one axis.

In the top figure of Figure 6.5, it is clearly visible that the lock actively stabilises the microcavity length. If the lock is not used the microcavity drifts off resonance with the laser. In the bottom figure of Figure 6.5, a clear improvement during the lock can also be observed. The lock does not only counteract the microcavity length drifts but also counteracts vibrations at higher frequencies. The FFT and the cumulative sum of the FFT of the cavity detuning signal are shown in Figure 6.6. In the FFT signal, almost no frequency peaks associated with vibrations are visible once the microcavity is locked. A peak at $50Hz$ and $150Hz$ can be seen, these peaks are discussed and a solution to removing these vibrations are discussed in Section 5.2.1. Another small vibration peak can be seen at $2kHz$, which seems to be suppressed compared to the case where no active feedback is applied. Overall, the

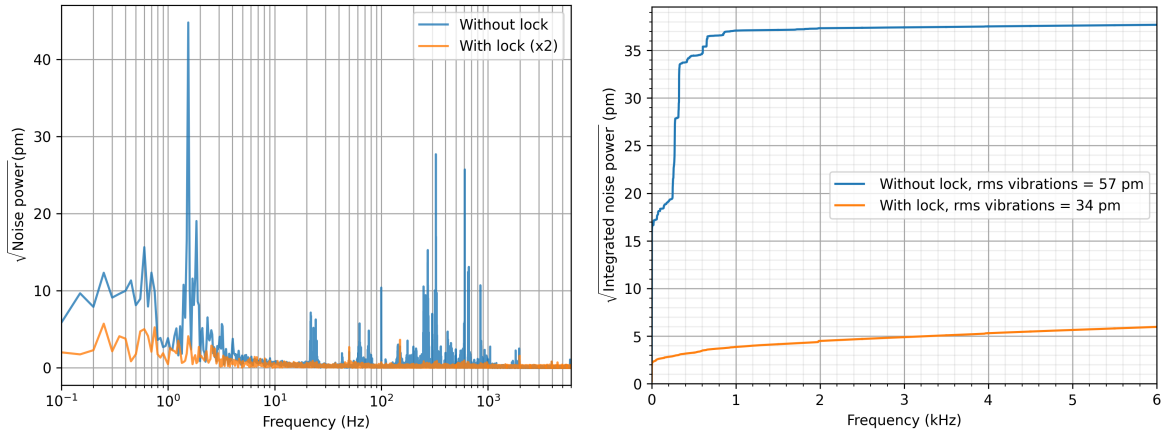

Figure 6.6: **(Left)** The FFT of the detrended detuning signals with and without active length stabilisation. Here the data from the measurement with active length stabilisation (With lock) is multiplied by two to indicate a more relevant size of vibration. Almost all vibrations are suppressed when the microcavity length is actively stabilised. **(Right)** The cumulative sum of the FFT shown in the left figure. The RMS vibrations are computed using the entire microcavity detuning signal displayed in Figure 6.5. The RMS values indicate a maximum of vibration sizes, as noise sources (see text) also contribute to the RMS vibration level. This is clearly visible in the ever increasing noise power.

lock seems to reduce the vibrations by a factor of two at minimum. And the vibration level seems to stay below $10pm$ when the lock is actively stabilising the microcavity length. The exact performance of the lock is hard to determine as the RMS vibration values are not to be trusted. There is a very simple explanation for the incorrect RMS vibration value. Looking at the cumulative sum of the FFT in Figure 6.6 when the lock is active, an ever increasing integrated noise power is visible. This increase arises due to noise sources already mentioned in Section 5.1, namely laser noise, detector noise etc. Due to these noise sources, a change in PD voltage is also converted to a cavity length detuning and contributes to the RMS vibration level. Normally this noise level is low compared to the actual vibrations in the system and can therefore be neglected. However, when the microcavity length is stabilised, the noise level is the main contributor to vibration level. This is also clearly visible in Figure 6.7.

Here the range of the PD signal is again highlighted in the middle figure. For the analysis where the lock is active, the peak of the Lorentzian is determined by the maximum PD voltage. However, the average PD signal is not located at the top of the Lorentzian, as one would expect when the lock is functioning ideally. It is very likely (also due to the symmetry of the maximum voltage and minimum voltage of the entire $20s$ trace) that fluctuations in laser power or detector noise are limiting the potential of the lock and the actual obtained RMS vibration level. There are some hints that the connection to the ADwin feedback some noise to the Yokogawa scope. For practical reasons, the noise is not a problem, as the lock seems to function even with a high noise level and reduces the level of vibrations by at least a factor of 2. It is important to mention that the active stabilisation of the microcavity length only functions when the cryocooler is off. Locking the microcavity length with the cryocooler on is still not possible due to the size of the vibrations. This should be improved when the performance of the passive vibrations is increased. Then, the active stabilisation method can also be applied to lock the microcavity length when the cryocooler is on. This will give a more realistic final picture of the stability of the microcavity length.

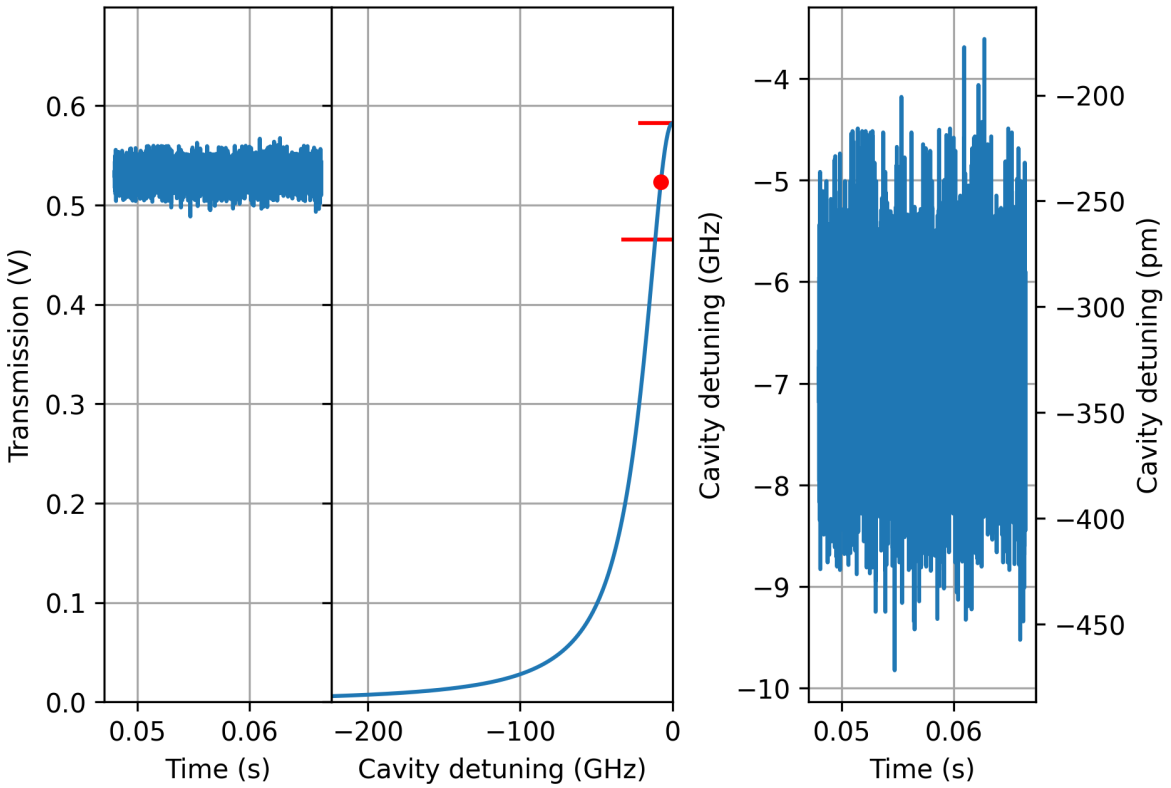

Figure 6.7: **(Left)** 0.02 seconds of the 20-second PD transmission signal when the microcavity length is actively stabilised. **(Middle)** The Lorentzian which is generated after characterising the fundamental mode. The transmission signal of the left figure is the same microcavity mode. Here the red dot indicates the average of the entire 20-second trace and the red lines indicate the maximum and minimum of the complete trace. For this measurement the microcavity properties are : $\delta\nu = 44.8GHz$, $L_{cav} = 22.6\mu m$ and $V_{peak} = 0.58V$. The maximum Lorentzian peak voltage is obtained by taking the maximum PD signal from the entire trace. **(Right)** The voltage trace from the left figure which is converted to a detuning in cavity length (in frequency and length). The measurement is performed by using the DL laser.

6.4. Summary

In this chapter, a method for actively stabilising the microcavity length is shown. The microcavity length is stabilised by feeding back the transmission signal to both the coarse piezo and the fine piezo. The active stabilisation method uses the coarse piezo to counteract microcavity length changes at low frequency (drifts) whereas the fine piezo is used to counteract microcavity length changes at higher frequencies (vibrations). Using this active stabilisation method, a fundamental mode is found automatically and the microcavity is automatically locked to that fundamental mode. Due to different noise sources, the actual RMS vibration level with active length stabilisation of the microcavity cannot be determined. The best estimation of the performance of the lock is that the RMS vibration level stays below $10pm$ and the lock is reducing the vibration level by at least a factor 2. This is still only the vibration level when the cryocooler is off. Further improvements to the system should allow to also lock the microcavity length when the cryocooler is on.

7

Conclusion & Outlook

7.1. Conclusion

The goal of this thesis is to characterise the new microcavity setup and stabilise the microcavity length in order to move towards Purcell enhancement of colour centres in diamond. To achieve a stable microcavity length, three goals are set in the introduction (Chapter 1), where the conclusion of these goals is described in this section.

First, control of the new setup is obtained. Where the microcavity length and microcavity linewidth can be measured with high accuracy. Using the new obtained control over the microcavity more properties are investigated. By analysing the microcavity length dependence on temperature, a dependence of $3\frac{1}{3}\mu m$ per $^{\circ}\mathrm{C}$ is found. Furthermore, the Radius Of Curvature (ROC) can be automatically determined and the found ROC is in good agreement with the analysis performed after the fibre has been manufactured. Using the ROC, further analysis allows us to measure the angle of the fibre with respect to the plane mirror. This will be a useful tool later on when the most ideal microcavity must be formed for Purcell enhancement. By measuring the finesse of the microcavity for different lengths, a maximum finesse of 6000 is obtained. This results in a quality factor of around 80.000 and a mode volume of $27\lambda_0^3$ for $L_{cav} = 5\mu m$.

Second, the vibrations influencing the microcavity length are studied in detail. Several important frequency ranges of the vibrations detuning the microcavity length are found and are located between $1-3Hz$, $10-20Hz$, $250-300Hz$ and $750-900Hz$. Both the $10-20Hz$ and $750-900Hz$ vibrations can be heavily suppressed by changing the conditions of the passive vibration isolator which supports the microcavity. However, the vibrations with $1-3Hz$ and $250-300Hz$ remain present with the current performance of the passive vibration isolation in the setup. The origin of these vibrations is investigated and there are indications that vibrations are related to the passive vibration isolator. However, this cannot be said with certainty and more measurements need to be performed to find the exact origin of these vibrations. The performance of the passive vibration isolation is not optimal, resulting in a high level of vibration. The size of the microcavity length detuning (due to vibrations) exceeds the maximum level of vibrations which allows for active feedback in a high finesse microcavity ($20-30pm$). When the cryocooler is turned on, the vibrations even exceed the threshold of reliable vibration measurements. By improving the passive vibration isolation, this problem can be solved. Active feedback is still a possibility but can only be performed for a low finesse microcavity with the cryocooler off.

Finally, the transmission signal of the microcavity is used to actively feedback a voltage to two piezo's in the setup. One piezo (coarse piezo) counteracts microcavity length drifts (low frequency) and a high bandwidth piezo (fine piezo) counteracts a detuning in microcavity length due to vibrations (high frequency). With this active feedback method, a fundamental mode of the microcavity can automatically be found, and the microcavity length can be locked to that mode. Different noise sources prevent us from determining the actual RMS vibration level when the microcavity length is actively stabilised. An estimation of the maximum RMS vibration level with the cryocooler off, at room temperature and with active stabilisation is $10pm$. This is at least a factor 2 lower than the RMS vibration level without active stabilisation. The vibration level obtained in this thesis compared to other literature can be found in Table 7.1

Table 7.1: Overview of the state of the art vibration levels of open Fabry-Pérot microcavities. For a closed-cycle cryostat, the cryostat is the most dominant source of vibrations. This has to be taken into account when comparing the RMS vibration levels. If the solid state emitter is stated in italics, the literature did not place the actual emitter in the microcavity. Most literature uses the Pound-Drever-Hall (PDH) lock or a Photothermal (PT) lock to actively stabilise the microcavity. This table shows there are quite some improvements to be made, in order to compete with other quantum nodes and microcavities.

Cryostat	Temperature	Solid state emitter	Active stabilisation	RMS vibrations (pm)	Source
Closed-cycle	Room temperature	*Colour centres, in diamond*	Yes, (below 10 kHz), Transmission signal	< 10	This thesis
Closed-cycle	$< 7K$	With erbium ions, in yttria	Yes, PDH (below 1kHz), Reflection signal	62.5	B. Casabone, 2021 [49]
Closed-cycle	$4K$	*NV centre, in diamond*	Yes, PDH (Below 1kHz), Reflection signal	54	Y. Fontana, 2021 [20]
Closed-cycle	$4K$	With NV centre, in diamond	NO	125	M. Ruf, 2021 [19]
Closed-cycle	$2K$	Erbium ions, in yttrium orthosilicate	Yes, PT, Reflection signal	4.3	B. Merkel, 2020 [50]
Liquid-Helium bath	$4K$	NV centre, in diamond	NO	< 5	D. Riedel,2017 [15] L. Greuter,2014 [35]
N/A	Room temperature	N/A	Yes, PDH and PT (Below 500kHz), Reflection signal	0.11	J. Brachmann, 2016 [51]

7.2. Outlook

As can be seen in Table 7.1, the room temperature vibration level of this thesis is still very high compared to other setups. To reduce the RMS vibration level in the new cavity setup, multiple improvements need to be made:

1. The performance of the passive vibration isolator from Janssen Precision Engineering (JPE) needs to be improved. The vibration isolator is not functioning according to design due to the amount of mass on top of the passive vibration isolator. The amount of mass on top of the vibration isolator has already been minimized, so in order to increase the performance, multiple steps can be taken. Some components of the vibration isolator can be replaced with titanium or can be slightly changed in design. If the performance of the new vibration isolator does not improve, a different plan needs to be constructed (using the passive vibration setup from [19] in the HILA cryostat, new vibration isolator etc.).

2. An electrical input filter needs to be installed. During this thesis, a microcavity length detuning at $50Hz$ is constantly present. This is due to an electronic signal constantly driving either one of the positioners/piezo's in the setup. Removing this constant drive by filtering the electronic input signals should decrease the vibration level. Moreover, by using the filter the positioners/piezo's do not have to be grounded, which will significantly improve the ease of operation of the setup.

3. If the performance of the passive vibration isolation increases, the vibration level needs to be assessed once more. Followed by active length stabilisation (using the technique shown in this thesis) when the cryocooler is on. If the vibration level is sufficiently low, all of the measurements performed in this thesis need to be performed at cryogenic temperature. Moreover, a diamond platelet has to be bonded to the flat mirror to characterise and stabilise a diamond-air microcavity.

4. If the vibration level is not sufficiently low, a different type of active length stabilisation can be applied. The Pound-Drever-Hall lock is a promising locking technique and is discussed more in Appendix F. Multiple simulations show that the PDH lock should be possible in the new cavity setup. However, limited time has prevented us from implementing the PDH lock in the new setup during this thesis.

After the microcavity has a sufficiently low RMS vibration level at cryogenic temperature with a diamond platelet, the focus of the microcavity project will shift more to the colour centre in diamond. With a stable microcavity, the microcavity must be tuned on resonance with the ZPL of a colour centre in diamond to generate Purcell enhancement.

Bibliography

[1] JI Cirac, AK Ekert, SF Huelga, and Chiara Macchiavello. Distributed quantum computation over noisy channels. *Physical Review A*, 59(6):4249, 1999.

[2] Nicolas Gisin and Rob Thew. Quantum communication. *Nature photonics*, 1(3):165–171, 2007.

[3] Hannes Bernien, Bas Hensen, Wolfgang Pfaff, Gerwin Koolstra, Machiel S Blok, Lucio Robledo, TH Taminiau, Matthew Markham, Daniel J Twitchen, Lilian Childress, et al. Heralded entanglement between solid-state qubits separated by three metres. *Nature*, 497(7447):86–90, 2013.

[4] Bas Hensen, Hannes Bernien, Anaïs E Dréau, Andreas Reiserer, Norbert Kalb, Machiel S Blok, Just Ruitenberg, Raymond FL Vermeulen, Raymond N Schouten, Carlos Abellán, et al. Loophole-free bell inequality violation using electron spins separated by 1.3 kilometres. *Nature*, 526(7575): 682–686, 2015.

[5] Norbert Kalb. *Diamond-based quantum networks with multi-qubit nodes*. PhD thesis, Delft University of Technology, 2018.

[6] Romana Schirhagl, Kevin Chang, Michael Loretz, and Christian L Degen. Nitrogen-vacancy centers in diamond: nanoscale sensors for physics and biology. *Annual review of physical chemistry*, 65:83–105, 2014.

[7] Lucio Robledo, Hannes Bernien, Ilse Van Weperen, and Ronald Hanson. Control and coherence of the optical transition of single nitrogen vacancy centers in diamond. *Physical review letters*, 105 (17):177403, 2010.

[8] Forrest T Charnock and TA Kennedy. Combined optical and microwave approach for performing quantum spin operations on the nitrogen-vacancy center in diamond. *Physical Review B*, 64(4): 041201, 2001.

[9] R Hanson, FM Mendoza, RJ Epstein, and DD Awschalom. Polarization and readout of coupled single spins in diamond. *Physical review letters*, 97(8):087601, 2006.

[10] CE Bradley, Joe Randall, Mohamed H Abobeih, RC Berrevoets, MJ Degen, MA Bakker, Matthew Markham, DJ Twitchen, and Tim H Taminiau. A ten-qubit solid-state spin register with quantum memory up to one minute. *Physical Review X*, 9(3):031045, 2019.

[11] Norbert Kalb, Peter C Humphreys, JJ Slim, and Ronald Hanson. Dephasing mechanisms of diamond-based nuclear-spin memories for quantum networks. *Physical Review A*, 97(6):062330, 2018.

[12] Peter Christian Maurer, Georg Kucsko, Christian Latta, Liang Jiang, Norman Ying Yao, Steven D Bennett, Fernando Pastawski, David Hunger, Nicholas Chisholm, Matthew Markham, et al. Room-temperature quantum bit memory exceeding one second. *Science*, 336(6086):1283–1286, 2012.

[13] Mohamed H Abobeih, Julia Cramer, Michiel A Bakker, Norbert Kalb, Matthew Markham, Daniel J Twitchen, and Tim H Taminiau. One-second coherence for a single electron spin coupled to a multi-qubit nuclear-spin environment. *Nature communications*, 9(1):1–8, 2018.

[14] Matteo Pompili, Sophie L. N. Hermans, Simon Baier, Hans K. C. Beukers, Peter C. Humphreys, Raymond N. Schouten, Raymond F. L. Vermeulen, Marijn J. Tiggelman, Laura dos Santos Martins, Bas Dirkse, Stephanie Wehner, and Ronald Hanson. Realization of a multi-node quantum network of remote solid-state qubits, 2021.

[15] Daniel Riedel, Immo Söllner, Brendan J Shields, Sebastian Starosielec, Patrick Appel, Elke Neu, Patrick Maletinsky, and Richard J Warburton. Deterministic enhancement of coherent photon generation from a nitrogen-vacancy center in ultrapure diamond. *Physical Review X*, 7(3):031040, 2017.

[16] Peter C Humphreys, Norbert Kalb, Jaco PJ Morits, Raymond N Schouten, Raymond FL Vermeulen, Daniel J Twitchen, Matthew Markham, and Ronald Hanson. Deterministic delivery of remote entanglement on a quantum network. *Nature*, 558(7709):268–273, 2018.

[17] Mark Fox. *Quantum optics: an introduction*, volume 15. OUP Oxford, 2006.

[18] Edward Mills Purcell. Spontaneous emission probabilities at radio frequencies. In *Confined Electrons and Photons*, pages 839–839. Springer, 1995.

[19] Maximilian Ruf, Matthew J Weaver, Suzanne B van Dam, and Ronald Hanson. Resonant excitation and purcell enhancement of coherent nitrogen-vacancy centers coupled to a fabry-perot microcavity. *Physical Review Applied*, 15(2):024049, 2021.

[20] Yannik Fontana, Rigel Zifkin, Erika Janitz, Cesar Daniel Rodríguez Rosenblueth, and Lilian Childress. A mechanically stable and tunable cryogenic fabry–pérot microcavity. *Review of Scientific Instruments*, 92(5):053906, 2021.

[21] John Walker. Optical absorption and luminescence in diamond. *Reports on progress in physics*, 42(10):1605, 1979.

[22] NB Manson, JP Harrison, and MJ Sellars. Nitrogen-vacancy center in diamond: Model of the electronic structure and associated dynamics. *Physical Review B*, 74(10):104303, 2006.

[23] SB van Dam. *Optical cavities, coherent emitters, and protocols for diamond-based quantum networks*. PhD thesis, Delft University of Technology, the Netherlands, 2019.

[24] Toeno Van der Sar. *Quantum control of single spins and single photons in diamond*. PhD thesis, Delft University of Technology, the Netherlands, 2012.

[25] Bas Hensen. *Quantum nonlocality with spins in diamond*. PhD thesis, Delft University of Technology, the Netherlands, 2016.

[26] Hannes Bernien. *Control, measurement and entanglement of remote quantum spin registers in diamond*. PhD thesis, Delft University of Technology, 2014.

[27] KD Jahnke, B Naydenov, T Teraji, S Koizumi, T Umeda, J Isoya, and Fedor Jelezko. Long coherence time of spin qubits in 12c enriched polycrystalline chemical vapor deposition diamond. *Applied physics letters*, 101(1):012405, 2012.

[28] Sophocles J Orfanidis. *Electromagnetic waves and antennas*. Rutgers University,Piscataway, NJ, 2016.

[29] Herwig Kogelnik and Tingye Li. Laser beams and resonators. *Applied optics*, 5(10):1550–1567, 1966.

[30] CJR Sheppard. Approximate calculation of the reflection coefficient from a stratified medium. *Pure and Applied Optics: Journal of the European Optical Society Part A*, 4(5):665, 1995.

[31] Garrett D Cole, Wei Zhang, Bryce J Bjork, David Follman, Paula Heu, Christoph Deutsch, Lindsay Sonderhouse, John Robinson, Chris Franz, Alexei Alexandrovski, et al. High-performance near- and mid-infrared crystalline coatings. *Optica*, 3(6):647–656, 2016.

[32] Andrew Zangwill. *Modern electrodynamics*. Cambridge University Press, 2013.

[33] Sophie Hermans. Towards Purcell enhancement of the zero-phononline of nitrogen-vacancy centres in diamond in an open Fabry-Pérot microcavity. Master's thesis, Delft University of Technology, the Netherlands, 2017.

[34] Yuli V Nazarov and Jeroen Danon. *Advanced Quantum Mechanics: A Practical Guide*. Cambridge University Press, 2013.

[35] Lukas Greuter, Sebastian Starosielec, Daniel Najer, Arne Ludwig, Luc Duempelmann, Dominik Rohner, and Richard J Warburton. A small mode volume tunable microcavity: Development and characterization. *Applied Physics Letters*, 105(12):121105, 2014.

[36] Erika Janitz, Maximilian Ruf, Yannik Fontana, Jack Sankey, and Lilian Childress. High mechanical bandwidth fiber-coupled fabry-perot cavity. *Optics express*, 25(17):20932–20943, 2017.

[37] Maximilian Ruf. Fiber-based fabry-perot microcavities. Master's thesis, McGill University, Canada, 2017.

[38] Material Properties Data. Alumina (Aluminum Oxide). https://www.makeitfrom.com/material-properties/Alumina-Aluminum-Oxide-Al2O3, 30-05-2020. [Online; Accessed: 22-07-2021].

[39] Santiago Sager La Ganga. Finesse and birefringence in a Fabry Perot cavity with a diamond membrane. Master's thesis, Delft University of Technology, the Netherlands, 2020.

[40] Daniel Riedel, Sigurd Flågan, Patrick Maletinsky, and Richard J Warburton. Cavity-enhanced raman scattering for in situ alignment and characterization of solid-state microcavities. *Physical Review Applied*, 13(1):014036, 2020.

[41] Theresa A Maldonado. Electro-optic modulators. *Handbook of optics*, 2:13–11, 1995.

[42] Wikipedia contributors. Utility frequency — Wikipedia, the free encyclopedia, 2021. URL https://en.wikipedia.org/w/index.php?title=Utility_frequency&oldid=1026985016. [Online; accessed 29-September-2021].

[43] Guillermo J Costa. Tuning a pid controller. *power transmission engineering*, 5(2):26–31, 2011.

[44] Zurich Instruments. Principles of Lock-in Detection, 2021. URL https://www.zhinst.com/europe/en/resources/principles-of-lock-in-detection. [Online; accessed 29-September-2021].

[45] Robert V Pound. Electronic frequency stabilization of microwave oscillators. *Review of Scientific Instruments*, 17(11):490–505, 1946.

[46] RWP Drever, John L Hall, FV Kowalski, J_ Hough, GM Ford, AJ Munley, and H Ward. Laser phase and frequency stabilization using an optical resonator. *Applied Physics B*, 31(2):97–105, 1983.

[47] G. Zames. Feedback and optimal sensitivity: Model reference transformations, multiplicative seminorms, and approximate inverses. *IEEE Transactions on Automatic Control*, 26(2):301–320, 1981. doi: 10.1109/TAC.1981.1102603.

[48] Lucio Robledo, Lilian Childress, Hannes Bernien, Bas Hensen, Paul FA Alkemade, and Ronald Hanson. High-fidelity projective read-out of a solid-state spin quantum register. *Nature*, 477(7366):574–578, 2011.

[49] Bernardo Casabone, Chetan Deshmukh, Shuping Liu, Diana Serrano, Alban Ferrier, Thomas Hümmer, Philippe Goldner, David Hunger, and Hugues de Riedmatten. Dynamic control of purcell enhanced emission of erbium ions in nanoparticles. *Nature communications*, 12(1):1–7, 2021.

[50] Benjamin Merkel, Alexander Ulanowski, and Andreas Reiserer. Coherent and purcell-enhanced emission from erbium dopants in a cryogenic high-q resonator. *Physical Review X*, 10(4):041025, 2020.

[51] Johannes FS Brachmann, Hanno Kaupp, Theodor W Hänsch, and David Hunger. Photothermal effects in ultra-precisely stabilized tunable microcavities. *Optics express*, 24(18):21205–21215, 2016.

[52] Wikipedia contributors. Accelerometer — Wikipedia, the free encyclopedia. https://en.wikipedia.org/w/index.php?title=Accelerometer&oldid=1045549851, 2021. [Online; accessed 5-October-2021].

[53] Eric D Black. An introduction to pound–drever–hall laser frequency stabilization. *American journal of physics*, 69(1):79–87, 2001.

A

Fibre Analysis

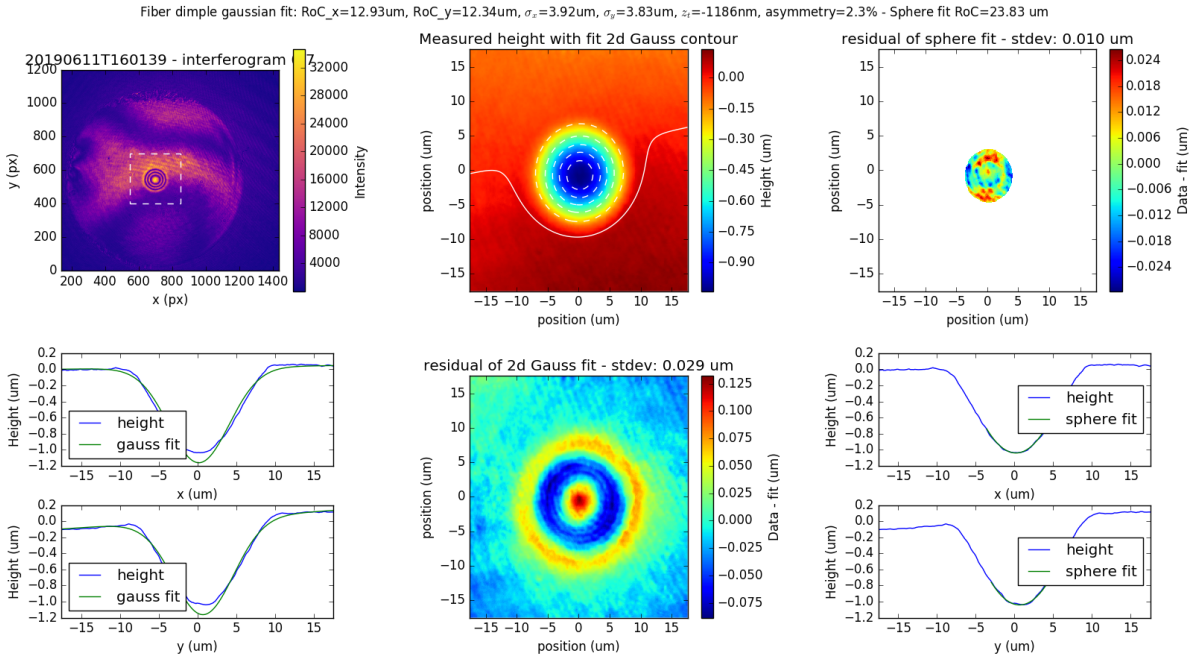

Figure A.1: Fibre analysis after the fibre tip is fabricated by TNO.

B

Transfer function measurement

The transfer function measurement is used to find the resonances of the entire setup. By exciting the different available piezo's or the entire setup itself, the resonance frequencies of the setup can be found. In this appendix, a short explanation of how the measurement is performed will be given in Section B.1. Followed by Section B.2, which discusses the results of the transfer function measurements.

B.1. Measurement Method

To find the resonance frequencies of the setup (or the piezo itself) a Lock-In Amplifier is used (HF2LI 50 MHz Lock-in Amplifier Zurich Instruments). A schematic overview of the used setup is shown in Figure B.1. The output of the Lock-in amplifier can be connected to different piezo's in the setup to excite them with an AC signal. The Photodiode (PD) in the detection path (Figure 3.5) is used to detect the transmitted light from the cavity. The PD is connected to the Lock-In amplifier and mixed with the applied AC signal. The output AC signal can internally be connected to the input of the Lock-In amplifier. A phase shifter (AC delay) is placed between the applied AC signal and the mixer to ensure a maximum error signal. After the PD signal and the applied AC signal are mixed, a low pass filter is used to suppress higher-order frequency components of the mixed signal. For this measurement, the green laser is used because, at this point in time, the HILA cryostat is not installed and the drifts in L_{cav} are too high to use a red laser. The different piezo's which can be driven by the AC signal are the: Fine piezo, the coarse piezo and a piezo shaker. A piezo shaker is a piezo which is mounted below the baseplate and pushed against the bottom of the base plate (see Figure E.2). The idea of the piezo shaker is that it can excite the entire setup and thus find the resonance frequencies of the entire setup. The piezo shaker only works when the piezo shaker is able to excite the baseplate enough. The reason why a resonance of the setup can be detected is explained in the following paragraph.

By applying an AC signal to either of the specified piezo's in the setup a small detuning in L_{cav} is induced. Since a green laser is used the finesse of the microcavity is very low with a high linewidth. Inducing a detuning in microcavity length is thus essentially a vibration measurement, but with induced vibrations. Due to the induced vibrations, a change in the PD signal (even for the green laser) can be detected. Logically, this change in PD signal should have the same frequency as the applied AC signal. Using the two signals, the Lock-In amplifier denotes the amplitude and phase relative to the applied AC signal. The Lock-In amplifier uses a dual demodulation circuit to obtain the amplitude and phase signal after the low pass filter [44]. If there is a correlation between the applied AC signal and the PD signal the amplitude and phase should stay constant. If a resonance frequency of the system is found, the phase and amplitude will change significantly since the PD signal will differ more from the applied AC signal. By investigating both the phase and amplitude of the final signal the resonance frequencies can be identified. In the measurement, the frequency of the AC signal is scanned over a certain frequency range and the phase and amplitude are recorded for each applied frequency.

B.2. Results

In Figure B.2, the recorded amplitude and phase of the transfer function measurement is shown for the applied frequencies to the coarse piezo. The first and most noticeable frequency which has a

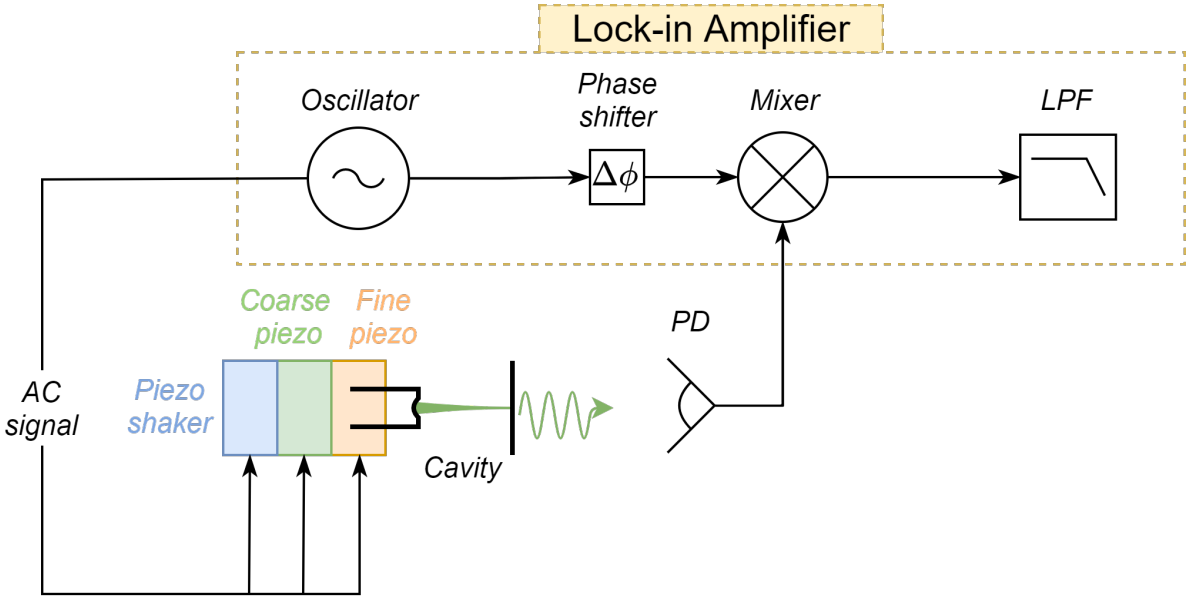

Figure B.1: Circuit for the transfer function measurement. The AC signal can be either applied to the fine piezo to which the fibre is glued (orange), the coarse piezo in the JPE positioner stack (blue) or the piezo shaker (green). The circuit is simplified as the actual circuit uses a dual demodulation circuit [44]. For this experiment, the green laser is used and the amplitude of the AC signal is kept constant during the entire measurement

resonance are multiples of $50Hz$. This is a clear indication that there is an electronic contribution for this resonance frequency, as has been extensively discussed in Section 5.2.1. Another resonance seems to be located around $250 - 270Hz$. However, it is hard to distinguish this resonance from the $50Hz$ contribution to microcavity length detuning. As there is no filter yet which filters out the low frequency electrical signals the measurement cannot be performed without introducing the $50Hz$ noise. The last and most important resonance which can be seen in Figure B.2, is the frequency range $650Hz - 2kHz$. In this range, multiple resonance frequencies of the JPE positioner system are situated. This gives an upper bound to the frequencies which can be applied to the coarse piezo.

The transfer function measurement is also performed by applying an AC signal to the fine piezo. This piezo has less travel range and is assumed not to excite the resonances of the setup (JPE positioner stack). However, the measurement for the fine piezo gives information about the maximum bandwidth for active feedback. As active stabilisation of L_{cav} will be performed with the fine piezo, it is important to find the resonance frequencies of the fine piezo (and every other resonance frequencies the fine piezo excites). In Figure B.3, the results of the transfer function measurement are shown. Other measurements with the fine piezo indicated no special resonances below $100Hz$, so only the range $100Hz - 55kHz$ is shown. Again in this measurement, a clear presence of the $50Hz$ detuning is visible. However, from this measurement it can be concluded that the bandwidth of the fine piezo is quite high and can be used in the range $100Hz - 20kHz$. This bandwidth is more than enough and allows us to (ideally) actively feedback vibrations up to $\sim 20kHz$.

Another measurement is performed by applying an AC signal to the piezo shaker. Ideally, the piezo shaker transfers energy to the mock-up baseplate of the HILA cryostat, thus the performance of the JPE passive vibration isolator can be tested. However, the range of the piezo shaker is problematic in order to fully trust the measurement. The piezo shaker must transfer its energy (due to the applied AC signal) to the heavy HILA baseplate. This energy transfer is not straight forward and it appears that the piezo shaker does not have the range to excite the HILA baseplate enough. Multiple measurements are taken (in different frequency ranges) and are combined in Figure B.4. Looking at the results of the piezo shaker measurements, no clear resonances are visible (except the multiples of $50Hz$). This could either mean that the vibration isolator of JPE is working perfectly. Or that the piezo shaker is not exciting the base plate enough. The latter conclusion seems most likely but cannot be said with absolute certainty. To find the exact resonances of the entire system it would be beneficial to perform the measurement again but with a different piezo shaker. Furthermore, these transfer function

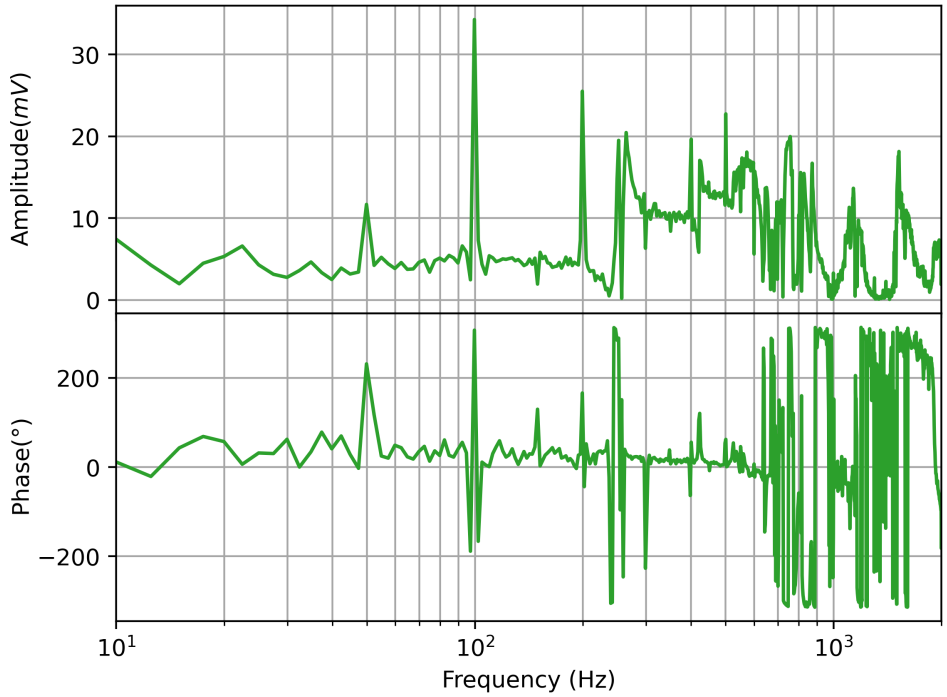

Figure B.2: Amplitude and phase of the out put signal after demodulation in the Lock-in amplifier. For this measurement the AC signal is applied to the coarse piezo and has the following properties: $f = 10Hz - 2kHz$, $V_{offset} = 300mV$ and $V_{pp} = 30mV$.

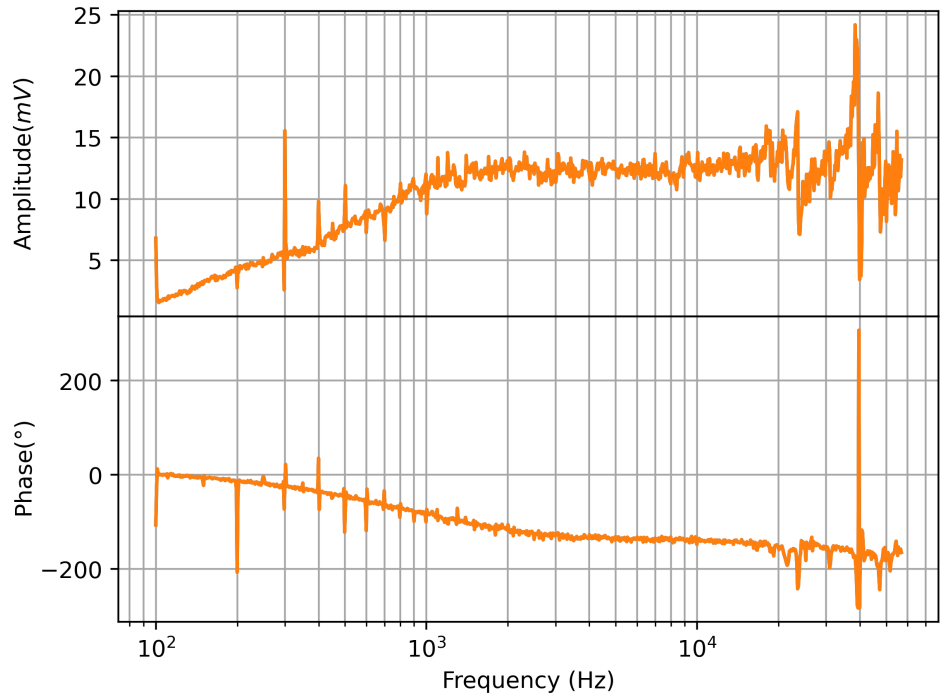

Figure B.3: Amplitude and phase of the out put signal after demodulation in the Lock-in amplifier. For this measurement the AC signal is applied to the fine piezo and has the following properties: $f = 100Hz - 55kHz$, $V_{offset} = 2V$ and $V_{pp} = 2V$.

measurements are all performed before the HILA cryostat is installed. This could influence all the measurements shown in this appendix, and thus measuring the transfer function again with the HILA installed is highly recommended. Furthermore, the transfer function measurement can now also be performed with a red laser instead of a green laser. This makes the measurement more sensitive.

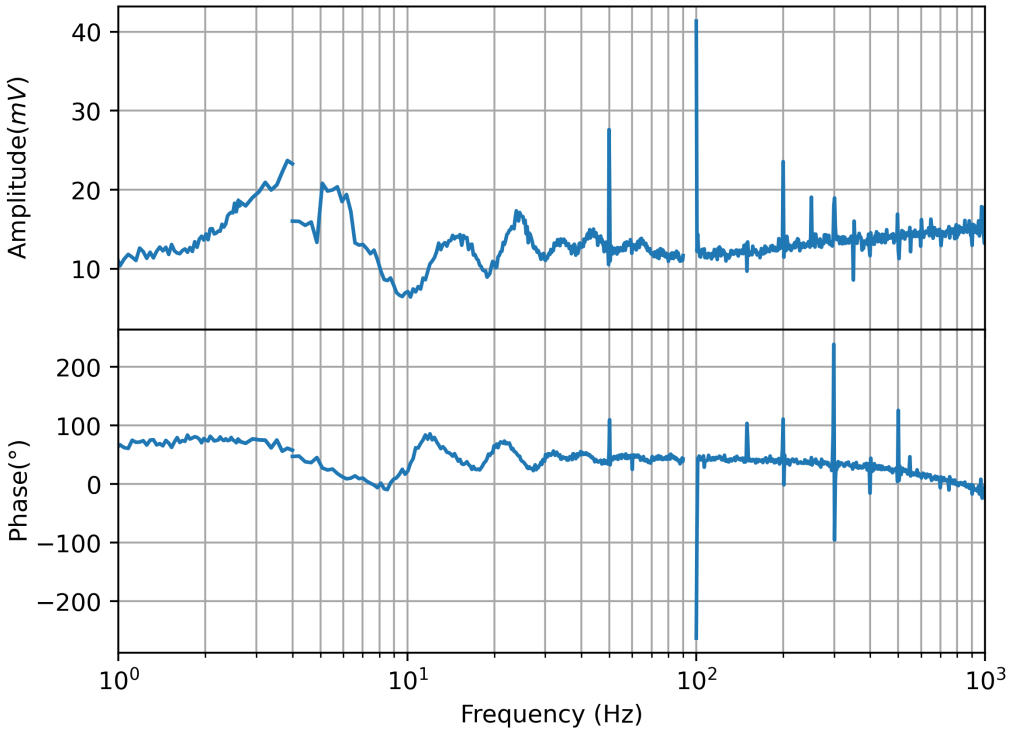

Figure B.4: Amplitude and phase of the out put signal after demodulation in the Lock-in amplifier. For this measurement the AC signal is applied to the piezo shaker and has the following properties: $f = 1Hz - 1kHz$, $V_{offset} = 0V$ and $V_{pp} = 560mV$. Where the gaps between certain frequency arises due to separate measurements with different starting and final frequencies.

C

Accelerometer Measurement

The accelerometer measurements are used to find the frequencies of the vibrations which are transmitted to the microcavity. The accelerometer is borrowed from JPE for a short timespan, meaning that the measurements could only be performed with the (at that time) limited knowledge about the problems of the floating condition of the JPE stage. An important note which needs to be made, is that the accelerometer measurements have not been performed by myself, thus limited details are given. Nonetheless, in this appendix a short explanation of how the measurement is performed will be given in Section C.1. Followed by Section C.2, which discusses the results of the transfer function measurements.

C.1. Measurement Method

Accelerations, and thus vibrations, can be measured with an accelerometer [52]. The most interesting places where the accelerations can be measured are:

- On the HILA baseplate. By measuring the vibrations at this location the vibrations which are not suppressed by the floating HILA baseplate can be identified.
- On the mirror sample holder. By measuring the vibrations which are transmitted up to the mirror holder, the performance of the JPE passive vibration isolator can be identified. When measuring the accelerations on the mirror holder, the JPE passive vibration isolator can be put in a non-floating condition, and an almost floating condition (as mentioned multiple times throughout this thesis).

The conditions in which the accelerations are measured can best be described as follows. First of all, in the accelerometer measurements the mirror holder is still made out of copper and thus heavier than the aluminium mirror holder used for the vibration measurements. This will make the floating condition generally worse than in the vibration measurements. Furthermore, the accelerometer also has some wires connecting it to the PCB and some weight. This can also slightly change the resonance conditions of the complex system. Second, the wire connecting the nanopositioner in the z-direction to the PCB is till touching the HILA baseplate at this moment in time. Finally, the leaf springs in the bars (Figure E.1) are assumed to also be bend. By measuring the accelerations over a certain amount of time and applying an FFT on the time signal, the frequencies (and size) of the accelerations are detected. The main conclusion from the results, together with the measurement conditions can be found in section C.2

C.2. Results

The accelerations which are measured at the HILA baseplate are shown in Figure C.1. In this measurement, the accelerations are measured without vacuum (base level, both roughing pump and turbopump are switched off), at vacuum ($10^{-6}mbar$) (roughing pump and turbopump are on) and at vacuum ($10^{-6}mbar$) with the cryocooler on. The unit on the y-axis is in standard units of acceleration. These

plots are thus not used to measure the exact level of vibrations but mainly the frequencies of the vibrations (accelerations). What can be seen is that there is a high level of acceleration at multiples of $30-40Hz$. Which are most likely to come from the roughing pump, as the turbopump is spinning at $1500Hz$. When switching on the cryocooler, the general level of accelerations increases and finding specific frequencies which are transmitted to the HILA baseplate is quite hard. Then again, the actual accelerations which are relevant are the accelerations at the microcavity, and thus at the mirror holder.

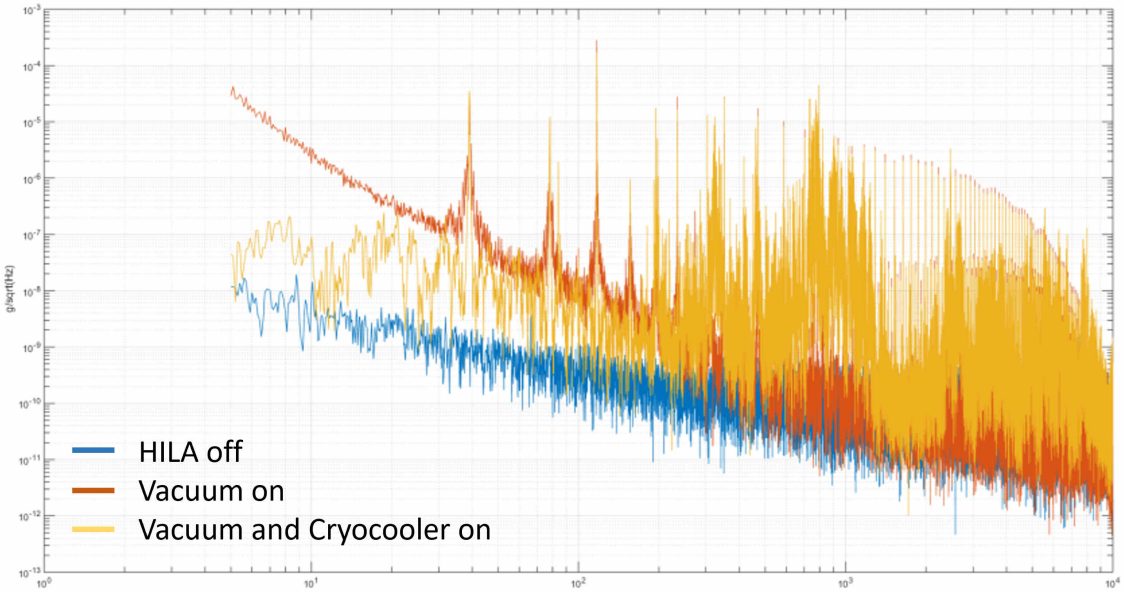

Figure C.1: Acceleration measurement performed at the HILA baseplate. Here the y axis is in units of $g/\sqrt{Hz}$. The blue line indicates the baseline, both the vacuum pumps are turned off and the cryocooler is off. The orange line shows the accelerations when the roughing pump and the turbopump are pumping. The yellow line shows the accelerations when the roughing pump and turbo pump are both on and the cryocooler is on.

The FFT of the acceleration signal and the cumulative sum of the FFT measured at the mirror holder are shown in Figure C.2. Where the explanation for the legend is:

- **Montana HILA Delft**: The acceleration measurement at the HILA baseplate with the vacuum pumps on and the cryocooler on.
- **Montana HILA w/vib iso**: The acceleration measurement at the mirror holder of the microcavity when the JPE passive vibration isolator is NOT floating. For this measurement, the vacuum pumps and cryocooler are also on.
- **Montana HILA w/vib iso floating**: The acceleration measurement at the mirror holder of the microcavity when the JPE passive vibration isolator is floating. For this measurement, the vacuum pumps and cryocooler are also on.
- **Montana HILA OFF**: the acceleration measurement at the HILA baseplate with the vacuum pumps on and the cryocooler OFF.

It is quite hard to find any relevant information from the FFT figure. Looking at the cumulative sum gives more information. Especially the difference between the floating condition and the non-floating condition is of interest. The cumulative sum of the floating condition (red) is multiplied by 500 to show the suppression of accelerations compared to measuring the accelerations at the HILA baseplate (turquoise/blue). However, when the JPE stage is in the floating condition (as far as that is possible) the acceleration level increases significantly. Multiplying the acceleration data from the floating condition (cyan) with 20, gives approximately the same acceleration level as the non-floating condition (brown/orange). Indicating once again, that the JPE vibration isolator is not in the ideal position. What can be noticed is some frequencies of accelerations that are also seen in the vibration measurements. The $250Hz$ and the $700-900Hz$ vibrations are also measured in the acceleration measurement. Something

which is far from ideal, but should not be a problem if the JPE passive vibration isolator is functioning properly, is the huge level of accelerations at the HILA baseplate at $700 - 900Hz$. These accelerations are exactly on resonance with the JPE positioner stage and might thus become problematic if the JPE passive vibration isolator is not functioning properly. However, in the same figure it can be seen that the vibrations from the HILA baseplate are quite well suppressed with the JPE passive vibration isolator.

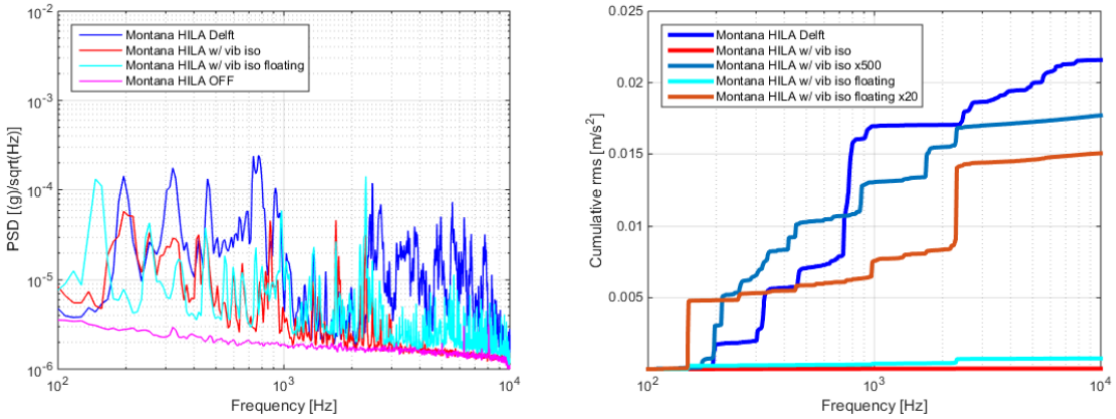

Figure C.2: **(Left)** Power Spectral Density function of the acceleration data measured at different locations and conditions (see text). **(Right)** Cumulative sum of the PSD of the left figure. Here the data of the non floating condition (red) is multiplied by 500 to show the relative improvement the JPE stage has on the acceleration level (turquoise/blue). The data of the floating condition (cyan) is multiplied by 20 to show the same acceleration level more detailed (brown/orange).

D

Additional Measurement Figures

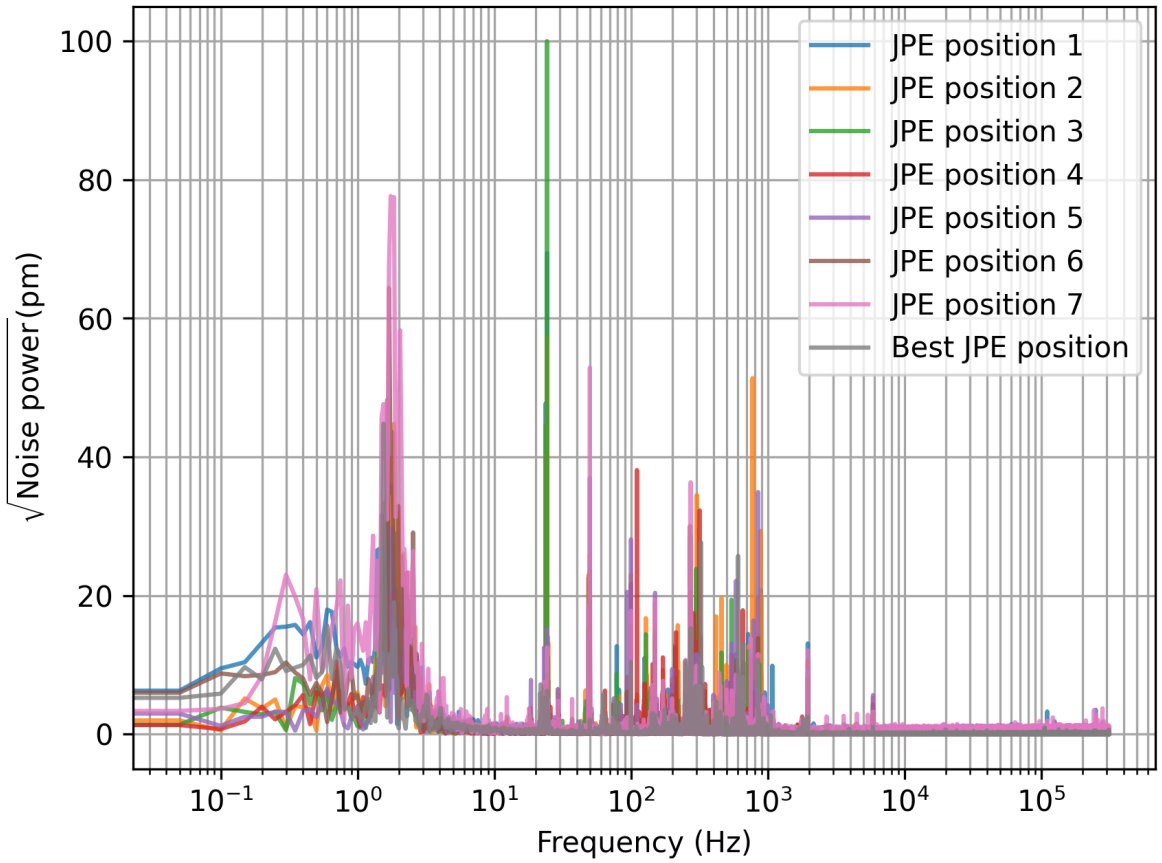

Figure D.1: The FFT of the length detuning signal discussed in subsection 5.2.2. The cumulative sum of this FFT is shown in Figure 5.5. Position 1 indicates the reference point of the other positions. For positions 1 and 2, it is known that the JPE passive vibration isolator is in the NOT floating condition. From position 3 to position 5 the vibration isolator is moving towards the floating condition. For positions 6 and 7, the JPE module motors are reaching their end stop. The measurements of positions 1-7 are all performed with the same vacuum conditions. Furthermore, the wire connecting the PCB to the coarse piezo is touching the baseplate in all of these measurements. For the best JPE position, the wire is not touching and the best floating condition is found by looking at each JPE passive vibration isolator module.

E

Setup Pictures

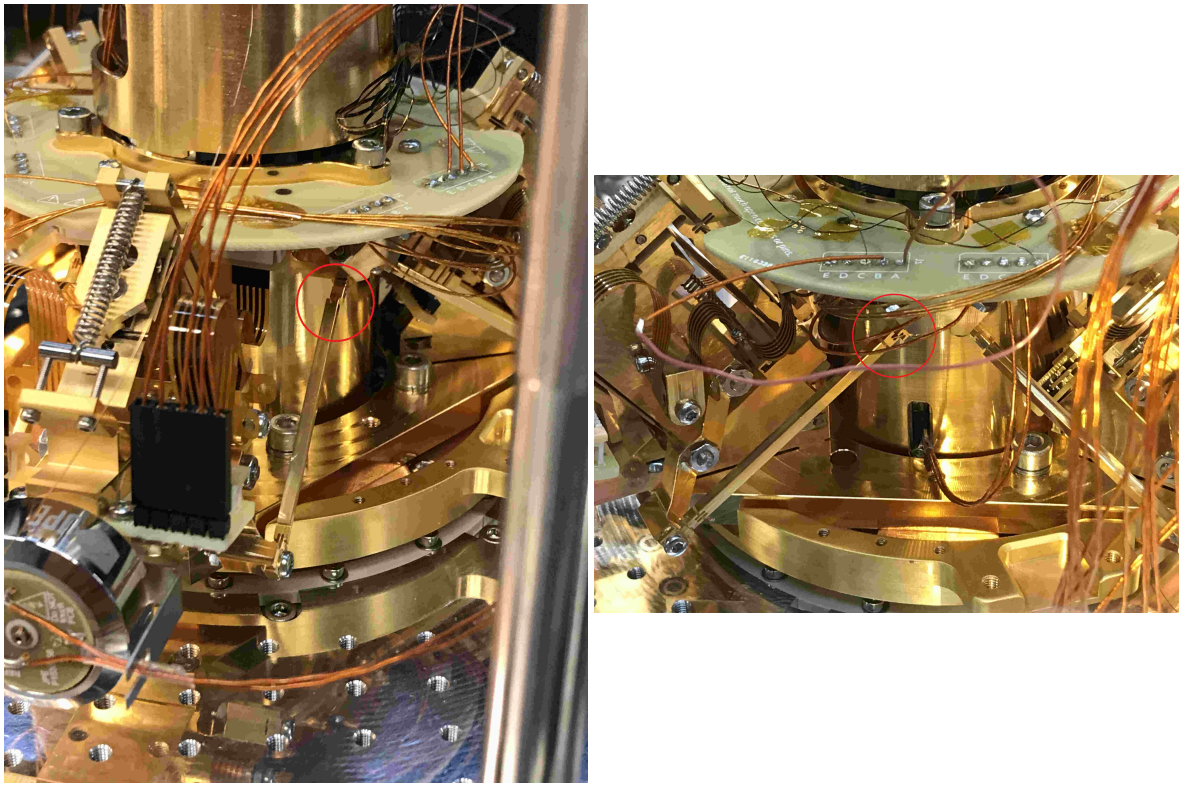

Figure E.1: **(Left)** JPE passive vibration isolator bars. Where the leaf springs at the end of the bars (close to the JPE positioner stack) are clearly bend, indicated with the red circle. The bend leaf springs may prevent the the entire stack to float and does not have a positive influence on the passive vibration isolation. **(Right)** Another picture showing the bend leaf springs, but from a different bar and different perspective.

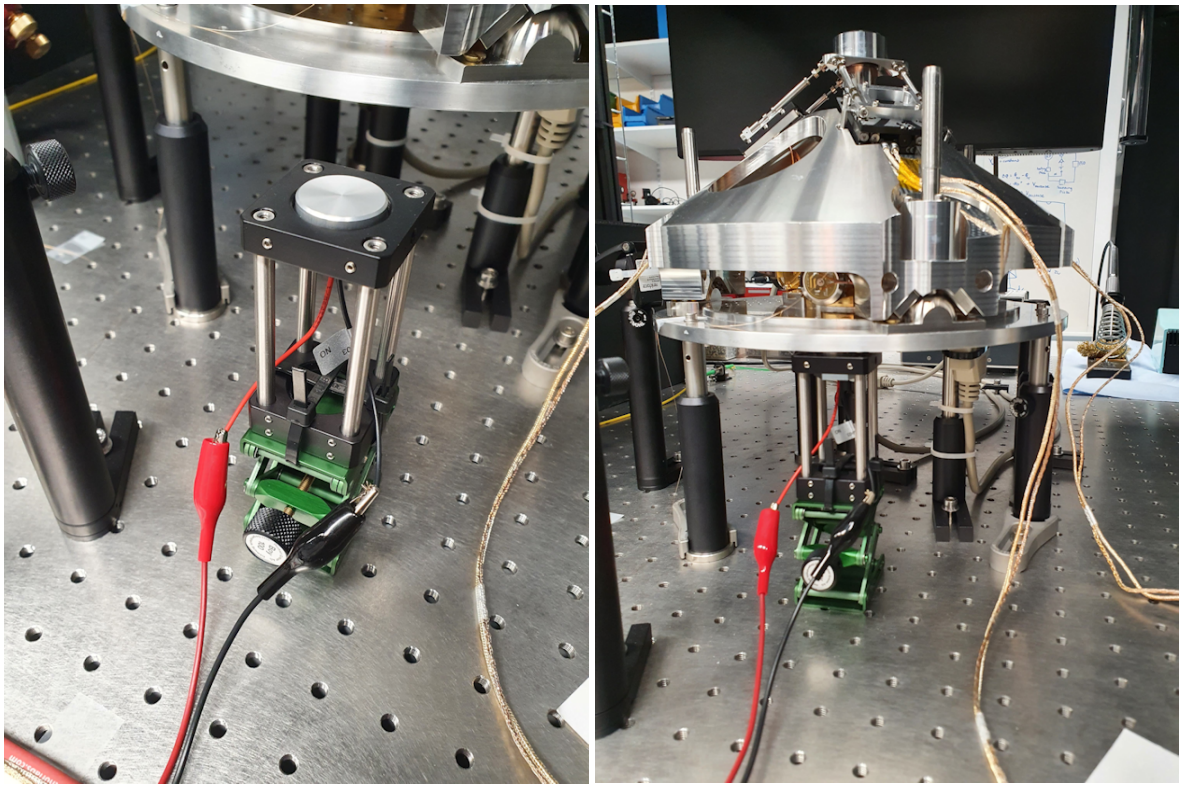

Figure E.2: **(Left)** The piezo shaker which is mounted on a lifting jack and connected to the Lock-In amplifier. **(Right)** Another picture of the piezo shaker. The piezo shaker is pressed against the bottom of the mock-up HILA baseplate. The mock-up baseplate has the same dimensions as the floating baseplate in the HILA cryostat and is used in the first part of this thesis. On top of the mock-up baseplate the vibration isolator is located together with the objective cone.

F

Pound-Drever-Hall Lock Simulations

The Pound-Drever-Hall (PDH) lock is a powerful stabilising technique for lasers and cavities in general. The frequency of a laser can be stabilised by using a static cavity. And the length of an optical cavity can be stabilised if the laser frequency is stable. For this thesis, the stabilisation of the cavity length is the obvious objective. The schematic feedback circuit of a PDH lock can be found in Figure F.1. For this thesis both the reflected and transmitted light of the microcavity can be used. During this thesis the transmitted light is used, to attempt to generate an error signal. The error signal is the most interesting part of the PDH lock, as the error signal is used to feedback a voltage to the fine piezo. Therefore, the error signal is the only part of the PDH lock which is discussed in detail in this Appendix. Due to the low responsivity of the PD used in this setup, a real error signal has not been measured during this thesis. Hence, only the theory behind the error signal and simulations of the error signal using parameters of the setup are discussed. Starting with a general mathematical description of the error signal in Section F.1. Followed by two different regimes for the error signal. A regime where the modulation frequency is smaller than the linewidth (Section F.2), and a regime where the modulation frequency is larger than the linewidth (Section F.3). The same method in simulation the error signal is used as described in [53]. The figures from this paper are used to validate the model.

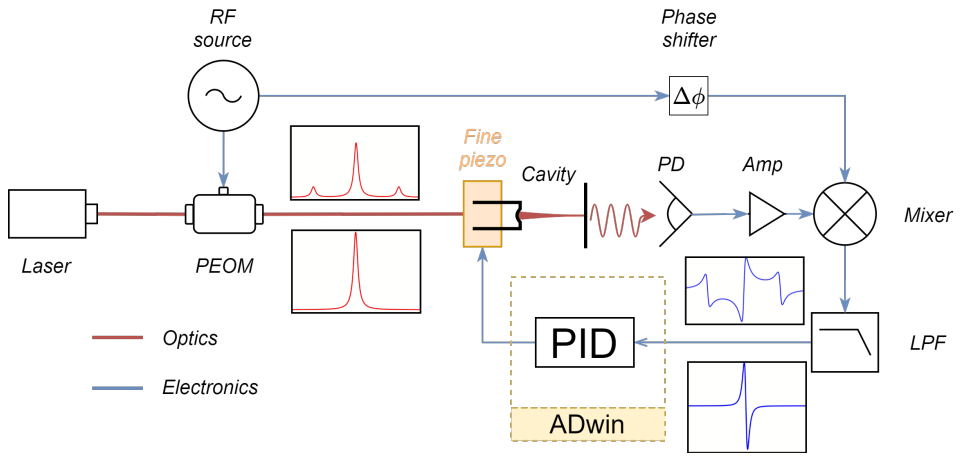

Figure F.1: Schematic overview of the PDH lock. In the PDH lock, the laser frequency is modulated, giving rise to two sidebands in the incoming electric field of the cavity. The incoming power of the beam (over frequency) for a modulated and not modulated laser is shown in the insets of the overview. The PhotoDiode (PD) signal is enhanced with an amplifier (amp) to create a larger error signal. After mixing the modulation signal and the enhanced PD signal and then applying a low pass filter on the mixed signal, an error signal will be generated. The insets show the error signal for a modulated and non modulated laser frequency. The error signal can then be converted to a feedback voltage using a PID loop.

F.1. Error Signal of the PDH Lock

The lock in this thesis modulates the microcavity length to stabilise the microcavity length. As has been explained already, this is not desirable when performing measurements as the microcavity length should stay constant and on resonance with the ZPL transition of the NV^-. To keep the microcavity length stable and still feedback an error signal to actively stabilise the length, another (measurable) quantity needs to be modulated. With the PDH lock, the laser frequency is modulated with a Phase Electro-Optic Modulator (PEOM). The reason a PEOM is used is best explained by looking at the transmission/reflection signal from the PD. Using the transfer matrix method of an open microcavity (derived in Section 2.2.1) the reflection coefficient is given by:

$$F_{Refl} = \frac{E_{refl}}{E_{inc}} = \frac{r_2 e^{i\frac{\omega}{2\Delta\nu_{FSR}}} - r_1 e^{-i\frac{\omega}{2\Delta\nu_{FSR}}}}{e^{i\frac{\omega}{2\Delta\nu_{FSR}}} - r_1 r_2 e^{-i\frac{\omega}{2\Delta\nu_{FSR}}}}. \tag{F.1}$$

Furthermore the transmission coefficient is given by:

$$F_{Trans} = \frac{E_{trans}}{E_{inc}} = \frac{t_1 t_2}{e^{i\frac{\omega}{2\Delta\nu_{FSR}}} - r_1 r_2 e^{-i\frac{\omega}{2\Delta\nu_{FSR}}}}. \tag{F.2}$$

This is the case for a non modulated laser with angular frequency ω and the FSR frequency $\Delta\nu_{FSR}$. The cavity has two mirrors with reflection coefficient r_1, r_2 and transmission coefficients t_1, t_2. If the laser frequency is modulated, two sidebands arise next to the main transmission Lorentzian transmission peak. This will result in the following incoming electric field at the first cavity mirror:

$$E_{inc} \approx E_0 \left(J_0(\beta)e^{i\omega t} + J_1(\beta)e^{i(\omega+\Omega)t} - J_1(\beta)e^{i(\omega-\Omega)t}\right). \tag{F.3}$$

Here E_0 is the amplitude of the incoming electric field, $J_i(\beta)$ indicates the Bessel function and Ω is the modulation frequency. Using these Bessel functions it is very easy to see that there are 3 peaks going into the cavity. The main transmission peak, with frequency ω (carrier) and two sideband peaks with frequency $\omega \pm \Omega$. Where the power going into the sideband peaks can be adjusted with β. In equation F.3 the assumption is made that the power going into the sidebands is rather low ($\beta < 0$). The power in carrier and sideband peaks is then given by:

$$P_c = J_0^2(\beta)P_0, \tag{F.4}$$

$$P_c = J_1^2(\beta)P_0, \tag{F.5}$$

respectively. With $P_0 = |E_0|^2$ the total power of the incident beam. To compute the actual reflected/-transmitted electric field from the cavity which needs to be used to actively feedback the microcavity length, each incident peak (carrier and sidebands) can be addressed individually. Resulting in:

$$E_i = E_0 \left(F_i(\omega)J_0(\beta)e^{i\omega t} + F_i(\omega+\Omega)J_1(\beta)e^{i(\omega+\Omega)t} - F_i(\omega-\Omega)J_1(\beta)e^{i(\omega-\Omega)t}\right), \tag{F.6}$$

where i can either be reflection or transmission. Since the electric field is not the direct measurable quantity, the reflected/transmitted electric field is converted to power. The resulting power of the beam is (after quite some algebra) given by:

$$\begin{aligned} P_i = {} & P_c\left|F_i(\omega)\right|^2 + P_s\left[\left|F_i(\omega+\Omega)\right|^2 + \left|F_i(\omega+\Omega)\right|^2\right] \\ & + 2\sqrt{P_c P_s}\,\mathrm{Re}\left(F_i(\omega)F_i^*(\omega+\Omega) - F_i^*(\omega)F_i(\omega-\Omega)\right)\cos(\Omega t) \\ & + 2\sqrt{P_c P_s}\,\mathrm{Im}\left(F_i(\omega)F_i^*(\omega+\Omega) - F_i^*(\omega)F_i(\omega-\Omega)\right)\sin(\Omega t) \\ & + h.o.t(2\Omega) \end{aligned} \tag{F.7}$$

Equation F.7 shows the expected PD signal. Where the first line indicates three different waves with frequency ω and $\omega \pm \Omega$. The second and third line indicate the interaction/interference between the sidebands and the carrier wave. Finally, the fourth line indicates the interference between the sidebands, which are neglected. This is not yet the error signal on which active feedback can be given. To

obtain the actual error signal the PD signal needs to be mixed with the applied Ω frequency signal and low passed filtered.

By mixing the PD signal with the applied modulation frequency, the two signals are essentially multiplied. Using the basic $\sin / \cos$ rules:

$$\sin(\Omega_1 t)\sin(\Omega_2 t) = \frac{1}{2}\{\cos([\Omega_1 - \Omega_2]\, t) - \cos([\Omega_1 - \Omega_2]\, t)\} \tag{F.8}$$

the $\Omega_1 - \Omega_2$ term can be separated by low-pass filtering the mixed signal. Since Ω_1 and Ω_2 should be equal with a microcavity, the resulting error signal will simply be a DC signal. This error signal contains the information of the phase of the reflected/transmitted light of the cavity and can be used to tune the microcavity exactly on resonance. A small side note to equation F.8 is the phase difference between the modulation signal and the PD signal. For equation F.8 the mixed signals are both sine waves, the relative phase compared to each other is equal. If the phase difference between the mixed signals is exactly $90°$ the following $\sin / \cos$ rules need to be used:

$$\sin(\Omega_1 t)\cos(\Omega_2 t) = \frac{1}{2}\{\sin([\Omega_1 - \Omega_2]\, t) - \sin([\Omega_1 - \Omega_2]\, t)\} \tag{F.9}$$

If $\Omega_1 = \Omega_2$ the DC term vanishes and no error signal will remain after the low pass filter. This is the reason why a phase-shifter (signal delay) needs to be placed in the electronic circuit of Figure F.1. The phase-shifter can then be used to obtain the correct phase difference between the modulation signal and the PD signal.

There are two regions of operation when using the PDH lock:

1. **Low modulation:** When the modulation frequency is low compared to the linewidth of the cavity ($\Omega < \delta\nu$), the field in the cavity has time to respond.

2. **High modulation:** When the modulation frequency is high compared to the linewidth of the cavity ($\Omega > \delta\nu$), the sidebands will almost be completely reflected when on resonance with the carrier.

Both of these regimes are simulated using equation F.7. Where the real and imaginary parts of the $\left(F_i(\omega)F_i^*(\omega+\Omega) - F_i^*(\omega)F_i(\omega-\Omega)\right)$ terms are calculated and are normalized with the $2\sqrt{P_c P_s}$ factor. To compute an estimate of the error signal, multiple parameters in the setup are also included, namely:

1. Amplifier after the photodiode

2. Responsivity of the fast PD in the setup

3. Length and Finesse values from Figure 4.8

4. Reflection coefficients r_1 and r_2 (together with unknown losses to obtain the correct finesse)

The simulated error signals for both regimes are shown in the following sections.

F.2. Low Modulation Frequency Regime

For the low modulation frequency regime the following cavity parameters are used: $L_{cav} = 3.2\mu m$, $\mathcal{F} = 5462$ resulting in a linewidth of $\delta\nu = 8.6GHz$. Which is very comparable with the data from Figure 4.8. Multiple fractions of $\frac{\Omega}{\delta\nu}$ are simulated to look at the corresponding error signal. In the left figure of Figure F.2, the PD signal of both reflection and transmission signal is shown. The right figure of Figure F.2 shows the computed error signal which can be measured after the low pass filter for different modulation frequencies. The simulated modulation frequencies range from $1 - 6GHz$

Due to the low responsivity of the PD, these signals have not been measured. Therefore, these simulations only serve as an indication of what the error signal will look like.

F.3. High Modulation Frequency Regime

For the high modulation frequency regime the following cavity parameters are used: $L_{cav} = 13.7\mu m$, $\mathcal{F} = 4331$ resulting in a linewidth of $\delta\nu = 2.5GHz$. Again, in very goof comparison with the data from Figure 4.8. Multiple fractions of $\frac{\Omega}{\delta\nu}$ are simulated to look at the corresponding error signal. In

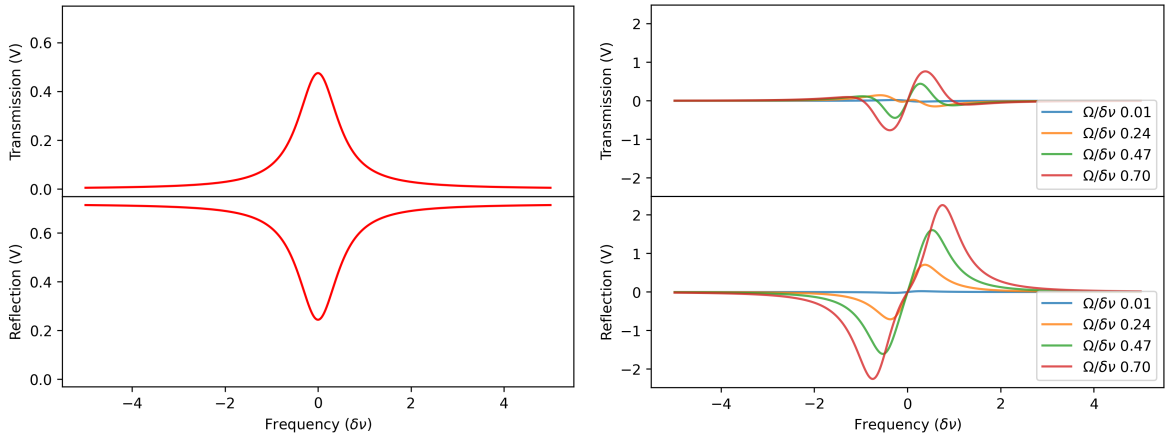

Figure F.2: **(Left)** PD transmission voltage and reflection voltage of the microcavity when the modulation frequency is small ($\Omega = 3GHz$). The following cavity parameters are simulated $L_{cav} = 3.2\mu m, \mathcal{F} = 5462$ resulting in a linewidth of $\delta\nu = 8.6GHz$. **(right)** Simulated error signal for the transmission and reflection signal. For low modulation frequency the reflection error signal will be purely real. Whereas the transmission signal will have both an imaginary and real contribution (see equation F.7).

the left figure of Figure F.3, the PD signal of both reflection and transmission signal is shown. The right figure of Figure F.3 shows the computed error signal which can be measured after the low pass filter for different modulation frequencies. The simulated modulation frequencies range from $3 - 9GHz$ Again, due to the low responsivity of the PD these signal have not been measured. Both Figure F.3

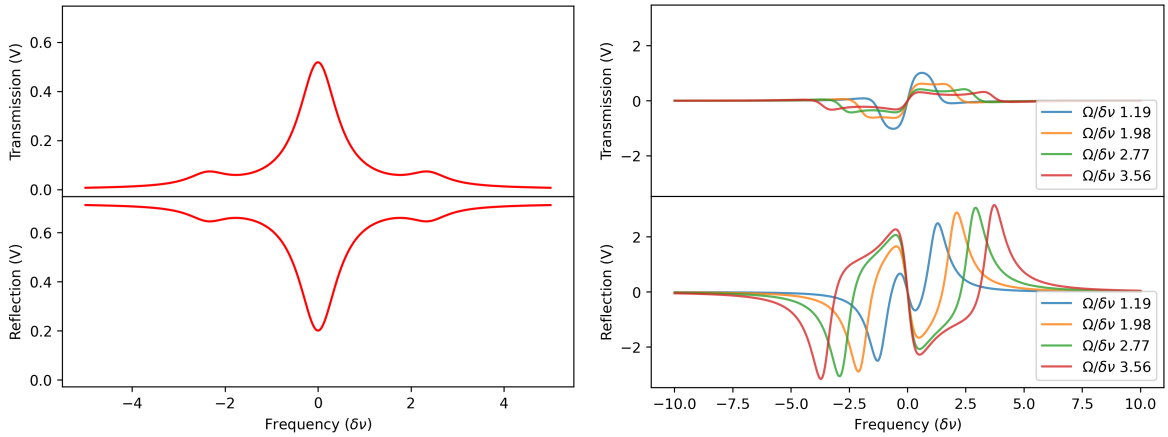

Figure F.3: **(Left)** PD transmission voltage and reflection voltage of the microcavity when the modulation frequency is high ($\Omega = 6GHz$). The following cavity parameters are simulated $L_{cav} = 13.7\mu m, \mathcal{F} = 4331$ resulting in a linewidth of $\delta\nu = 2.5GHz$. **(right)** Simulated error signal for the transmission and reflection signal. For high modulation frequency the reflection error signal will be purely imaginary at the carrier wave. Whereas the transmission signal will have both an imaginary and real contribution at the carrier wave (see equation F.7).

and F.2 show another reason why the reflection signal is preferred over the transmission signal. Apart from the sensitivity of the transmission signal to laser power fluctuations, the reflection signal has a generally larger error signal. And due to the fact that the sidebands will not ”enter” the microcavity at high modulation frequencies the phase information will eventually vanish for the transmission error signal.